SCHOOL OF ENGINEERING
RESEARCH SHOWCASE 2018

2018 Research Showcase Posters
Table of Contents

BIOENGINEERING

SCHOOL OF ENGINEERING RESEARCH SHOWCASE 2018

MECHANICAL ENGINEERING

6 - Research in Multirobot Adaptive Navigation
Robert McDonald: Mechanical Engineering, Ph.D.
Michael Neumann: Mechanical Engineering, Ph.D.
Scot Tomer: Mechanical Engineering, Master's
Danop Rajabhandharaks: Mechanical Engineering, Ph.D.
Ryan Cooper: Computer Science and Engineering, Master's
Advisor: Dr. Christopher Kitts

7 - Ground Station Location Optimization and Remote Location Telecommunication
Leland Taylor: Mechanical Engineering, Master's
Michael Neumann: Mechanical Engineering, Ph.D.
Advisor: Dr. Christopher Kitts

8 - Material Property Analysis of Aluminum Ultrasonic Wedge Wire Bonds via Nano-Indentation
Jamie Ferris: Mechanical Engineering, Undergraduate
Matthew McKay: Mechanical Engineering, Master's
Advisor: Dr. Panthea Sepehrband

9 - Simulation of Lipid Membrane Rupture via Cellular Automation
Abhay Gupta: Mechanical Engineering, Undergraduate
Irep Gözen: (University of Oslo)
Advisor: Dr. Michael Taylor

ELECTRICAL ENGINEERING

10 - 60GHz Cavity Backed Patch Antenna Array
Kasey Chun: Electrical Engineering, Master's
Advisor: Dr. Ramesh Abhari

11 - Evaluation of Biological Tissues for Wireless Power Transfer in Microwave Hyperthermia
Nivedita Parthasarathy: Electrical Engineering, Ph.D.
Advisor: Dr. Ramesh Abhari

SCHOOL OF ENGINEERING RESEARCH SHOWCASE 2018

12 - Field Pattern Measurement of Beam-Switching Planar Antenna Array with Modified Butler Matrix in SIW at 60 GHz
Benjamin Horwath: Electrical Engineering, Ph.D.
Advisor: Dr. Ramesh Abhari

13 - Multi-Port Dual Polarized Integrated Patch Antenna for RF Detection at 5.8 GHz
Jonathan Lee: Electrical Engineering, Master's
Advisor: Dr. Ramesh Abhari

14 - Proof of Concept for Tunable Periodically-Loaded Substrate Integrated Waveguide Phase Shifters
Rouzbeh Edalati: Electrical Engineering, Master's
Rudy Lopez: Electrical Engineering, Master's
Advisor: Dr. Ramesh Abhari

15 - System Level Electromagnetic Compatibility Remedy Using Absorbing Frequency Selective Surfaces
Ali Khoshniat: Electrical Engineering, Ph.D.
Advisor: Dr. Ramesh Abhari

16 - Wireless Power Transfer in Biological Materials
Daniel Webber: Electrical Engineering, Undergraduate
Nivedita Parthasarathy: Electrical Engineering, Ph.D.
Advisor: Dr. Ramesh Abhari

17 - NanoGrid: A Path to Energy Efficiency and Renewable Energy
Taylor Mau: Computer Science and Engineering/Electrical Engineering, Undergraduate
Randolph Louie: Electrical Engineering, Undergraduate
Francis Estacio: Electrical Engineering, Master's
Nicolas Garcia: Mechanical Engineering, Undergraduate
Brian Meier: Mechanical Engineering, Undergraduate
Advisor: Dr. Maryam Khanbaghi

18 - A Low Power Energy Harvesting Circuit for IoT Applications
Sanad Kawar: Electrical Engineering, Ph.D.
Advisors: Dr. Shoba Krishnan and Dr. Khaldoon Abugharbieh

SCHOOL OF ENGINEERING RESEARCH SHOWCASE 2018

19 - A C-band Wide Locking Range Injection Locked Oscillator Based Phase Shifter
Sudipta Saha: Electrical Engineering, Ph.D.
Advisors: Dr. Shoba Krishnan and Dr. Allen A Sweet

20 - Adaptive Search Pattern for Fast Motion Estimation in Video
Pavel Arnaudov: Electrical Engineering, Ph.D.
Advisor: Dr. Tokunbo Ogunfunmi

21 - An Efficient Reconfigurable Hardware Accelerator for Convolutional Neural Networks
Anaam Ansari: Electrical Engineering, Ph.D.
Advisors: Dr. Tokunbo Ogunfunmi and Dr. Kiran Gunnam

22 - Using Machine Learning to Help in Medical Devices
Juliana Shihadeh: Computer Engineering, Undergraduate
Advisor: Dr. Tokunbo Ogunfunmi

23 - Process Optimization for Carbon Nanotubes-on-Graphene Fabrication
Andrew Michelmore: Electrical Engineering, Undergraduate
Julia Shaffer: Electrical Engineering, Undergraduate
Richard Senegor: Electrical Engineering, Master's
Dayou Luo: Electrical Engineering, Master's
Advisor: Dr. Cary Yang

24 - Bayer Feature Map Approximation through Scaling of Sensor Data
Allen Rush: Electrical Engineering, Ph.D.
Advisor: Dr. Sally Wood

25 - Deep Learning Distance Measurement for Monocular Vision
Robert Christiansen: Electrical Engineering, Ph.D.
Jerry Hsu: Computer Engineering, Master's
Advisor: Dr. Sally Wood

26 Robust Localization of a Mars Exploration Rover Under Data Association Ambiguity in Aerial and Ground Imagery
Kamak Ebadi: Electrical Engineering, Ph.D.
Advisors: Dr. Sally Wood and Dr. Curtis Padgett

SCHOOL OF ENGINEERING RESEARCH SHOWCASE 2018

COMPUTER ENGINEERING

27 - Data Security using Causal Modeling
Dr. Suchitra Abel: Computer Science and Engineering, Postdoctoral Fellow
Adel Abdalla: Computer Engineering, Master's
Licheng Xiao: Computer Engineering, Master's
Lucy Kagiri: Chemistry, Undergraduate (University of California, Merced)
Advisor: Dr. Ahmed Amer

28 - Enabling Low-Power, Reliable and Timely Communication of 802.11 Devices in Cyber-Physical Systems
Jaykumar Sheth: Computer Science and Engineering, Ph.D.
Angelina Poole: Computer Science and Engineering, Master's
Advisor: Dr. Behnam Dezfouli

29 - A Remotely Programmable Software-defined Radio Platform for Low-power IoT
Rami Akeela: Electrical Engineering, Ph.D.
Advisor: Dr. Behnam Dezfouli

30 - Neural Citation Network for Context-Aware Citation Recommendation
Travis Ebesu: Computer Science and Engineering, Ph.D.
Advisor: Dr. Yi Fang

31 - Semantic Text Hashing with Weak Supervision
Suthee Chaidaroon: Computer Engineering, Ph.D.
Advisor: Dr. Yi Fang

32 - A Comparative User Study of Interactive Multilingual Search Interfaces
Chenjun Ling: Computer Engineering, Ph.D.
Ben Steichen: Not SCU anymore (Co-Advisor)
Alexander Choulos: Not SCU
Advisor: Dr. Silvia Figueira

33 - An optimized VM Allocation Strategy to Make a Secure and Energy-Efficient Cloud Against Co-residence Attack
Ruiwen Li: Computer Engineering, Undergraduate
Songjie Cai: Computer Engineering, Undergraduate
Hanxiao He: Computer Science and Engineering, Undergraduate
Advisors: Dr. Yuhoung Liu and Dr. Xiaoju Ruan

Auxetic Metamaterials in Contact Lens Sensors for IOP Monitoring

Cecilia Hemingway, Sevda Agaoglu, Kseniya Malukhina, Ju Young Lee, I. Emre Araci*
Department of Bioengineering, Santa Clara University
*email: iaraci@scu.edu

Santa Clara University
School of Engineering

Introduction

Glaucoma is a progressive disease in which the optic nerve becomes damaged leading to loss of peripheral vision or blindness

- It is the leading cause of **irreversible blindness** worldwide, with over **6 million people** blind in both eyes from it
- The primary risk factor is an increase in **intraocular pressure (IOP)**
- The cause of an increase in IOP is **unknown**

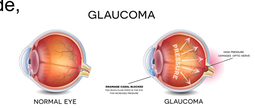

Early detection of Glaucoma preserves vision. DIfficulties with early detection include:

- Glaucoma typically has **no noticeable symptoms** until peripheral vision is already lost
- Patients go to the doctor for a one time measurement resulting in many peaks in IOP going unrecorded

Our **goal** is to develop a highly sensitive disposable, affordable contact lens that utilizes the principles of strain sensing and auxetic metamaterials for the continuous monitoring of IOP

Proof of Concept

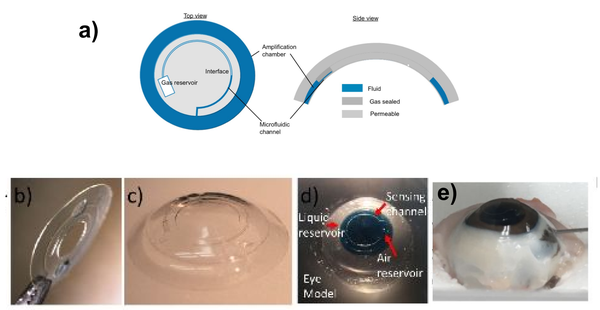

Figure 1. **a)** Top and side view of single ring strain sensor **b)** Image of completed strain sensor made of NOA 65 **c)** Embedded strain sensor within PDMS to form completed contact lens **d)** Eye model made of PDMS to mimic mechanic properties of the cornea **e)** Porcine eye used for further proof of concept that the sensor responds to applied strain

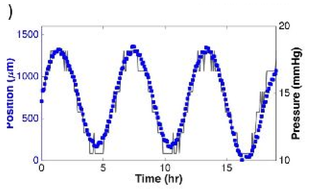

Figure 2. Position of air-liquid interface (blue square markers) in response to a sinusoidal pressure pattern (grey line) over an 18-hour period, proving that the sensor accurately responds to changes in pressure.

Auxetic Materials

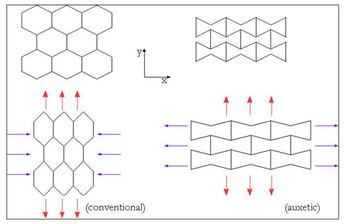

Figure 3. Auxetic Material Behavior
Auxetic materials have a negative Poisson's ratio meaning they become thicker perpendicular to applied force when stretched. This phenomenon is possible because of the geometry and internal structure of these materials.

$$\nu = -\frac{d\varepsilon_{\text{trans}}}{d\varepsilon_{\text{axial}}} = -\frac{d\varepsilon_{\text{y}}}{d\varepsilon_{\text{x}}} = -\frac{d\varepsilon_{\text{z}}}{d\varepsilon_{\text{x}}}$$

Figure 4. Poisson's Ratio Equation
Auxetic materials have a negative Poisson's ratio

Increase in Sensitivity with the use of an Auxetic Design

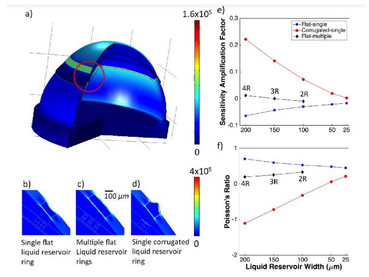

Figure 5. COMSOL testing demonstrates an increase in volume change when an auxetic top layer design is incorporated into the contact lens. This increase of volume results in an increase in sensitivity of the contact lens.

Initial Results

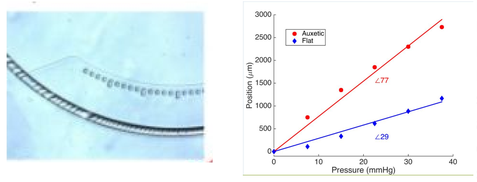

Figure 6. Image showing patterned ceiling in reservoir channel that mimics auxetic metamaterials. Graph shows experimental auxetic device response compared to flat ceiling sensor.

Fabrication Protocol

Top Layer: Auxetic Layer
NOA 65 cured for 3 minutes between a positive and negative auxetic PDMS mold

Bottom Layer
NOA 65 cured for 1 minute 30 seconds on PDMS sensing channel mold with 2 holes in the oil ring

Completed Chip
Both layers treated with plasma for 60 seconds. Bottom layer treated with APTES for 10 minutes. Chip layers bonded, filled with oil, and sealed.

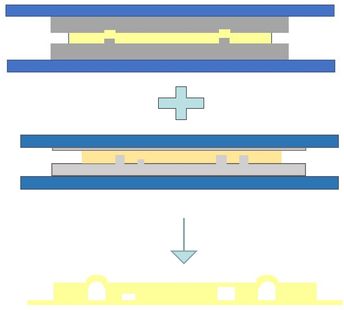

Image of Chip

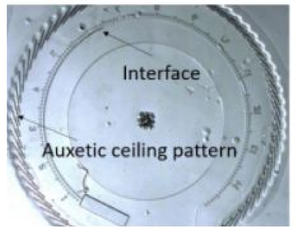

Figure 7. Image of single ring auxetic miLens fabricated using the above modified method. Height of auxetic grooves is 10 microns. Variations in auxetic design include variations in length of linear pattern and angle of the pattern.

Conclusion

In conclusion, through COMSOL simulations and initial testing of chips with patterned ceilings, it has been determined that there is an increase in the volume change of the reservoir channel. This increase in volume change correlates to an increase in sensitivity for auxetic sensors as compared to flat ones. Therefore, further testing will be done to characterize and quantify the exact increase in sensitivity. Additionally, a few variations of the auxetic chips will also be tested in order to determine which auxetic design parameters result in the greatest increase in sensitivity.

References and Acknowledgements

Agaoglu S.,, Diep P., KT S., et. al.Microfluidic metamaterials for intraocular pressure monitoring in daily wear contact lenses. Nature Biomedical Engineering. Submitted.

This study is supported by School of Engineering, SCU and partially supported by SmartLens Inc. I. Emre Araci is the co-founder of SmartLens Inc.

Dielectrophoresis as a Separation and Characterization Method for Single Droplet Encapsulated Cancer Cells

Amy Mongersun †, Emre Araci, PhD †, Prashanth Asuri, PhD, MBA †, Ramesh Abhari, PhD‡
†Department of Bioengineering, Santa Clara University, Santa Clara, California 95053, United States
‡Department of Electrical Engineering, Santa Clara University, Santa Clara, California 95053, United States

Background

Typical cell separation techniques are labeled detection methods that require prior knowledge of surface molecules or the development of probes, rendering them innately unsuited for intrinsic cell separation. The development of a microfluidic platform that could both probe for cellular characteristics and sort cells based on these characteristics quantitatively, in real-time, and without labeling would allow for an enhanced understanding of cellular heterogeneity and disease.

Objectives

1. Characterize bulk dielectric properties of biological materials and cells at microwave frequencies.
2. Simulate, optimize, and design electrodes for integration with a microfluidic device to investigate the interaction between microwaves and biological materials.
3. Fabricate an electrical microwave frequency microfluidic device capable of characterizing and sorting cells according to both intrinsic and extrinsic properties.

Material Characterization with VNA

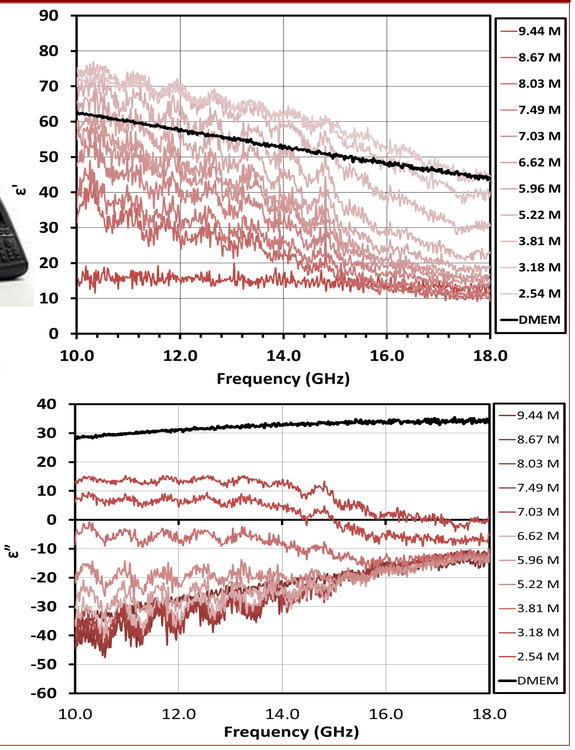

Figure 1. Dielectric characterization of real (ε') and imaginary (ε") permittivity values of varying concentrations of lactic acid obtained with a Keysight open-ended coaxial probe and Field Fox Vector Network Analyzer from 500 MHz -18 GHz. DMEM without FBS (Dulbecco's Modified Eagle Media) was also characterized to ascertain a different from output lactate concentrations.

Electrode Geometry Design

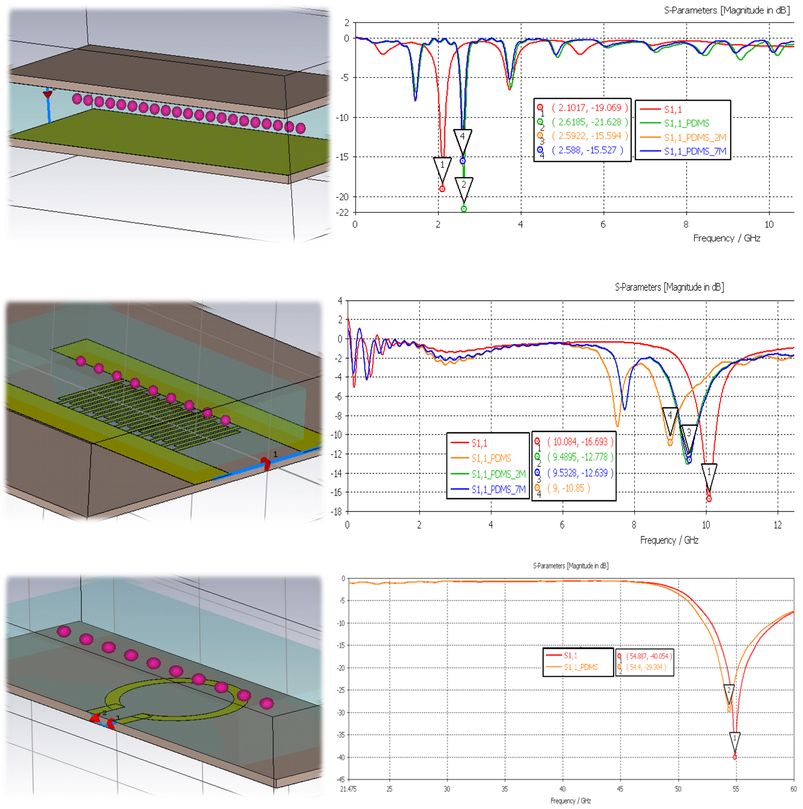

Figure 2. Three electrode geometries (left), a parallel plate capacitor, an interdigitated capacitor (IDC), and a ring resonator were investigated for suitability at biologically relevant frequency ranges. A PDMS layer with droplets of lactate was simulated to obtain S-parameters (right).

Microfluidic Layer

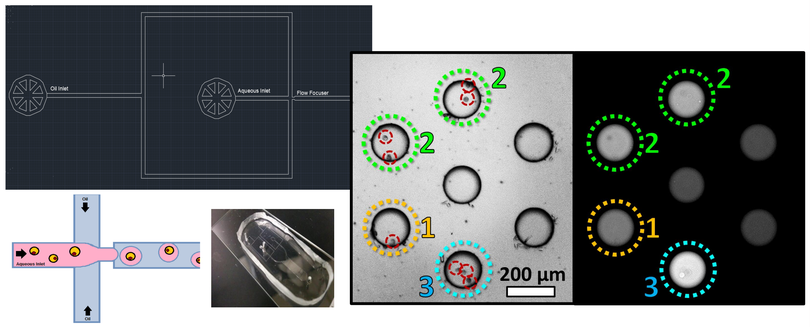

Figure 3. AutoCAD mask of flow layer to be used to create PDMS layer for creation of droplets containing cells (left). Droplets containing cells anchored within wells for an extended period of time to observe the increase in lactate concentration as a function of fluorescence increase (right).

Schematic Circuit for IDC to SMA Transition

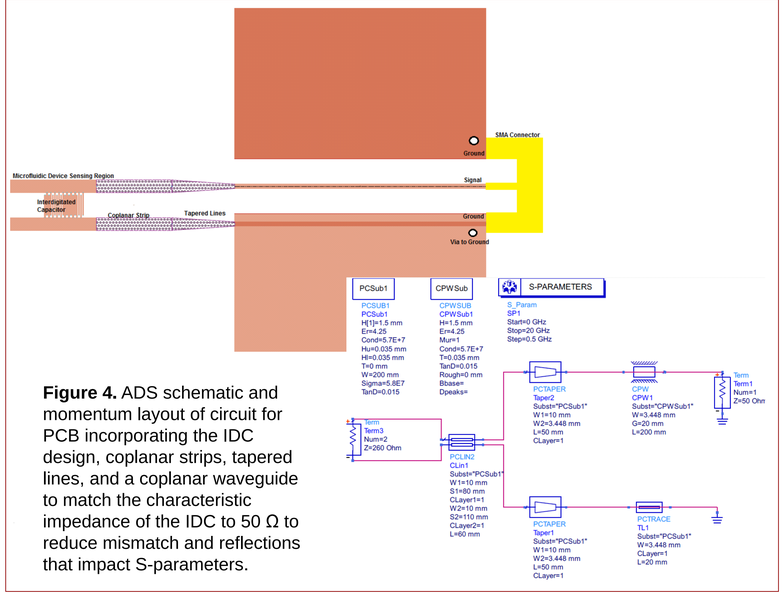

Figure 4. ADS schematic and momentum layout of circuit for PCB incorporating the IDC design, coplanar strips, tapered lines, and a coplanar waveguide to match the characteristic impedance of the IDC to 50 Ω to reduce mismatch and reflections that impact S-parameters.

Conclusions

- Varying concentrations of lactate result in dielectric permittivity values that scale with the molarity of lactate.
- Interdigitated capacitor electrode design can be utilized in the microwave frequency range to potentially sort droplets of varying concentrations of lactate.
- Microfluidic PDMS devices can be fabricated and bonded to electrical layers to measure microwave S-parameters.

Future Work

1. Optimize and tune electrode circuit design for better matching at biologically relevant frequencies.
2. Fabricate electrode device and bond with microfluidic layer.
3. Create droplets of varying concentrations of lactate and other biological materials within microwave device.
4. Create droplets encapsulating single cells to distinguish them based on secreted levels of lactate within device.
5. Create droplets encapsulating single cells and characterize and sort them according to extrinsic and intrinsic properties.

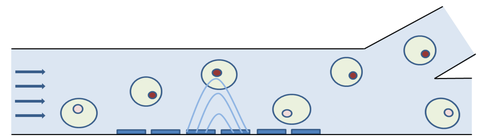

Amy Mongersun
amongersun@scu.edu

References

1. Gascoyne PRC, Shim S. Isolation of circulating tumor cells by dielectrophoresis. Cancers (Basel). 2014;6(1):545–579. PMID: 24662940
2. Dubuc D, Grenier K, Poupot M, Fournie JJ. Broadband microwave biosensing based on interdigitated capacitor for Lab-on-Chip applications. 2012 IEEE 10th Int New Circuits Syst Conf NEWCAS 2012. 2012;529–532.
3. Alazzam A, Stiharu I, Bhat R, Meguerditchian AN. Interdigitated comb-like electrodes for continuous separation of malignant cells from blood using dielectrophoresis. Electrophoresis. 2011;32(11):1327–1336. PMID: 21500214
4. Riedel M, Riedel M. Characterization of Low-Concentration Glucose / Lactate Aqueous Mixtures via MM- Waves Characterization of Low-Concentration Glucose / Lactate Aqueous Mixtures via MM-Waves. 2017;(March):0–2.
5. Yesiloz G, Boybay MS, Ren CL. Label-free high-throughput detection and content sensing of individual droplets in microfluidic systems. Lab Chip [Internet]. Royal Society of Chemistry; 2015;15(20):4008–4019.
6. Satish, Malik S, Sen K, Anand S. Measurement of dielectric properties of ringer lactate solution with respect to D-glucose. Proc 2015 IEEE Int Conf Electr Comput Commun Technol ICECCT 2015. 2015;1–4.
7. Abbyad P, Dangla R, Alexandrou A, Baroud CN. Rails and anchors: guiding and trapping droplet microreactors in two dimensions. Lab Chip. 2011;11:813–821.

SANTA CLARA UNIVERSITY

Evaluating the effect of nanoparticle-protein interactions on the biological responses of nanoparticles

Evangelia Bouzos[1], Erik Berggren[2], Lauren Schmitt[2], Sarah Anderson[2], Prashanth Asuri[1], PhD, and Korin Wheeler[2], PhD

Departments of Bioengineering[1] and Chemistry and Biochemistry[2]

Introduction

A. Motivating Questions

- How do blood proteins influence the fate and toxicity of engineered nanomaterials (ENMs) that are commonly used for medicinal purposes?
- How does ENM identity and surface coating influence the structure and function of human blood proteins?
- What role do proteins play in ENM behavior, specifically aggregation?
- What is the role of the ENM protein corona on toxicity in human cells?

B. Defining the System

- Human serum albumin (HSA) was selected as a model protein for its abundance in blood and diversity of biophysical properties. HSA is 66.5 kDa in size and has a concentration of 55% in blood.
- A library of 40 nm silver engineered nanomaterials (Ag ENMs) included a range of commonly employed surface coatings ranging from highly positive to highly negative (**Table 1**).

Table 1. Chemical structures of common engineered surface coatings.

Surface	Structure	Zeta potential at pH 7
Branched polyethylenimine (bPEI)	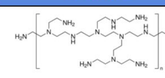	Highly positive
Citrate	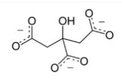	Highly negative
Polyethyleneglycol (PEG)	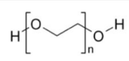	Neutral

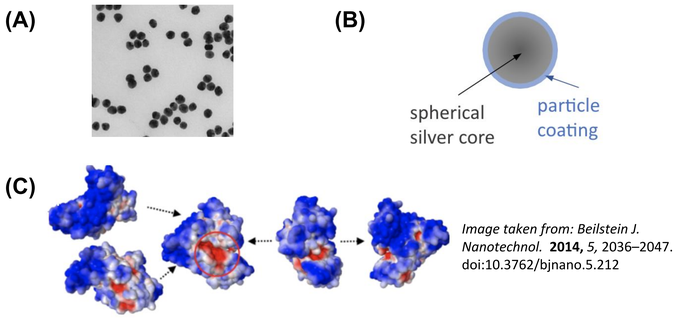

Figure 1. Model System. (A) TEM image of 40 nm Ag ENMs (image from NanoComposix, Inc) **(B)** Schematic representation of the Ag ENM structure **(C)** Surface electrostatics of HSA at pH 7.4. Potential is represented in graduating colors from dark blue (most negative) to light blue, white, light red to red (most positive). Positive region is marked by the red circle. Arrows indicate the connectivity between the faces.

Experiments and Results

A. Analysis of Protein Unfolding and Particle Aggregation:

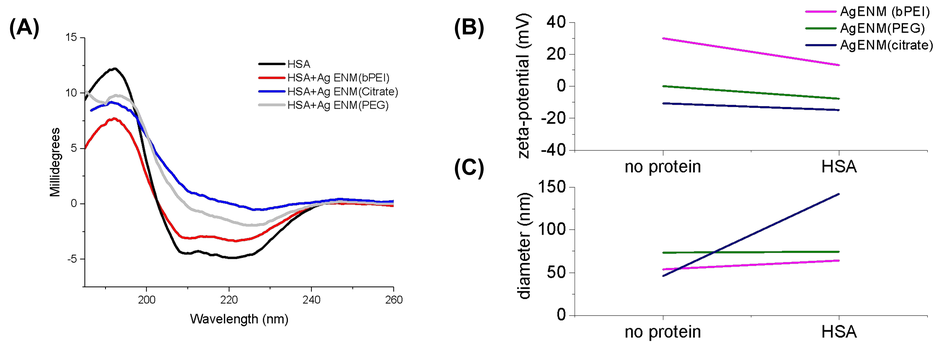

Figure 2. CD Spectroscopy, Zeta-Potential, and Hydrodynamic Diameter Measurements. (A) CD spectroscopy provides insight into the secondary structural composition of a protein. Upon addition of HSA to Ag ENMs with various coatings, protein unfolding was observed. **(B)** Zeta-potential provides surface charge changes upon addition of HSA. HSA is negatively charged at pH 7; therefore, its addition reduced the zeta-potential for all Ag ENMs in neutral pH. **(C)** The measured hydrodynamic diameter for all Ag ENMs was greater than 40 nm in solution. The addition of HSA further increased the diameter of all Ag ENMs, but the increase was most dramatic for citrate coated Ag ENMs.

B. Toxicity Testing using a Model Human Hepatic Cell Line (HepG2)

HepG2 cells were plated at a concentration of 15,000 cells/well and allowed to grow for 24 hours before ENMs (**Figure 3**) were added to the wells. WST assays were run for three days.

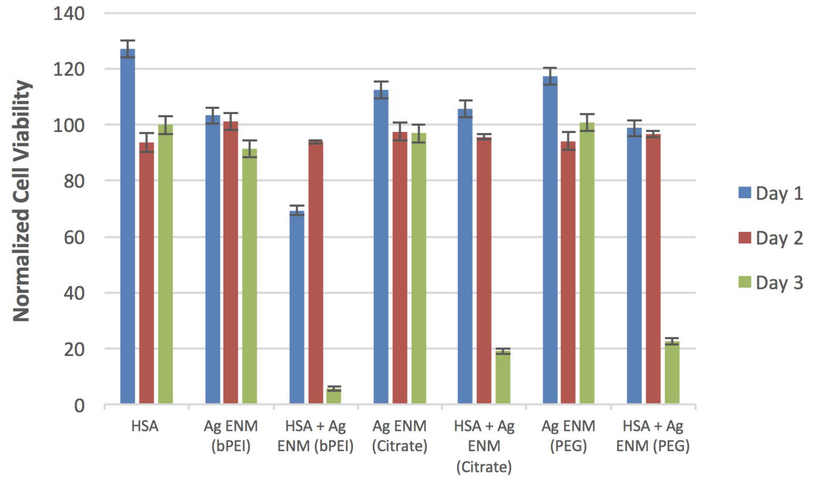

Figure 3. Trends of Ag NP Toxicity on HepG2 Cells. Raw data was normalized against no ENM controls. Averages calculated based on n=3 and N=2. Statistical significance calculated using mean±SEM.

Conclusions and Future Plans

A. Protein and particle behavior altered due to protein corona formation

- CD spectroscopy shows that HSA unfolds with the addition of each Ag ENM. Unfolding is most dramatic when HSA interacts with citrate coated and PEG coated Ag ENMs.
- Zeta-potential measurements reveal that the addition of HSA decreases the zeta-potential for each Ag ENM, but it is most dramatic for bPEI coated Ag ENM. This is likely due to stronger electrostatic interactions with HSA.
- Although all Ag ENMs were synthesized at 40 nm, hydrodynamic diameter of all Ag ENMs is slightly increased in solution, due to some aggregation in the sample buffer. Addition of HSA caused all Ag ENMs to aggregate, but aggregation is most dramatic for citrate coated Ag ENM. This is likely due to HSA unfolding.

B. Role of the ENM protein corona on the biological response of HSA coated Ag ENMs.

- Although HSA protein in solution and Ag ENMs coated with bPEI, citrate, and PEG are non toxic, HSA coated Ag ENM protein corona formation leads to decreased cell viability on day 3.

C. Short term goals/future directions

- Run Lactate Dehydrogenase (LDH) and Reactive Oxygen Species (ROS) assays to assess the subtoxic effects of HSA-ENM interactions on HepG2 cells.
- Start full examination of protein-ENM binding across a matrix of four blood proteins and five medically relevant ENM surfaces, using data gathered by DLS, and fluorescence anisotropy.
- Other methods will be used to quantify proteins at the surface of ENMs, including SDS PAGE quantification of the hard corona and TEM imaging of the protein coating.

Coat ENMs with peptides found in model proteins like HSA and fibrinogen (**Figure 4**) and evaluate the toxicity using HepG2 cells.

Long term future directions

Coat ENMs with peptides found in fibrinogen (**Figure 4**), and evaluate the toxicity using HepG2 cells.

This peptide is known to suppress relapsing paralysis in multiple sclerosis (MS):

Gamma-Fibrinogen (377-395) YSMKETTMKIIPFNRLSIG
Gamma-Fibrinogen scrambled (377-395) KMMISYTFPIERTGLISNK

Location of the peptide in the larger fibrinogen protein

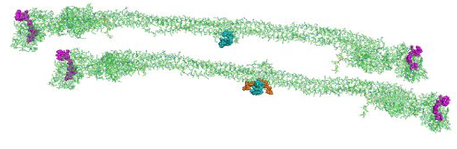

Figure 4: Diagram of Fibrinogen Protein. The Gamma-Fibrinogen (377-395) sequence is highlighted in pink.

DETECTION OF LEAD CONTAMINATION IN DRINKING WATER THROUGH ELECTROCHEMICAL SENSORS

Jo Gopinath, William Newcomb, Kyle Markfield, and Unyoung Kim

Department of Bioengineering, Santa Clara University, USA

Abstract

Lead contamination, caused by industrial run-off and pipe erosion, is a major world health problem in both developed and developing countries alike. Lead poisoning has a widespread affect on the body's tissue systems and thus often leads to neurological damage [1,2].

Thus, there is a need to detect lead contamination in water in an efficient and portable manner. Electrochemical analysis is quantitatively accurate and sensitive while also being portable, cost-effective, and easy to use for the customer.

We have developed a protocol that is not only sensitive, but has the capability of becoming much more portable for field use. While the Environmental Protection Agency has set the Maximum Contaminant Level Goal (MCLG) for lead at 0 ppb, our protocol and sensor currently have the capability to detect as low as 1 ppb [1].

Lead Contamination in Water

Lead is classified by the World Health Organization as one of the top 10 most dangerous chemicals to public health [2]. Once in the body, it is remarkably easy for lead to cross the blood-brain barrier and cause severe neurological damage, especially in children [2,3]. Thus, the EPA has set the MCLG of lead to 0 ppb [1].

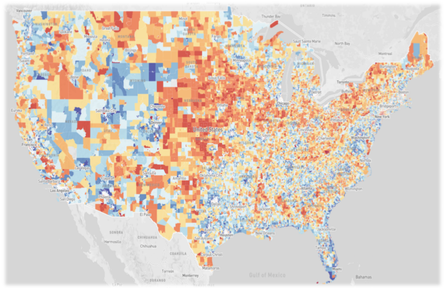

http://meridianintl.co/attachment/full/us-map-of-lead-in-water/where-is-the-lead-exposure-risk-in-your-community.jpg

Existing Technologies

Current heavy-metal detection tend to be one of these three technologies [4,5]:

Technology	Benefits	Drawbacks
Colorimetric	- Portable - Affordable - User Friendly	- Large margin of error
Mass Spectrometry	- Accurate	- Not highly portable - Expensive
Electrochemical	- Affordable - User Friendly - Portable - Accurate	

Materials and Methods

Our system setup primarily involves a Boron Doped Diamond Electrode (BDDE) connected to the CHI electrochemical analyzer.

The testing solution – which consists of varying concentrations of lead, DI water, HCl, and acidic NaCl – is deposited on the BDDE in the manner shown below.

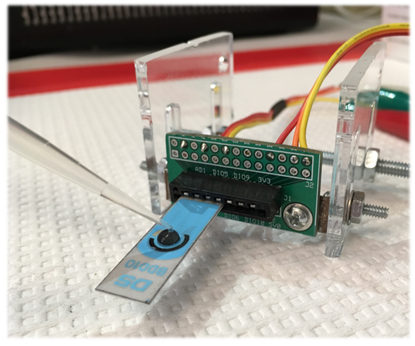

Using the CH Instrument (CHI), a differential pulse scan is run on the sample (which is explained in detail in the next section). The resulting graphs are interpreted through use of tools on the CHI software.

Electrochemical Testing Method

To detect lead, our team tested a variety of voltammetry methods. We came to the conclusion that **differential pulse voltammetry** served best for our experimental needs because of its optimum ability to detect low concentrations in relation to other commonly-used methods of heavy metal detection.

After an initial deposition period on the BDDE, the sample is run through a differential pulse voltammetry protocol. The result is a peak at a specific voltage, which hints at presence of Pb^{2+} and is dependent on the testing solution's pH and temperature.

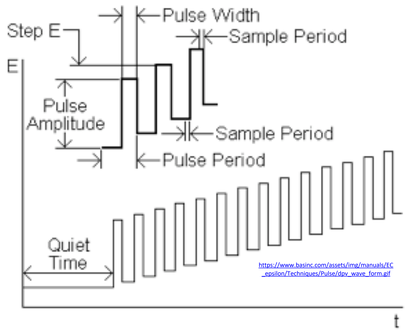

Input:
Differential Pulse Voltage

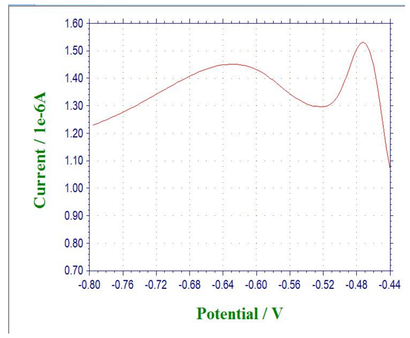

Output:
I-V Curve + Pb^{2+} voltage peak

Results

As was previously discussed, our protocol consisted of performing differential pulse voltammetry using a boron doped diamond electrode for the detection of lead. In absence of lead, no peak was observed from the working electrode (seen in red on graph). As we increased the lead concentrations from 1 to 9 ppb, we observed higher currents ranging between approximately 0.17 to 0.37 uA at the same voltage value, demonstrating that our sensor is not only detecting lead consistently, but is also able to distinguish between different concentrations of lead.

The linear regression plot seen on the right displays our data, showing that there is a clear correlation between $[Pb^{2+}]$ and current.
Our R squared value of 0.862 shows that there is clear room for improvement in our testing protocol.

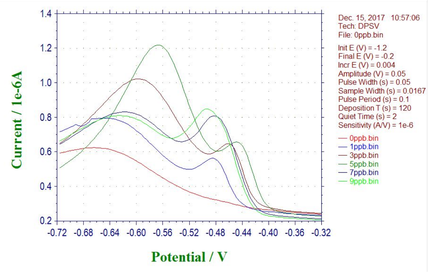

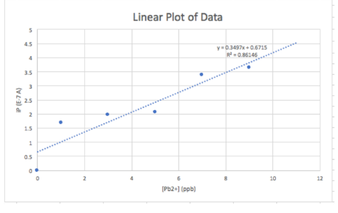

Conclusion

The presence of lead in drinking water as a result of industrial runoff and pipe erosion is a world health issue that must be addressed. However, the first step in doing so is being able to detect the presence of lead in a sample.

Through experimentation we have concluded differential pulse voltammetry to be an effective tool to address this problem for its sensitivity. We have also determined there is a positive correlation between lead concentration and current magnitude.

We will continue to expand on our goal of creating a portable electrochemical detection protocol by utilizing our lab's previously developed *AquaSift* device, a portable electrochemical analyzer. Our overarching research goal is to achieve a "just add water" approach, while still working towards creating a portable system.

Acknowledgements

The authors would like to thank the Clare Booth Luce Scholars Program from Santa Clara University for financial support. We would also like to thank Michigan State University's Fraunhofer Lab, especially Dr. Cory Rusinek, for their guidance with this research project.

References

[1] https://www.epa.gov/ground-water-and-drinking-water/basic-information-about-lead-drinking-water
[2] Jouhadi, Zineb, et al. "Lead Poisoning in Children: A Case Report." *Pan African Medical Journal*, vol. 24, May 2016, pp. 1-5.
[3] Hanna-Attisha, Monal, et al. "Elevated Blood Lead Levels in Children Associated with the Flint Drinking Water Crisis: A Spatial Analysis of Risk and Public Health Response." *American Journal of Public Health*, vol. 106, no. 2, Feb. 2016, pp. 283-290.
[4] Chaiyo, Sudkate, Amara Apiluk, Weena Siangproh, and Orawon Chailapakul. "High sensitivity and specificity simultaneous determination of lead, cadmium and copper using μPAD with dual electrochemical and colorimetric detection." *Sensors and Actuators B: Chemical* 233 (2016): 540-49. Web.
[5] Xing-Bao, Tao, et al. "Determination of Heavy Metals in Chinese Prickly Ash from Different Production Areas Using Inductively Coupled Plasma-Mass Spectrometry." *Tropical Journal of Pharmaceutical Research*, vol. 15, no. 8, Aug. 2016, pp. 1767-1772.

Exosome Tracking and Capture in Living Human Cells

Mai Anh Do | Daniel Levy | Dr. Biao Lu | Santa Clara University | Department of Bioengineering

Abstract

Exosomes are living nanoscale vesicles that can shuttle bioactive cargos for intercellular communication. The potential of these vesicles to serve as biomarkers for diagnosis of disease as well as vehicles for delivery of therapeutics has only begun to be explored.

Here we present a surface display strategy that enables exosome modification in living mammalian systems. By reconfiguring the surface protein CD63 or viral envelope glycoprotein VSVG, we generate topologically distinctive protein chimeras for the purpose of exosome imaging and capture in mammalian systems.

The genetically encoded protein chimeras had the ability to correctly target and integrate into exosomes in cultured human cells. Engineered exosomes were shown to endocytose into various mammalian cell lines when introduced. The secreted exosomes could be successfully captured by the affinity peptide intentionally displayed on the outer surface of exosomes. Our study highlights the potential of these fusion proteins for exosome tracking and provides novel genetic tools for exosome research and translation.

Approach: Surface Engineering

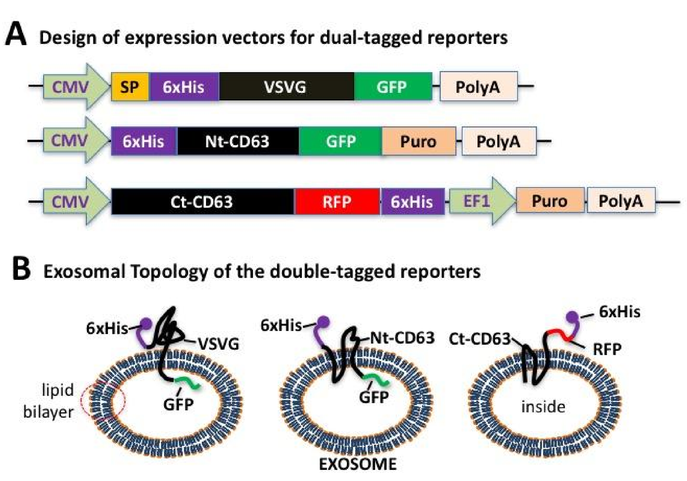

Figure 1: Design and construction of dual-tagged reporter protein for exosome tracking and capture
(A) Vector design for VSVG and CD63 fusion proteins. Fluorescent (GFP, RFP) and 6xHis-tag genes were attached as shown. **(B)** The schematic of dual loaded exosomes showing VSVG (black) transmembrane protein, GFP (green) or RFP (red) reporters, and 6xHis-tag (purple).

Results

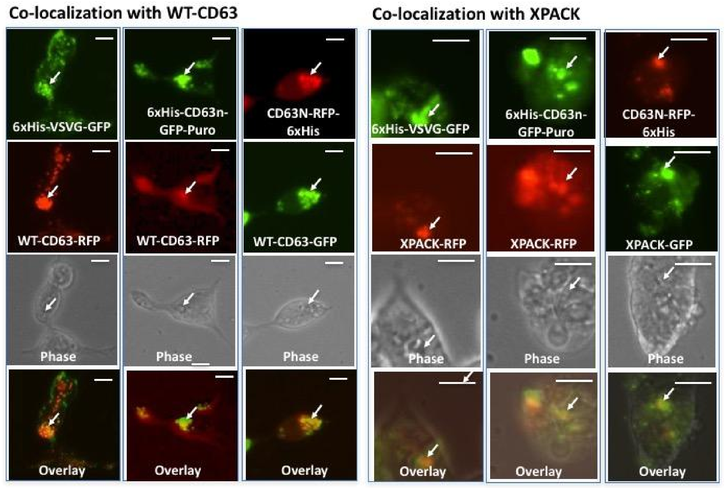

Figure 2: Colocalization of tracking molecules with exosome markers
HEK293 cells were cotransfected with our 6xHis-VSVG-GFP, 6xHis-CD63n-GFP, or CD63N-RFP-6xHis and known exosomal markers XPACK, and WT-CD63. After 48 hours incubation time, exosomes were observed to be colocalized in subcellular punctations.

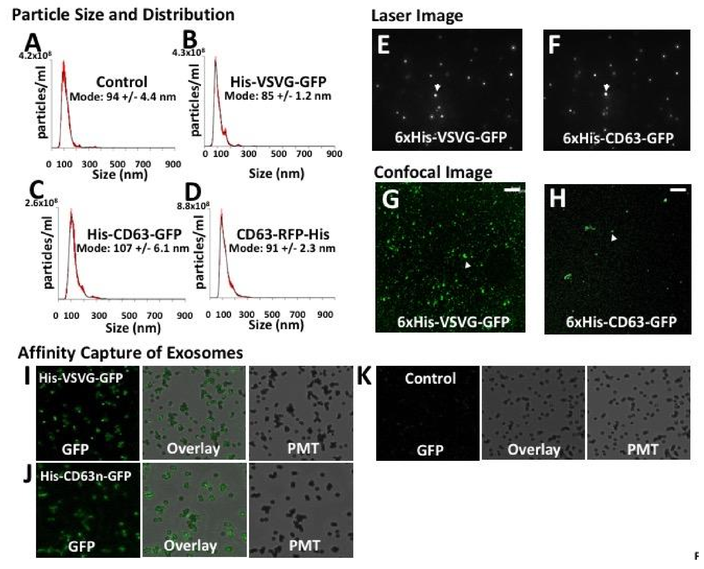

Figure 3:Characterization of exosomes released from producer cells
Exosomes were isolated from cell culture media of producer cells with Exo-Quick TC (System Biosciences). (**A-D**) Isolated exosomes were analyzed with Nanoparticle Tracking Analysis (Nanosight) indicating similar size distributions between our construct modifications and unmodified HEK293 exosomes.(**E-H)** Isolated exosomes were visualized with confocal microscopy. (**I-K**) Modified exosomes were captured on magnetic Dynabeads (ThermoFisher Scientific) via their His-tags and visualized via confocal microscopy.

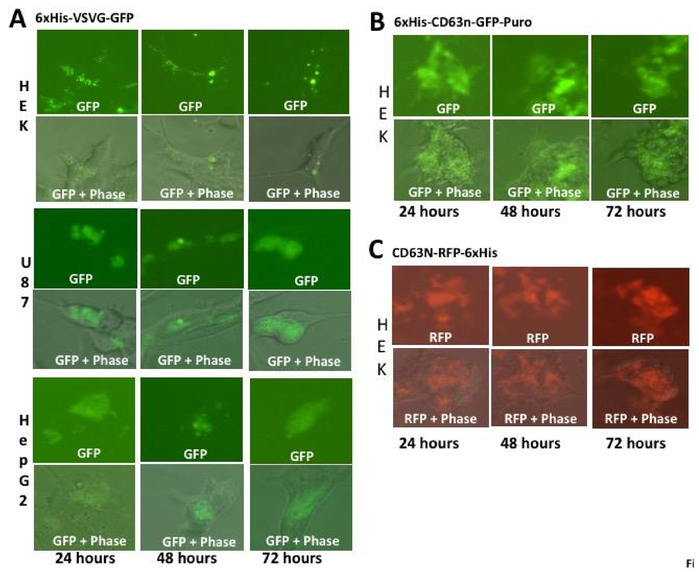

Figure 4: Mammalian cells can effectively uptake dual-tagged exosomes
(A) An uptake assay with 6xHis-VSVG-GFP modified exosomes in three different cell lines was performed in serum-free Ultra-Culture (Gibco). 24, 48, and 72 hours post assay, images were taken on a fluorescent microscope at 20x magnification to show the uptake within the cells. The same was done for 6xHis-CD63n-GFP-puro **(B)** and CD63N-RFP-6xHis **(C)** exosomes.

Conclusion

Our engineered molecular tools could be used to track and capture exosomes in living human cells.

Engineered exosomes have the potential to be loaded with molecules for drug delivery. We can also attach cell-specific molecules for targeted therapy or disease diagnosis.

References

Tkach, M., & Théry, C. (2016). Communication by Extracellular Vesicles: Where We Are and Where We Need to Go. Cell, 164(6), 1226-1232. doi:10.1016/j.cell.2016.01.043

Meyer, C., Losacco, J., Stickney, Z., Li, L., Marriott, G., Lu, B. (2017). International Journal of Nanomedicine. 12:3153-3170

Hassuna, N., Monk, P. N., Moseley, G. W., & Partridge, L. J. (2009). Strategies for targeting tetraspanin proteins: Potential therapeutic applications in microbial infections. BioDrugs, 23(6), 341–359. http://doi.org/10.2165/11315650-000000000-00000

Stickney, Z., Losacco, J., McDevitt, S., Zhang, Z., & Lu, B. (2016). Development of Exosome Surface Display Technology in Living Human Cells. Biochemical and Biophysical Research Communications, 472(1), 53–59. http://doi.org/10.1016/j.bbrc.2016.02.058

Santa Clara University
School of Engineering

Research in Multirobot Adaptive Navigation

Robert McDonald, Michael Neumann, Scot Tomer, Danop Rajabhandharaks, Ryan Cooper
Advisor: Dr. Christopher Kitts
Department of Mechanical Engineering
Santa Clara University
School of Engineering

Abstract

Multirobot Adaptive Navigation (MAN) involves moving a cluster of robots through a field of interest based on realtime sensor measurements in order to find features of interest. This capability has a variety of compelling applications and the potential to save significant time and energy compared to other strategies. This poster reviews several threads of our research program in MAN.

Our research team is a leader in this field. We are the first to demonstrate MAN extrema finding and contour following in the field. We are also the first to propose and verify controllers for ridge descent, trench ascent and saddle point positioning.

Background

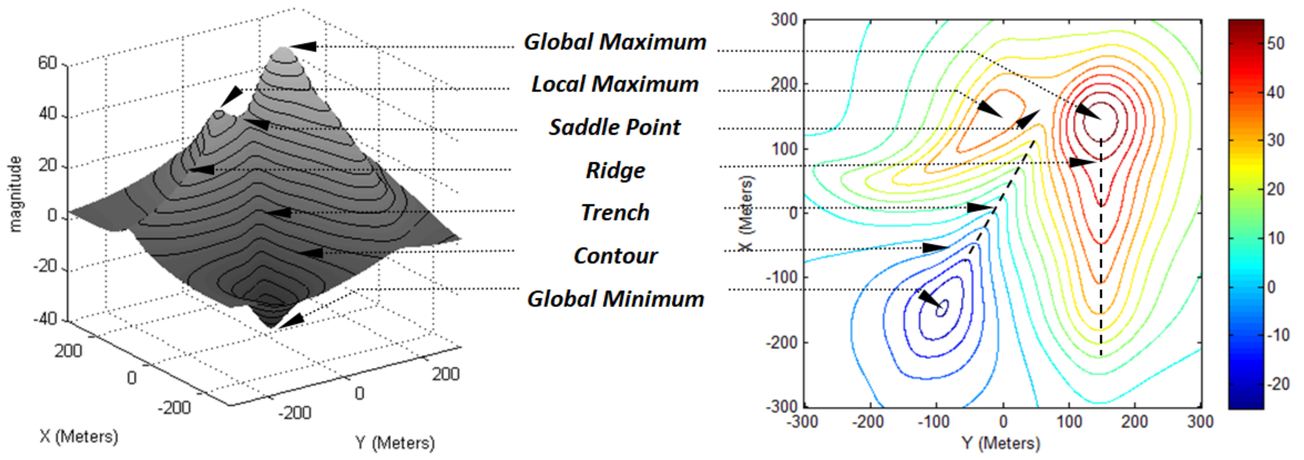

Critical Points within a Scalar Field: (left) 3D view of scalar surface, (right) overhead view of equivalent contour map

- Scalar fields associate one value, like temperature or pollution level, with each location in a field of interest.
- For planar regions, scalar values are depicted as the altitude of a surface at the sampled point in a plane
- Critical scalar field features include extreme points (min/max), contours, ridges/trenches, and saddle points.
- We have developed simple reactive controllers to move to/along each one of these features.

Real World Applications

Environmental Sensing – Find sources of and define the extent of pollution, locate anoxic and starvation zones, etc.
Disaster Response – Locate the source of harmful gases, establish safety perimeters, and find safe paths of minimum exposure
Exploration – Find caches of valuable resources, move efficiently between features of interest, explore while ensuring the provision of necessary operational services

Multirobot Adaptive Navigation has been hailed as a breakthrough technology capable of revolutionizing the way we characterize the environment, respond to disasters, and explore new worlds. Our work has set the performance bar for demonstrating these techniques experimentally and in field applications.

MAN Control Primitives

We have developed and verified via simulation a comprehensive suite of controllers to move to/along each critical feature of a scalar field.

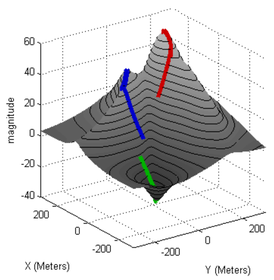

Moving up/down a gradient to go to the maximum/minimum in a field

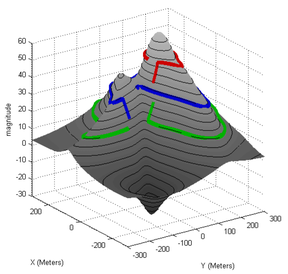

Moving along a contour by moving perpendicular to a gradient

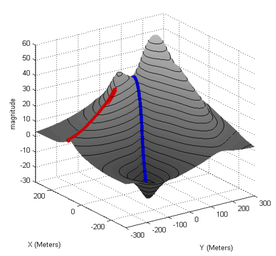

Straddling a ridge/trench to move down/up those features

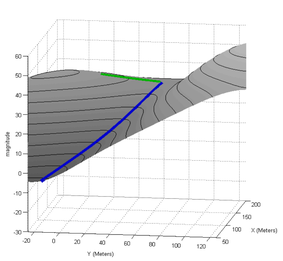

Terminating ridge/trench navigation through positioning on a saddle point

MAN Experiments

We've demonstrated the control primitives experimentally via autonomous kayaks in the field, and mobile robots in the laboratory.

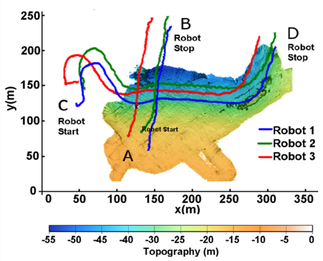

Three kayaks descending a gradient and following a contour in Lake Tahoe, CA.

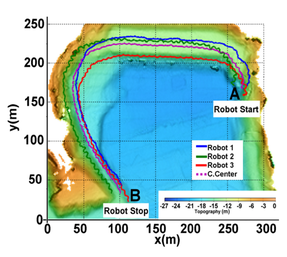

Three kayaks following a contour in Stevens Creek Reservoir, CA.

Five mini-robots navigating down a ridge in a laboratory testbed.

Several of the robotic clusters used for MAN experiments [1]-[2].

Adaptive Cluster Sizing

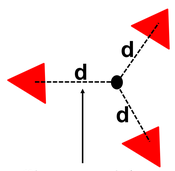

Cluster size definition

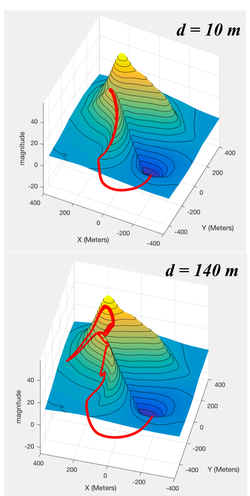

A simulation of a cluster of 3 robots detecting local and global extrema

- Most of our work to date has used symmetric robot clusters of a constant size.
- The ability to move to/along scalar field features is affected by the size of the cluster.
- We have found that the cluster size can be selected to filter out spatial noise and to "tune" navigation to be sensitive to features of certain sizes.
- We are now developing adaptive sizing capabilities to exploit this capability for real world missions.

Vector Fields

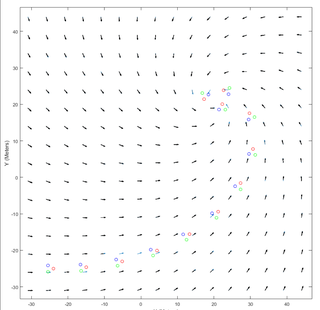

A simulation of a 3 robot cluster moving to the center of a vortex in a vector field.

- Vector fields describe flow fields and multi-parameter scalar fields.
- Vector field features include sources, sinks, vortices, and doublets.
- Vector field examples include fluid flow, wifi, electromagnetic fields, and color images.
- We're extending our MAN techniques for vector field navigation and have verified via simulation several candidate controllers.

Acknowledgements

Elements of this work have been supported by the National Science Foundation, NASA Ames Research Center, NOAA, the Monterey Bay Aquarium Research Institute, and the School of Engineering.

[1] T. Adamek, et al., "Gradient-Based Cluster Space Navigation for Autonomous Surface Vessels," *IEEE/ASME Trans on Mechatronics*, v20, n2, 2015, pp. 506-518.
[2] S. Tomer, et al., "A Low-Cost Indoor Testbed for Multirobot Adaptive Navigation Research," Accepted to IEEE Aerospace Conf., Big Sky, MT, March, 2018.

Ground Station Location Optimization and Remote Location Telecommunication

Leland Taylor; Dr. Michael Neumann; Dr. Christopher Kitts
Robotics Systems Laboratory || Department of Mechanical Engineering
Santa Clara University
School of Engineering

Background

In satellite operations, Earth-based antennae called ground stations (GS) are used to track, communicate with, and command satellites for a variety of missions. The satellite and GS can successfully communicate when their fields of view overlap. Depending on the satellite's orbit and the GS location, the characteristics and quality of this access time can vary greatly. In some cases, like that of NASA's Deep Space Network, the location of the GS can be critical to mission success. The goal of this research was to analyze access patterns generated by different satellite and GS combinations in order to develop "rules of thumb" for mission planning. This research then investigated and proposed a simple, low cost GS design to further reduce mission cost and provide satellite access to previously inaccessible and remote regions.

Orbital Access Analysis

Satellite orbital access was analyzed using an automated program which leveraged Satellite Tool Kit (STK), Matlab, and MySQL. In an STK simulation, GSs are placed at uniformly distributed locations of latitude and longitude to create a grid of GSs which spans the Earth. The amount of access time each GS has to the satellite is calculated and a contour plot of the result is made. This is a convenient way to visualize how a satellite's access pattern varies across the Earth. An example of these access patterns is shown below.

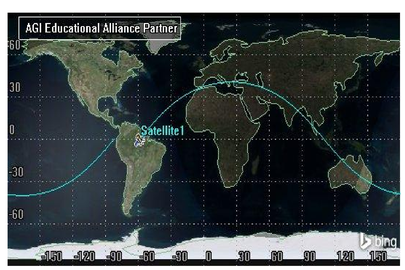

Orbit Ground Track in STK

Simulation parameters
- 30 days
- Circular orbit
- 300 km radius
- 40 degrees inclination

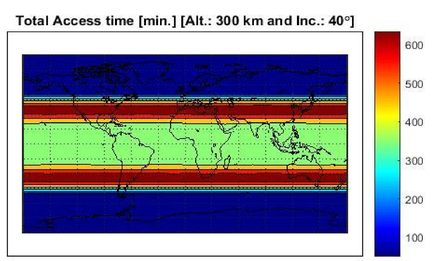

2D Access Contour Map in Matlab

Latitude of Max Access

Rule of Thumb: to maximize access time, the latitude of a GS should be slightly less than the satellite's inclination (inc). For a 300 km, circular orbit:
- If inclination < 10°, place GS at 0° latitude.
- If inclination > 10°, place GS at -10.3° + 1.08 inc.

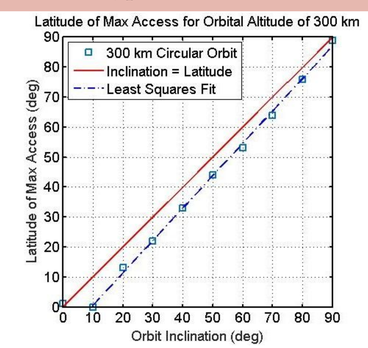

Case Study: DSN

Deep Space Network (DSN)
- 3 GS locations
  - Goldstone - U.S.
  - Madrid - Spain
  - Canberra - Australia
- Placed 120 degrees apart
- Provides uninterrupted coverage for satellites above 30,000 km
- Consists of a 70m main dish and a variety of smaller, 34m dishes at each site
- Costs millions of dollars for each site

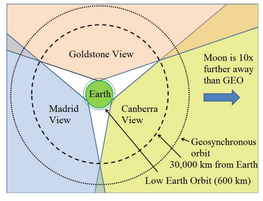

Ground Station Location Optimization

Another optimization problem is to determine the best location to place an additional GS, given one or more existing GS. If the satellite's orbit is known, the additional GS location can be tailored in order to optimize access time using the Ground Station Location Optimization (GSLO) program. To the right are figures showing the outputs of the GSLO program. Additional research is being done to take into account other parameters such as maximum time between contacts.

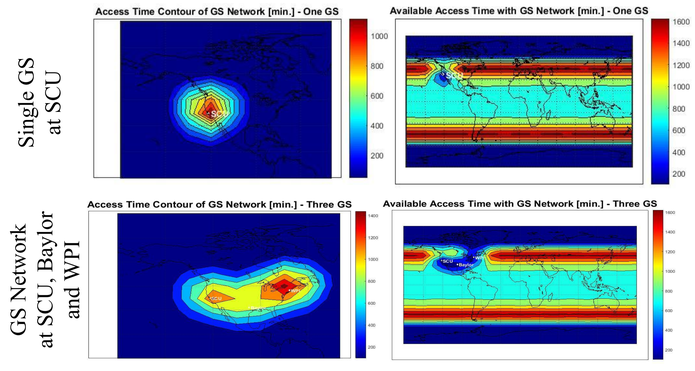

Access Time for Existing GS/GS Network

Access Time Increase for an Additional GS

Access and Inclination

Rule of Thumb: a polar or equatorial orbit will maximize access time (if a GS can be placed anywhere). The figure below shows maximum access time varying with orbit altitude and inclination.

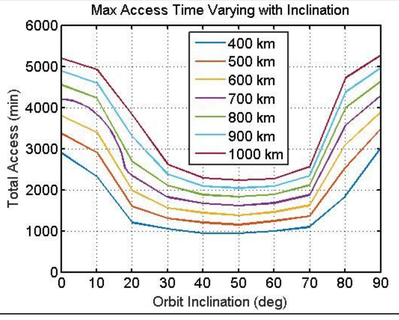

References

Altshuld, Max. *A Graphical Analysis Tool for Ground Station Availability Optimization*. Advisor: C. Kitts, SCU Master's Thesis, October 2013.

NASA. "Deep Space Network (DSN)". www.nasa.gov/directorates/heo/scan/services/networks/dsn. March 10, 2016

A special thanks to Dr. Christopher Kitts and Dr. Michael Neumann for their guidance and direction during the course of this research.

Remote Location Telecommunication System

An optimal GS location can often be geographically or logistically infeasible for traditional GS deployment. One goal of this research is to create a mobile, robust, and rugged GS that can be temporarily deployed in such remote locations. The Remote Location Telecommunication System (RLTS) was developed with the idea that it can be modified to meet specific missions' needs. The images to the right show the basic diagram and a photograph of the prototype during testing.

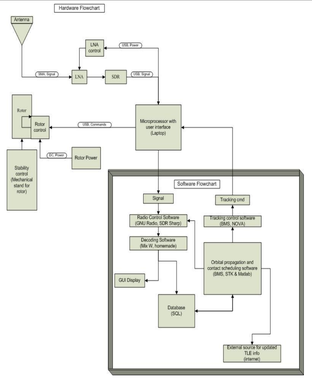

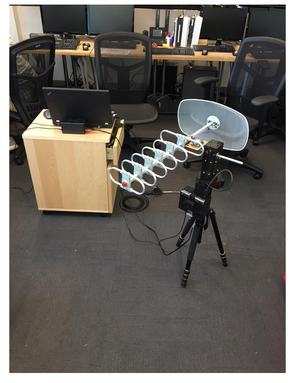

Future Work

- Develop user interface to streamline the orbital analysis and improve access to the database for analysis purposes.
- Simulations that test more exotic orbits.
- Transmission capability for the RLTS.
- Field testing, documentation, and deployment procedures for the RLTS.
- Optimization placement of an additional GS based on interval between access times.
- Optimization placement of an additional, receive only GS to provide state of health data at a specific time relative to primary GS access.

Material Property Analysis of Aluminum Ultrasonic Wedge Wire Bonds via Nano-Indentation

Jamie Ferris, Matthew McKay, Panthea Sepehrband
Department of Mechanical Engineering, Santa Clara University

What is ultrasonic wire bonding?

Ultrasonic wedge-wedge wire bonding is a fast, low temperature bonding method that is used commonly in electronic packages. However, the exact mechanics of bonding are unknown. Better understanding ultrasonic bonding would aid in the optimization of the process as well as application to other materials.

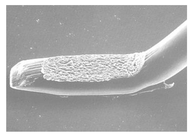

Ultrasonically bonded wire.[8]

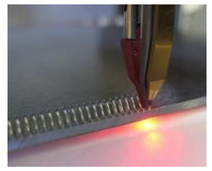

Ultrasonic wire bonding in process.[1]

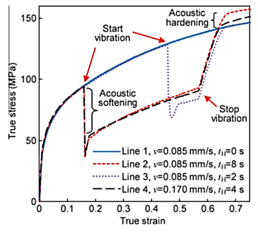

Theory of acoustoplasticity.[9]

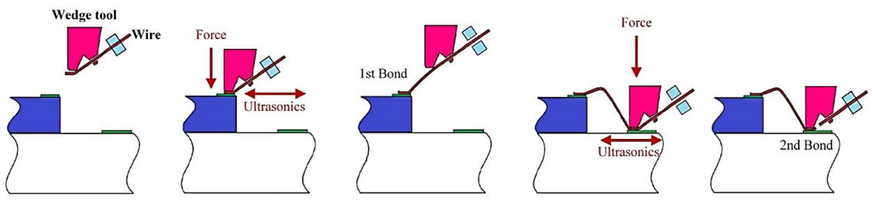

Ultrasonic wire bonding procedure.[4]

Our Goal:

- Use nano-indentation to evaluate the material properties across Al-Al ultrasonic wedge wire bonding interfaces.
- Contribute to the understanding and optimization of ultrasonic bonding by relating material properties at various bonding powers to atomic level structural changes

Thus far we have concluded micro-indentation and have established nano-indentation testing procedures. We recently began nano-indentation.

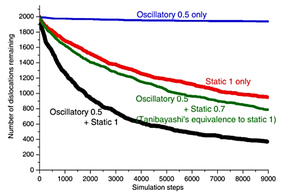

Dislocation cancellation via ultrasonic oscillation.[7]

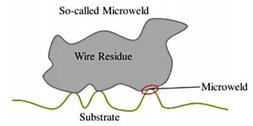

Microweld formation in ultrasonic bonding.[4]

Micro-Indentation Results

- Micro-indentations were taken across the bond interfaces with spacing 75 µm.
- Near the bond interface, where both plastic deformation and ultrasonic vibration occur, was harder.
- Near the middle of the wire, where only ultrasonic vibration was present, was less hard.

Micro-indentation results lacked enough resolution.
→ Nano-indentation

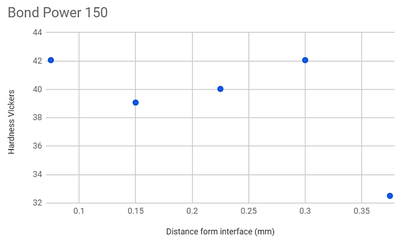

Hardness across bond interface found using micro-indentation.

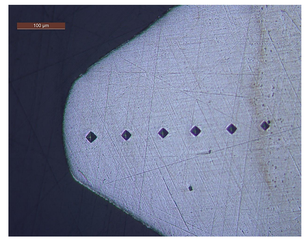

Micro-indentation on an Al-Al sample.

Nano-Indentation

1. Load-displacement data is measured by a Hysitron TI Premier nano-indenter.
2. Hysitron software calculates hardness (H), reduced elastic modulus (E^*), stiffness (S), and more.
3. We calculate elastic modulus (E), yield strength (σ_y), and strain hardening exponent (n).

Nano-indent image.[5]

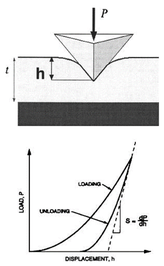

Nano-indentation.[2]

Ogasawara's Equations

Ogasawara et al.[6] has shown that mechanical properties of materials can be calculated from the results of nano-indentation by defining a representative strain to normalize a dimensionless function relating $\frac{E^*}{\sigma_r}$ to $\frac{C}{\sigma_r}$. Strain 0.0115 best normalized this relationship for the Berkovich indenter.

Assumptions: power law strain hardening and incremental theory of plasticity with von Mises effective stresses.

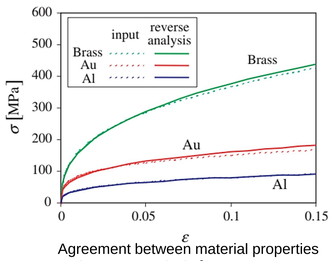

Agreement between material properties and reverse analysis.[6]

$$\frac{W_t}{\delta_{max}^3 \sigma_R \langle 0.0125 \rangle} = f\left(ln\ \frac{E^*}{\sigma_R \langle 0.0115 \rangle}\right)$$

$$\frac{S}{2\delta_{max} E^*} = f\left(n, ln\ \frac{E^*}{\sigma_R \langle 0.0115 \rangle}\right)$$

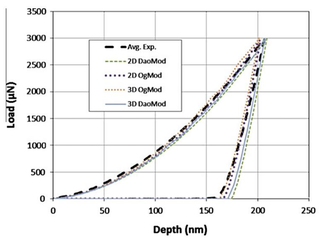

Comparison of experimental and simulated load-displacement curves.[3]

Nano-Indentation Results

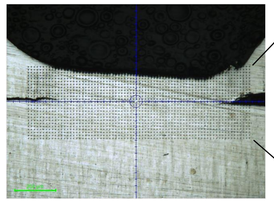

Nano-indentation data from an Al-Al sample at 255 bond power.

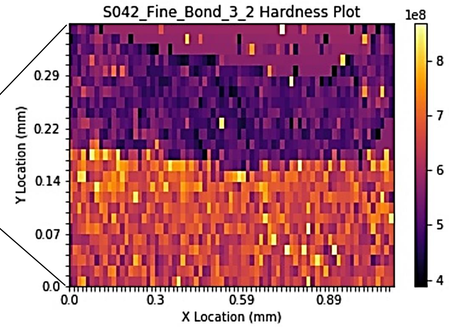

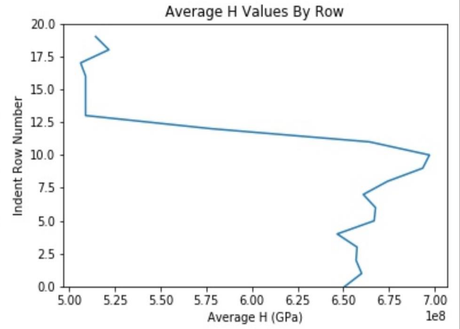

- Only slightly curved interface surface
- Substrate hardness increases near the interface
- Substrate hardness trending with the curve
- Wire hardness is not significantly increased

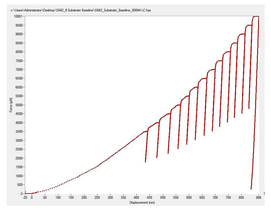

Material	Published E Value	Average Measured E Value	Measured Standard Deviation/ Average
Substrate (5052-O Al)	70.3 GPa	86.9 GPa	4.11%
Wire (99.99% Al)	68.0 GPa	65.4 GPa	3.54%

References
[1] Brökelmann, Michael. "Active Vibration Control in Ultrasonic Wire Bonding." *Hesse GmbH*, Dec. 2014, www.hesse-mechatronics.com/en/active-vibration-control-in-ultrasonic-wire-bonding/.
[2] den Toonder JM, et al. *J. Electron. Packag.* 2004;127(3):276-285.
[3] Harvey, Evan, et al. *Mechanics of Materials*, vol. 52, 2012, pp. 1–11.
[4] Long, Yangyang, et al. *Journal of Materials Processing Technology*, vol. 245, 2017, pp. 241–258.
[5] "Nanoindentation." *Wikipedia*, Wikimedia Foundation, 27 Dec. 2017, en.wikipedia.org/wiki/Nanoindentation.
[6] Ogasawara, Nagahisa, et al. *Scripta Materialia*, vol. 54, no. 1, 2006, pp. 65–70.
[7] Siu, K.w., et al. *International Journal of Plasticity*, vol. 27, no. 5, 2011, pp. 788–800.
[8] "Wire Bonding." *The Nordic Electronics Packaging Guideline*, extra.ivf.se/ngl/a-wirebonding/chaptera1.htm.
[9] Yao, Zhehe, et al. *International Journal of Plasticity*, vol. 39, 2012, pp. 75–87.

Simulation of Lipid Membrane Rupture via Cellular Automation

Abhay Gupta[1], Irep Gözen[2], and Michael Taylor[1]
[1]Department of Mechanical Engineering, Santa Clara University. [2]Centre of Molecular Medicine Norway, University of Oslo.

Introduction

Lipids are the fundamental structural component of biological cell membranes. Under tensile stress, these membranes form transient ruptures. Unchecked membrane ruptures are implicated in serious ailments such as muscular dystrophy, CTE, and vibration white finger. Understanding and controlling rupture formation has important implications in, e.g., gene therapy and drug delivery.

In model double bi-layer lipid membranes spreading on a solid surface, several rupture morphologies have been observed, including floral and fractal patterns [1]. Unfortunately, the underlying mechanics are too small to observe experimentally.

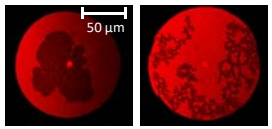

Floral Fractal

Objectives

The primary goal of this research is to develop a computational model for rupture in lipid membranes, examining specifically *why different fracture morphologies appear* and *how the fracture morphology is a function of membrane properties and lipid structure*. Research activities include

- Develop a 2D Cellular Automation of lipid membrane pinning and rupture using Matlab
- Make qualitative comparisons of simulation results with experimental data

Cellular Automation

Cellular automation (CA) is a discrete numerical model consisting of a grid of cells that can take on one of a finite set of states (e.g., on or off). The state of a cell is changed, or evolved, according to very simple rules based on the state of its neighbors. It has commonly been used to describe fluid movement through porous structures as well as growth and decay areas in ecology [2,3].

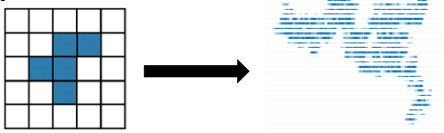

Generation: 1 **Generation: 4000**

Simulation Overview

The simulation of these rupture patterns was created through manipulation of two properties. The first property is the probability of pinning sites and cluster. A pinned site is a node that has the bottom and top layer of the bilayer connected, while a cluster is a chain of these pinned sites across the bilayer. Each site has a tension value that is linearly proportional to the radius of the bilayer:

$$T = \frac{R_{annulus} - R_{pinradius}}{R_{max}}$$

And each pinned site has constant bond strength determined by the following equation:

$$B = \left(\frac{19}{32}\right)^{C} (B_o)(C+1),$$

where c is the number of cells in that cluster.
If this tension exceeds the bond strength of the pinned site or a cluster, a rupture occurs. After a rupture occurs, new pinned sites and clusters are formed through the dispersion of energy and are given a specified bond strength. The new bond strength is determined through an adjustment equation:

$$B = B_o + (\mathrm{T} - B_o)\, f$$

The second probability is the distribution of pinning sites and clusters across the spread bilayer. The higher probability of cluster formulation causes a higher probability of fractal rupture, while a higher pinning probability results in alternate rupture patterns. A higher density of pins in the overall bilayer will cause a floral rupture due to chains of circular rupture. Alternatively, a low density of pins will result in single circular rupture.

Algorithm

1. Create initial state of circular lipid CA cells
2. Expand lipid by one cell radially
3. Determine whether cell becomes a regular pin or cluster pin site based on user-defined probabilities P_n and T, respectively
4. Compute tension in pinned cells
5. Invasion percolation routine to determine cluster growth throughout lipid
6. Recompute tensions in pinned cells
7. If tensions are greater than a critical value B, cells "fracture" and release energy as dictated by whether they are a regular or cluster pin
8. Loop back to 2 and repeat for N generations

Results

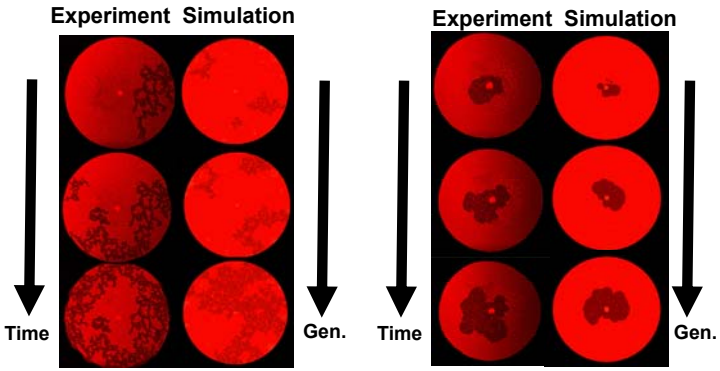

Summary and Future Work

The simulation shows good quantitative accuracy to the experimental results across a range of rupture morphologies. This provides some evidence that the pinning can contribute to the appearance of the different morphologies found in the lab.

However, further investigation must be made in order to quantitatively justify these results and determine how to utilize them to control or eliminate ruptures completely. These quantitative studies include determining the dimension of the fractal pattern and the area of fracture for floral patterns, as well as comparing the rates of fracture among all rupture patterns.

References

[1] Gözen et al. Fractal avalanche ruptures in biological membranes. *Nat. Mat.* 9, 908-912 (2010).
[2] O'Sullivan & Perry, *Spatial Simulation: Exploring Pattern and Process*, Wiley-Blackwell, 2013.
[3] Feder & Torstein, *Fractal Patterns in Porous Media Flow*, Fractals in Geology and Earth Processing, 1996.

Acknowledgements

This work has been supported by the Kuehler Undergraduate Research Grant administered by the SCU School of Engineering.

60 GHz Cavity Backed Patch Antenna Array

Kasey Chun, Master's Student; Dr. Ramesh Abhari, Advisor
Department of Electrical Engineering

Santa Clara University
School of Engineering

Motivation:
5G and next generation wireless technology will be centered around the 60 GHz range which can support higher data rates and currently serves as an untapped bandwidth.

Objectives:
Investigate the design of 60 GHz patch antenna arrays and experiment with cavity backed systems to reduce the amount of unwanted coupling in tightly packed systems.

Design and Simulations

Dielectric Info: Rogers 04350; εr = 3.66; H = .508 mm; tanD = .0037

Patch: 1.64 x 1.03 mm

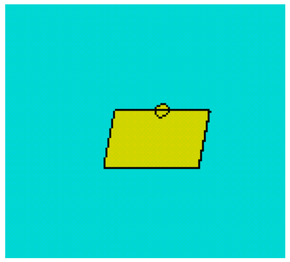

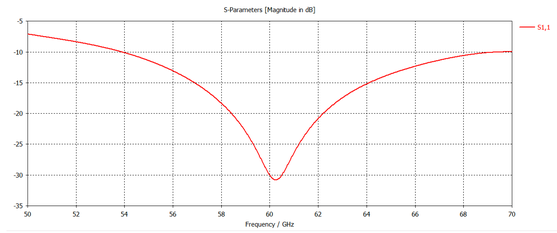

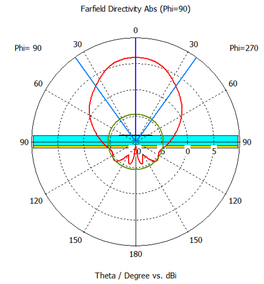

Patch: 1.64 x 1.03 mm
Cavity: 2.16 x 2.67 mm
CWxCL: 0.26 x 0.82 mm
Via Diameter: 0.2 mm
Via Spacing: 0.47 mm

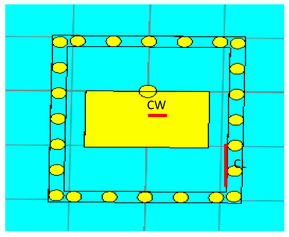

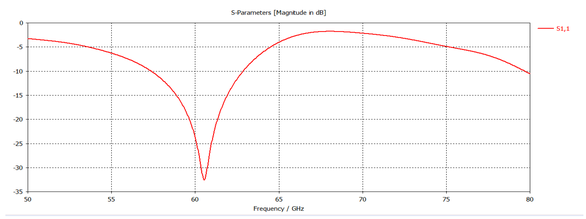

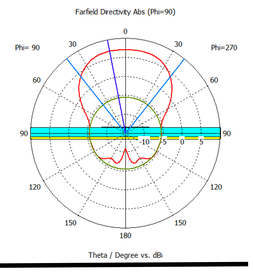

Patch: 1.5 x 1.7 mm
2x2: 4.89 x 4.48 mm
Feed: 0.539 x 0.72;
0.427 x 0.728;
0.297 x .739

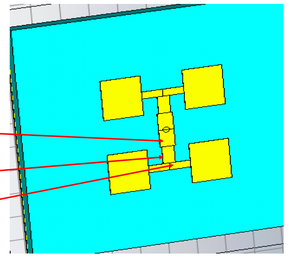

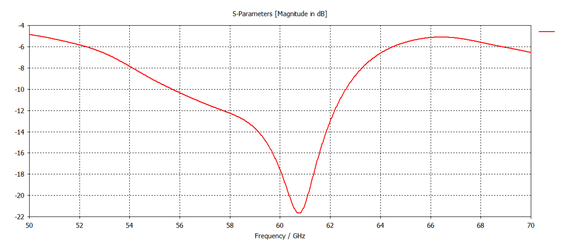

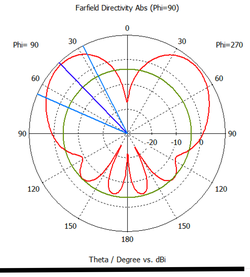

Patch: 1.5 x 1.7 mm
Cavity: 6.76 x 6.91 mm
CWxCL: 0.93 x 1.21 mm
Via Diameter: 0.2 mm
Via Spacing: 0.47 mm

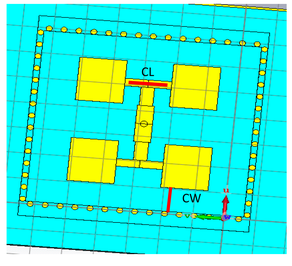

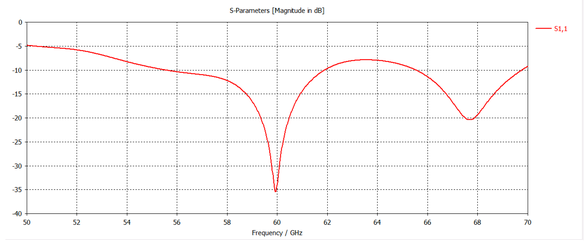

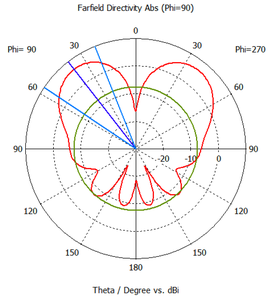

Antenna	Gain	HPBW	S11 BW	FTB Ratio
Single	6.11 dB	71.2 deg	15.1 GHz	10.8 dB
Single w/ Via	6.93 dB	76.5 deg	5.5 GHz	12.55 dB
2x2	8.6 dB	39.5 deg	6.9 GHz	12.82 dB
2x2 w/ Via	7.2 dB	34.3 deg	8.3 GHz	14.06 dB

2x2 Feed Design:
The feed design minimizes the amount of energy loss by matching ¼ wave T-lines from a low to high characteristic impedance path from input to patch.

Conclusion:
From the results I found that designing a via cavity fencing can have major effects on the radiation pattern, directivity, bandwidth and beamwidth of a patch antenna, with different configurations yielding different results.

Next Steps:
Fabricate the 4 different boards and measure their return loss versus frequency and radiation pattern.

Evaluation of Biological Tissues for Wireless Power Transfer in Microwave Hyperthermia

Nivedita Parthasarathy, PhD Student; Dr. Ramesh Abhari, Advisor
Department of Electrical Engineering
Santa Clara University
School of Engineering

Motivation:

- Evaluation of the dielectric properties of biological tissues is an important aspect of studying radiation absorption in various biomedical applications including Microwave Hyperthermia.
- Hyperthermia is a medical procedure that involves elevating the temperature of tumor cells by means of a microwave applicator.
- Controlled exposure to microwave radiation destroys cancer cells which makes hyperthermia an effective form of non-invasive radiation therapy.
- Wireless Power Transfer in the 5.8 GHz range is studied to determine radiation absorption.

Objectives:

1. Design of microwave applicators to evaluate power absorption in layered tissue medium. These include 3D stacked Yagi-Uda antennas to provide focused radiation and coupled coils for efficient power transfer.
2. Design of a suspended microstrip ring resonator to extract the dielectric permittivity and loss tangent. These are important dielectric properties that determine the dispersive nature of biological tissues at different frequencies.
3. Study of radiation patterns, Power loss density and SAR, and S-parameters with Computer Simulation Technology (CST) Microwave Studio Suite.

Design of Hyperthermia Applicators: Double-Sided Printed Yagi Antenna

Front and Back Views of Printed Yagi Antenna with Partial Ground Plane Reflector

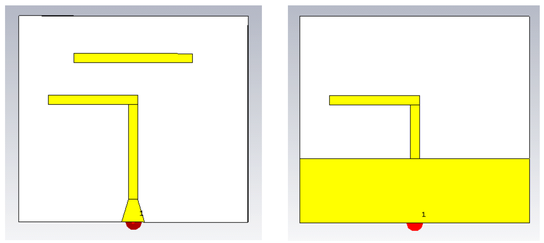

Analysis of 3D Stacked Antenna Arrays

Fullwave Electromagnetic Simulation in CST S-Parameter and Radiation Pattern

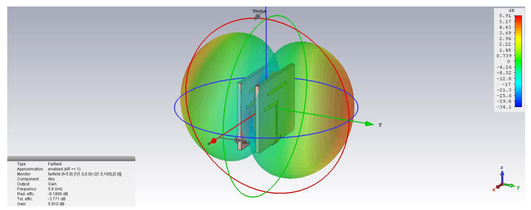

Isolation Enhancement with Parasitic Dipole Plane Stacked between Planar Arrays

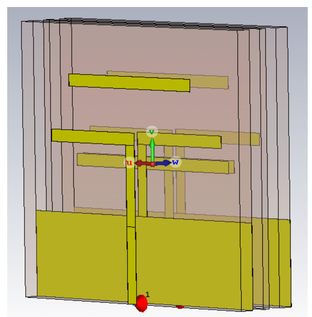

Design and Setup of Suspended Microstrip Ring Resonators

Ring Resonator with Fat Tissue Sample

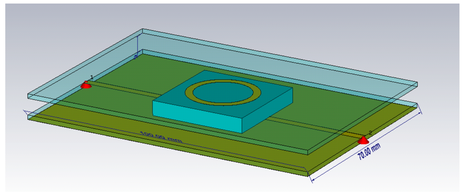

Determining the Dielectric Permittivity and Loss Tangent from Varying Sample Values

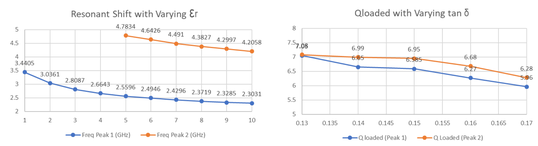

Sample System for Wireless Power Transfer to mm-sized Implant

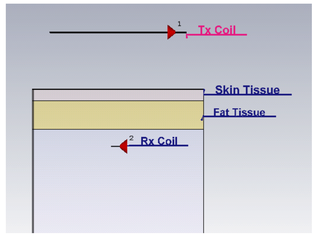

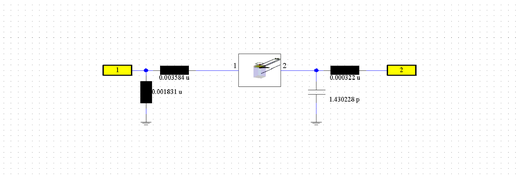

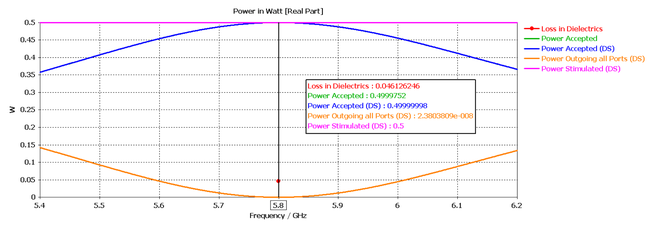

Key findings of this project:

- Stacked Yagi antennas provide high-gain endfire radiation that allows for focused radiation inside human tissue.
- Ring resonators can be used to effectively determine the dielectric properties of biological tissues at various frequencies.
- Resonant coupled coils can generate efficient transfer when the receiver implant is small when compared to its depth inside the body.

Preliminary Experiments:

- The use of parasitic dipoles and stacked arrays enhance isolation while the double-sided design makes for easy fabrication.
- Ring Resonators can effectively determine the dielectric properties of homogenous tissues by recording of shifting resonant peaks and Q-loaded from S-Parameter results.

Next steps:

- Study of electric field propagation in muscle tissue to record anisotropic nature of tissue with ring resonator.
- Development of prototypes and a power transmission test set-up to validate design and simulations of 3D Yagi-Uda antenna as a hyperthermia applicator and study power transfer efficiency at the skin-fat interface.

Field Pattern Measurement of Beam-Switching Planar Antenna Array with Modified Butler Matrix in SIW at 60 GHz

Benjamin Horwath, PhD Student; Dr. Ramesh Abhari, Advisor
Department of Electrical Engineering
Santa Clara University
School of Engineering

Summary: After fabricating antenna system prototype, measured 3D E-field pattern to compare performance to design goals and simulations. Test board consists of 4 input connectors, microstrip-to-SIW (substrate integrated waveguides) transitions, a Butler Matrix circuit modified to feed a planar array, and a 2x2 planar microstrip antenna array.
Objective: Construct a positioning system and antenna test range to measure 3D field pattern of a beam-switching antenna array at 60 GHz.

Target Specs: Need to collect E-field strength in a hemisphere around the antenna-under-test (AUT):
- Fixed radius: Fraunhofer distance, $d_f > 2D^2/\lambda_0$=9cm , Elevation angle: semi-rotation of horn antenna, $-90° < \theta < 90°$, Azimuth angle: full rotation of AUT, $0° < \phi < 360°$

Positioning System Design Flow:

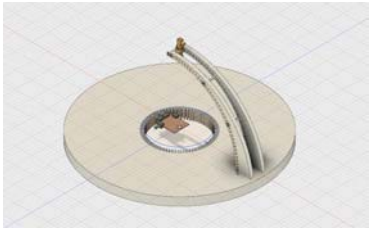

Autodesk Fusion 360:
- 3D conceptual design
- Export artwork and 3D object files

Iterate Design

Maker Lab:
- 3D printing platform and pegs
- laser cutter for base and arms

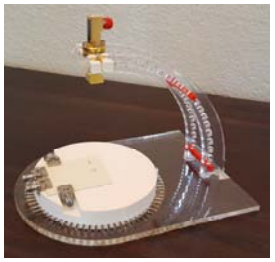

Final rig:
- Rotate horn antenna & AUT in 5° increments

Antenna Test Range:

Components:
- Data collection (Anritsu VNA in CNS Lab)
- Anechoic Chamber (needed to build)

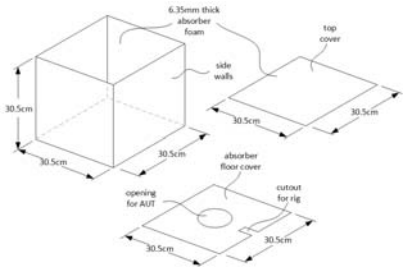

Results:

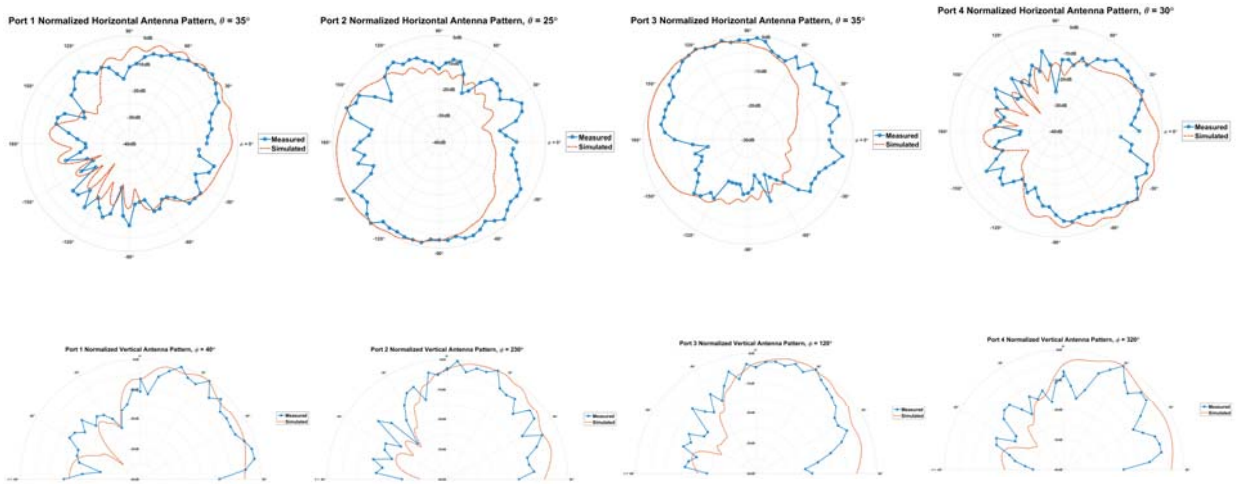

Conclusions:

- Measurement error sources:
  - Physical adjustment of AUT and horn antenna
  - Moving & replacing anechoic chamber walls, re-routing cables between data collection steps
- How to improve:
  - Reduce the number of times the operator must handle the test setup by automation and/or multiple calibrated test cables
  - Get better resolution with motor controls

Multi-Port Dual Polarized Integrated Patch Antenna for RF Detection at 5.8 GHz

Jonathan Lee
Advisor: Dr. Ramesh Abhari
Department of Electrical Engineering
Santa Clara University
School of Engineering

Motivation:

- Innovative design of antennas is a key factor in implementing compact and energy efficient wireless devices, particularly in new 5G wireless system designs [1]
- One approach to realize this objective is by using a multi-port antenna design, realized through inductive loops [2]
- Multiport antennas can be accessed by more than one sub-system at the same time and allow for implementing a number of design goals such as RF energy harvesting, pattern reconfiguration [3], environmental sensing, RF identification (RFID) [4]
- Also allows additional circuits to be integrated into a system without sacrificing space or portability

Objectives:

- Design and implement a multiport patch antenna to detect both horizontal and vertical polarization
- Create inductive coupling feeds for direct integration with RF chips
- Optimize all ports for maximum power transfer
- Ensure that antenna's radiation performance is not adversely affected by addition of extra ports into system

Design Steps:

- Square patch optimized for desired center frequency of 5.8 GHz
- Design T-junction feed network for maximum power transfer to Port 1
- Design inductive loops for conjugate impedance matching to RF-DC rectifier circuit – in this case, RF diode with 10+j40 Ω input impedance
- FR-4 substrate with $\varepsilon_r = 4.3$ used as PCB material
- Final optimized dimensions are shown in table below:

L1	3.7 mm	W3	0.41 mm	Winset	2.12 mm
W1	0.69 mm	Wloop	0.24 mm	Linset	1.07 mm
L2	8.5 mm	L4	0.98 mm		
W2	0.18 mm	L5	1.7 mm		
L3	10.3 mm				

Antenna Design and Measurement

Simulated Model and Fabricated Antenna

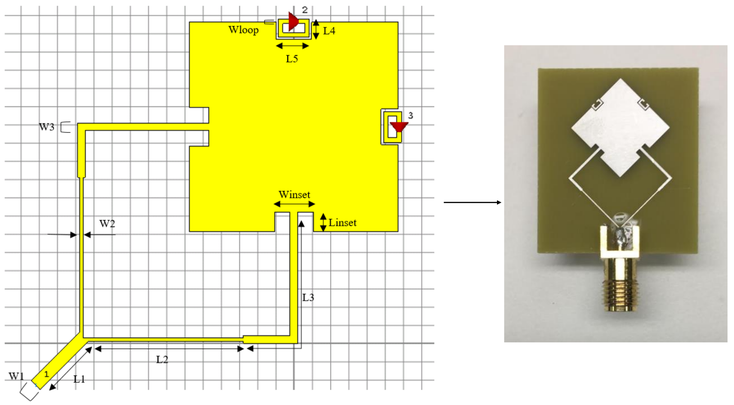

Radiation Pattern Comparison, Port 1 Excitation, Gain

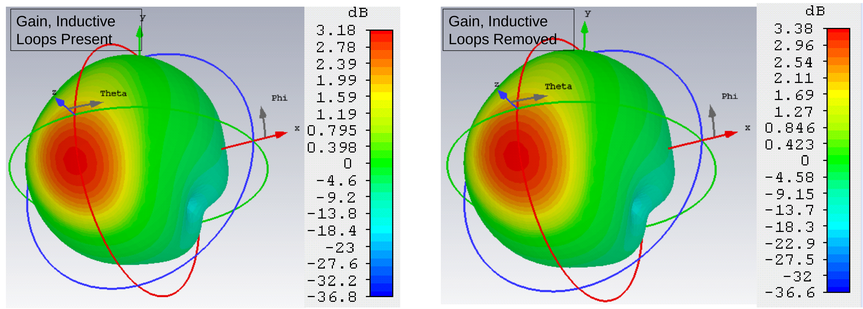

Selected Results

Simulated Input Impedance at Ports 2 and 3

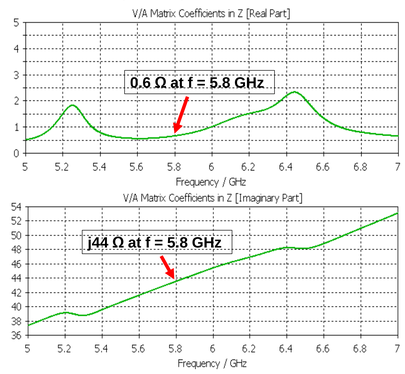

S11: Measured (Blue) vs Simulated (Red)

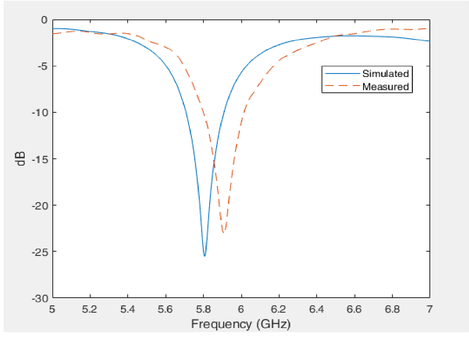

Key findings:

- Far-field simulation of the patch antenna demonstrates radiation gain of 3.18 dB at 5.8 GHz
- When inductive loops are removed, radiation gain of 3.38 dB is obtained from simulations, which is only 0.2 dB lower
- The simulated input impedance of the inductively coupled loops at Ports 2 and 3 is found to be 0.6 + j44Ω at 5.8GHz indicating complex matching to RF energy harvesting diodes
- The simulated return loss at Port 1 in Fig. 3 shows S11 < -25 dB at 5.8 GHz
- Measured S11 of the manufactured prototype closely follows the predicted simulation result with a small frequency shift of 1.7% which is attributed to fabrication tolerances

Next Steps

- Integrate energy harvesting chips and/or polarization detection circuits to provide additional level of functionality in desired wireless system
- Arrange antenna element in a linear array to improve RF characteristics such as gain
- Investigate viability of miniaturization techniques on patch and feed geometry
- Improve port isolation between loops and direct attach feed

References

[1] Y. Liu, Y. Zhang, and S. Xie, "Integrated energy and spectrum harvesting for 5G wireless communications," IEEE Network, vol. 29, no. 3, pp. 75-81, 2015.

[2] H.-W. Son and C.-S. Pyo, "Design of RFID tag antennas using an inductively coupled feed," Electron. Lett., vol. 41, no. 18, pp. 994–996, Sep.2005

[3] Y. Q. Wen, B. Z. Wang and X. Ding, "Planar Microstrip Endfire Antenna With Multiport Feeding," in IEEE Antennas and Wireless Propagation Letters, vol. 15, pp. 556-559, 2016.

[4] A. Abdulhadi, Y. Ding, M. Parvizi, and R. Abhari, "Multi-port UHF RFID tag antenna for enhanced energy harvesting of self-powered wireless sensors," in Proc. IEEE MTT-S Int. Microw. Symp. (IMS), Jun. 2014, pp. 1-3.

Proof of Concept for Tunable Periodically-Loaded Substrate Integrated Waveguide Phase Shifters

Rouzbeh Edalati, MSEE Student; Rudy Lopez, MSEE Graduate; Dr. Ramesh Abhari, Advisor
Department of Electrical Engineering

Santa Clara University
School of Engineering

Introduction

- RF Phase Shifter: Provide a needed phase shift and operate at RF frequencies not base band.
- Many different active and passive types such as loaded or switched transmission lines or Waveguides, MEMS, RFICs, ferromagnetic, substrate integrated waveguide (SIW).
- Application in phased array antennas and RF front end of various communication, radar, medical imaging and sensors systems.

SIW Phase Shifter

- SIW is a traditional waveguide adapted to PCB technology by using via fences as its side walls.
- Phase shifting in SIW can be accomplished by considering a specific delay length L_{WG} for SIW.
- The length L_{WG} can be shortened by allocating slots on SIW top wall.
- Also the phase shift may be increased by adding capacitors to the slots.

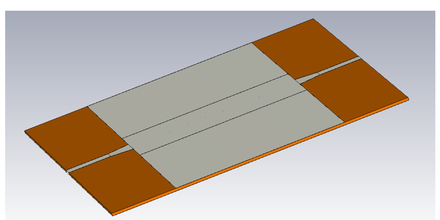

Slotted SIW (below)

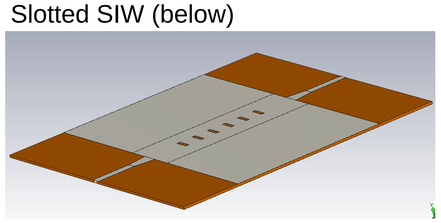

Objective

- Developing a cost-effective SIW Phase shifter technology.
- Provide means for tuning the phase shift.

Design

- Frequency: 15 GHz

Critical Dimensions & Values
Lcell = 3 mm
Gx = 2.0 mm
Gy = 0.6 mm
Wt = 2.2 mm
Wg = 7.8 mm
Wms = 1.2 mm
TL Imped. = 50 Ohms
Cg = 0.1pF - 0.6pF
Substrate: RO 4350B
Subs Thickness: .508 mm

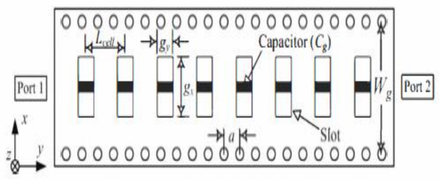

SIW Side Walls

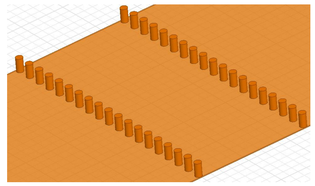

- Via diameter = .4 mm
- Via pitch = .8 mm
- Wall spacing = 2.2 mm

Simulation Results

- Without capacitors

Phase Difference Comparison (Slotted vs. Non-Slotted)

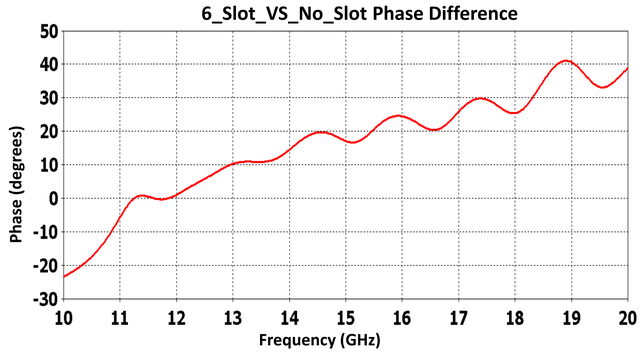

- Next parametric studies were conducted to characterize phase shift and insertion loss for variable slot dimensions and different number of capacitors.

Mean phase Difference vs Slots

# of Slots	Simulated Phase Shift (deg)
0 --> 2	36.4
2 --> 4	2.1
4 --> 6	0.8
6 --> 8	2.9
AVG	10.55
Total 0-->8	42.2

Prototypes Fabricated

- From left to right: Unloaded set, Cap-loaded set, Cap-Loaded w/ coax SMA connector

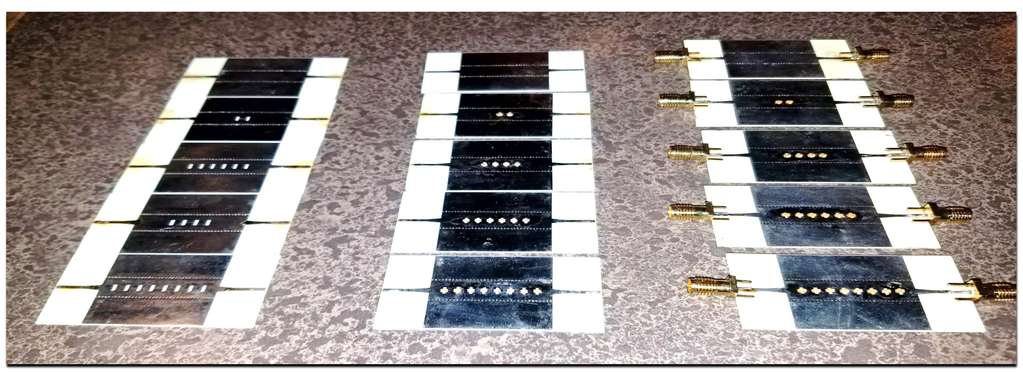

Measurement Results

- Simulation Vs Measured (No Capacitors)

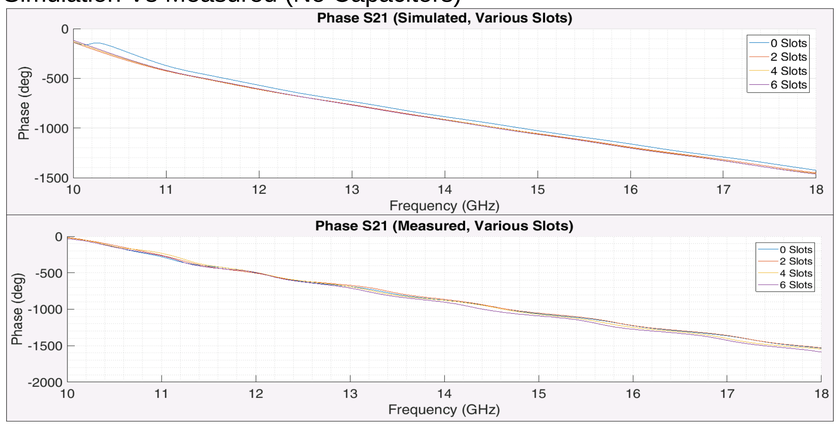

TRL Method For De-embedding the effect of connectors and transitions

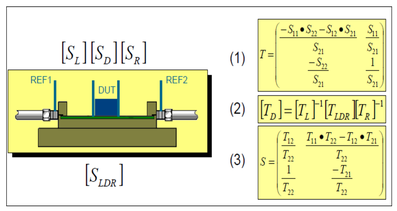

[1] Chad W.Morgan , "Obtaining Accurate Device-Only S-Parameter Data to 15-20 GHz Using in-Fixture Measurement Techniques" , February 3, 2004, Tyco International Ltd.

Mean Measured Phase For 6 Slot Cap Loaded SIW

Capacitance	Simulated	Measured
.1 pF	-802	-768
.2 pF	-2202	-891
.3 pF	-1903	-669
.4 pF	-752	-671
.5 pF	-761	-698
.6 pF	-764	-693

Conclusions

- Confirmed phase shift increase due to increased number of slots.
- Confirmed phase shift change due to placement of lumped capacitors over the slots.
- These capacitors can be replaced with variable capacitors to make a tunable phase shifter.
- Lack of quality connectors degraded S21 significantly.

Next Steps

- TRL Method should be used for de-embedding the effect of connectors and transitions.
- The TRL method consists of physically constructing two or more through lines which differ in length, in addition to an open or short circuit reflection. The S-parameters of these standards are measured and used in a set of matrix equations to extract the S parameters of the connectors and their junction to a device under test. Our goal is to obtain this characterization and remove the effects of the sub-optimal connectors and their junctions from our collected data.

System Level Electromagnetic Compatibility Remedy Using Absorbing Frequency Selective Surfaces

Ali Khoshniat and Ramesh Abhari
Department of Electrical Engineering, Santa Clara University
akhoshniat@scu.edu, rabhari@scu.edu

Santa Clara University
School of Engineering

Motivation

- Absorbing Frequency Selective Surfaces (FSS) can be used for system level mitigation of Electromagnetic Compatibility (EMC) issues.

Objective

- Design a Frequency Selective Surface (FSS) to match to the wave impedance of 377 Ω at 8 GHz. The FSS is placed inside the top wall of a metal box to absorb rather than reflect the radiations caused by components on a board and reduce leakage of emission through the gaps and ventilation slots.

Design Methodology

- Geometry of a unit cell of FSS is optimized to match the wave impedance using Resistive Nickel Phosphorus alloy (99,000 S/m) and thickness of 0.1 μm film yielding w= 3.525 mm and g= 1.075 mm.
- The substrate material is FR406 with thickness of d= 1.5748 mm, ε_r= 3.93, and tan δ= 0.0167.

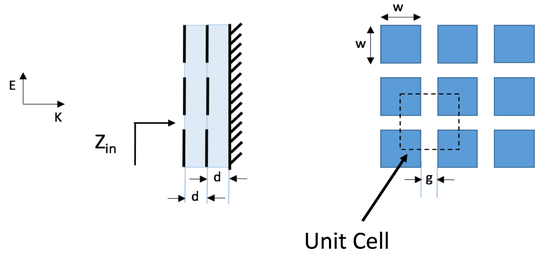

- Both real and imaginary parts of Zin change with the incidence angle.
- At 0° the impedance is almost Re[Z_{in}]= 377 Ω and Im[Z_{in}]= 0 Ω close to a perfect match to wave impedance but this changes as the angle changes (especially the imaginary part).
- This results in reduction of absorption from 32 dB at 0° to 20 dB at 30°.

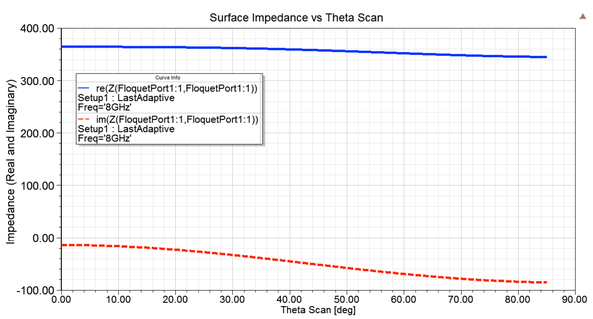

Simulation of Emissions from the System Box

- The system board under test is an RO4003C dielectric substrate with εr= 3.55 and the thickness of 1.524 mm which is placed on the floor of the box.
- A total of 9 square patches with the dimensions of 19.4 mm by 19.4 mm each represent potential active components on different locations inside the box (one excited, others terminated).
- Patches are spaced by 40 mm in x and 30 mm in y directions.

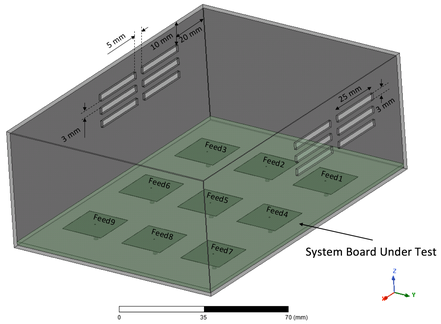

- The two-layer FSS absorber, a 29x20 array of small resistive patches is placed on the ceiling wall of the aluminum box.

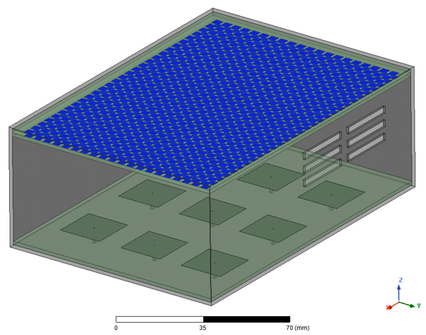

- From full-wave simulations, maximum radiated electric field (far-field) is determined for each active feed.

Excitation Point	Simulated Emission (dB)			Measured Emission (dB)		
	w/o FSS	w/ FSS	Emission Reduction	w/o FSS	w/ FSS	Emission Reduction
Feed 1/3	1	-9	10	-44	-50	6
Feed 2	3	-3	6	-39	-44	5
Feed 4/6	-1	-8	7	-41	-48	7
Feed 5	2	-4	6	-38	-46	8
Feed 7/9	-5	-10	5	-43	-51	8
Feed 8	-1	-5	4	-45	-51	6

Measurement of Emissions from the System Box

- The enclosure box has the fabricated FSS on its top cover and the system board with 9 square patches on its floor to emulate an active digital system.

- The in-lab test set-up ensures maintaining the 40 cm distance from center of the box to measure the emissions from the boxed system with and without FSS.
- The surface of the cylinder is marked to specify field measurement points at 10 cm intervals in height (z direction) and 10 degrees in azimuth (φ direction).

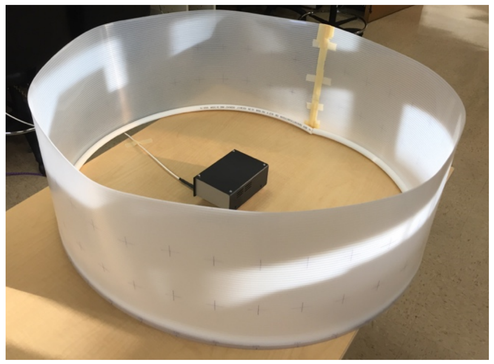

- A patch antenna is designed to operate at 8 GHz to be used as a probe and measured emissions are reported in the table to compare with simulation. 4 spacers at corners keep 7.5 cm distance from the cylinder surface.

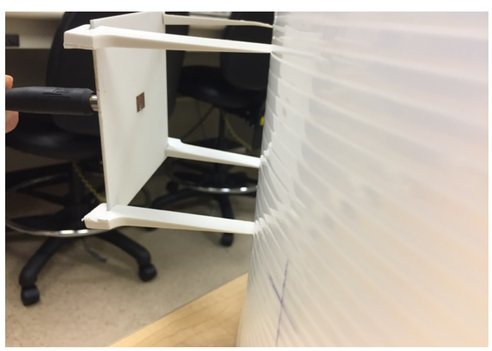

Radiation Pattern Measurement

- Simulation plots are far-field patterns at $\theta = 90^o$ cut-plane with sweeping φ angle. Measurements are done at the distance of 47.5 cm from the center of the box at z = 10 cm (almost indicating $\theta = 80^o$), and sweeping φ at 10° intervals
- Radiation patterns below show FSS performance for the worst case when Feed 2 is active. Left plot is simulation and right plot is measurement.

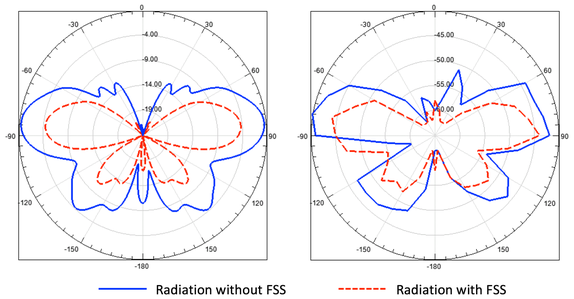

- Following radiation patterns show FSS performance when Feed 5 is active. Left plot is simulation and right plot is measurement.

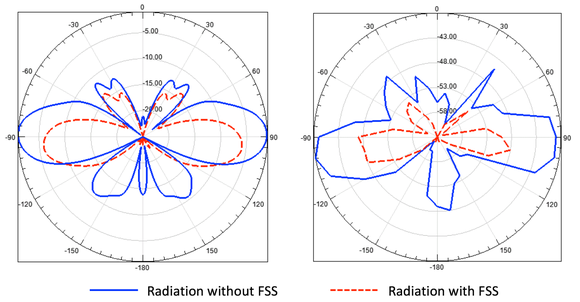

Conclusions

- The FSS surface impedance changes with the angle of incidence of the plane wave. Therefore, it is concluded that the relative location of active components on the board also impacts the radiated emission level.
- It is observed that the strongest emissions happen when the active patch is at the center of the board and closest to the side of the box with ventilation slots.
- Simulations show 6 dB emission reduction for the worst cases. Measurements of radiation patterns closely follow the simulated emission patterns and demonstrate better than 5 dB reduction for the worst case emissions.
- This application of FSS is a low cost solution that provides a system level EMC failure remedy at the final stages of product development.

Wireless Power Transfer in Biological Materials

Daniel Webber, Undergraduate Student; Nivedita Parthasarathy, PhD Student; Dr. Ramesh Abhari, Advisor
Department of Electrical Engineering
Santa Clara University
School of Engineering

Motivation:

- Implanted wireless medical devices are being heavily researched, because of their ability to provide targeted medical treatment and drug delivery without utilizing a large battery to supply power.
- To efficiently power and communicate with implanted devices, the biological mediums need to be correctly characterized at the desired frequencies.

Objectives:

- Design a transmitter and receiver coil system in a 3D EM CAD solver to extract the system's coupling coefficient as the spacing varies.
- Embed the receiver coil in biological-like materials and simulate it to understand how it affects the coupling's coefficient as the spacing varies.
- Design and optimize a passive matching network in simulations to maximize the power transfer efficiency to and from the coils.

Design of Transmitter and Receiver Coil:

- The layout parameters are kept the same in all simulations, only coil spacing is varied

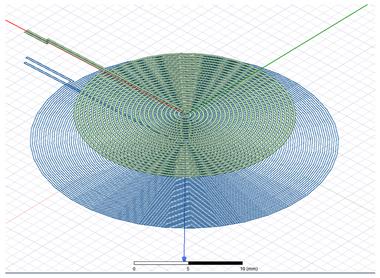

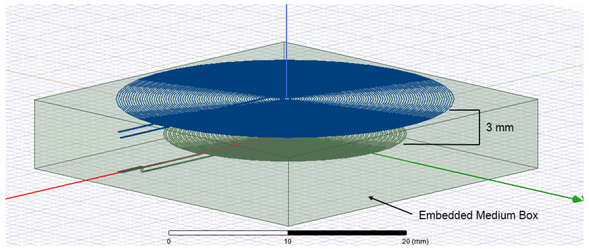

Coil Layout Properties			
Coil	Number of Turns (N)	Trace Width (mm)	Spacing Between Trace (mm)
TX	35	0.2	0.2
RX	25	0.2	0.2

Mutual Inductance vs. Spacing in Different Mediums

- **Magnetostatics Simulation in ANSYS Maxwell 3D**

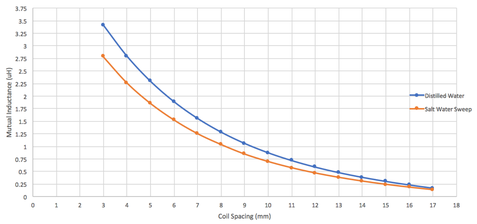

Relevant Material Properties		
Medium	Relative Permeability	Bulk Conductivity (S/m)
Distilled Water	0.99	0.0002
Salt Water	0.99	4.0000

- RX coil embedded in said material.
- Air and Distilled Water simulate to the same values

Tuned Matching Circuit with Coil Model in ADS

- ADS System Simulations

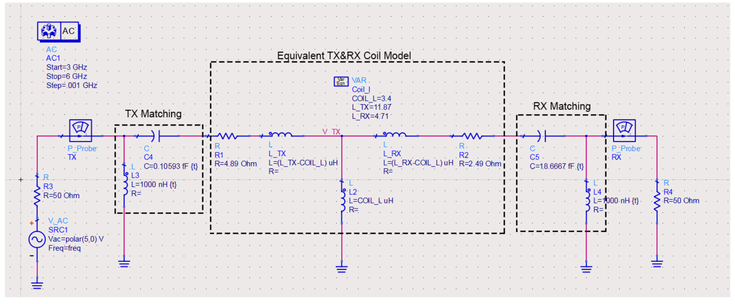

S-Parameters

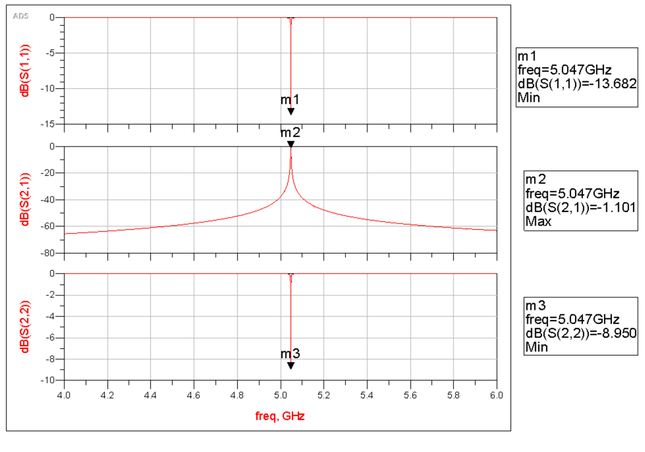

Average Input Power and Output Power

- The power is calculated from ADS using P_{AVG}= real(½*V*conj(I))

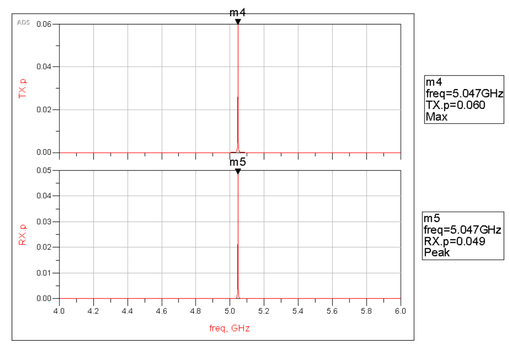

Note: Inductance values used in ADS related simulations the results are for the case that the two coils are spaced 3 mm apart with the RX Coil embedded in Distilled Water.

Key findings of this project:

- A simulation framework can be used to learn how different mediums affect the system's performance in the near field.
- A matching network could be optimized with theoretical component values.
- A power transfer efficiency of 75% was achieved at 3mm spacing when the Rx coil is embedded in salt water which is 5% lower compared to that of air medium.

Next steps:

- Explore more relevant materials and their effects on power transfer.
- Use this framework to design a receiver coil for the size needed in an electronic implant.
- Improve lumped element coil models.
- Compare efficiency results with other matching network topologies being researched.
- Fabrication of coils and matching network to verify simulation results.

References:

R. L. de Abreu, L. B. Zoccal, T. C. Pimenta and D. H. Spadoti, "Self-tuning of impedance matching for wireless power transfer devices," 2016 1st *International Symposium on Instrumentation Systems, Circuits and Transducers* (INSCIT)

NanoGrid

A Path to Energy Efficiency and Renewable Energy

Taylor Mau, Randy Louie, Francis Estacio, Maryam Khanbaghi, Nico Garcia and Brian Meier

Background

With prices of consumer photovoltaic (PV) generation systems decreasing, the number of small-scale electricity generating households is growing steadily. Many current household generation systems are not able to take full advantage of the electricity they generate. To circumvent this set of problems, several energy storage systems have emerged within the market that give households the ability to store self-generated energy for later use. With the increasingly common partnership of PV generation and battery energy storage systems, a household with both can be treated as its own microgrid system, capable of self-generation, storage, and only using a connection to the existing utility network when absolutely necessary.

Objective

In this work, we choose residential homes and forgo the connection to the grid. We will call these single home microgrids, nanogrids (nGrids). The major component of nGrids energy management systems is advanced control strategies. [2,3,5,7].

The objective of this work is to propose a control strategy for an nGrid energy management system where the average household can operate autonomously from the main grid with current technologies available in the market. This work is divided in four parts:

1. System Description
2. System Prototype
3. Control Strategy Simulation
4. Results and Evaluation

System Description

A. nGrid Architecture

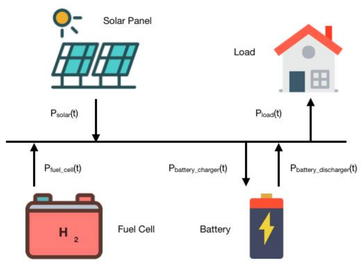

Fig. 1. nGrid architecture with battery, fuel cell, solar, and load.

B. System Model

$$P_{load}(t) = P_{solar}(t) + P_{FC}(t) + P_{batt.}(t). \quad (1)$$

$$P_{solar}(t) = \begin{cases} P_{solar}^{day}(t) = S(r(t)) = \begin{cases} r(t)=1 & \text{(sunny)} \\ r(t)=2 & \text{(cloudy)} \\ r(t)=3 & \text{(overcast)} \end{cases} \\ P_{solar}^{night}(t) = 0 \end{cases} \quad (2)$$

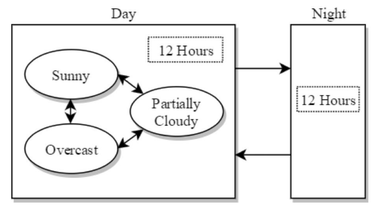

Fig. 2. Weather diagram representing cloud coverage during daytime.

$$\frac{dE_b(t)}{dt} = \alpha E_b(t) + (1 - a_i)P_{solar}(t) - b_i P_{batt}^{dis.}(t) + (1 - c_i)P_{FC}(t)$$

$$\frac{dE_l(t)}{dt} = \beta E_l(t) + a_i P_{solar}(t) + b_i P_{batt}^{dis.}(t) + c_i P_{FC}(t)$$

C. Household Load Data and Simulated Cloud Coverage

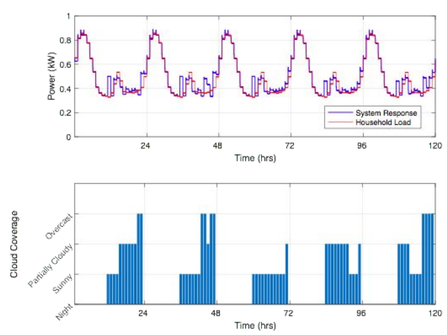

Fig. 3. System response with simulated response (top) and simulated cloud coverage (bottom).

System Prototype

nGrid

- Represents the electrical components of a home
- Comprised of a solar panel, fuel cell, and battery
- Uses integrated sensors to measure and display voltage, current, and power generated or consumed by each component
- Compact and user friendly

Fig. 4. Front of nGrid controller

Autonomous Vehicle

- Acts as a load to the nGrid via wireless charging
- Main Components:
  - Arduino Mega
  - Accelerometer
  - Laser Range Finder
  - Ultrasonic Range Detector
  - GPS
- Able to read sensor data and detect obstacles in path
- Second chassis built to optimize space and efficiency

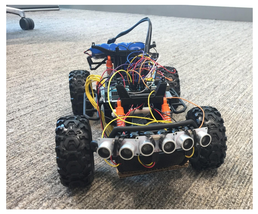

Fig. 5. Autonomous vehicle design with off-the-shelf chassis

Control Strategy Simulation

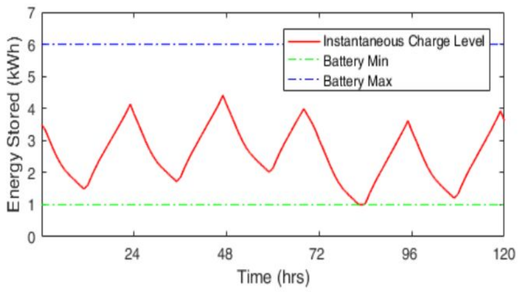

Fig. 8. Simulated charge and discharge of the Battery

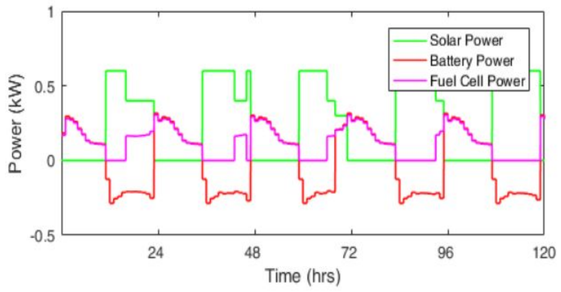

Fig. 7. Solar, battery, and fuel cell contributions (long overcast and night period).

Results and Evaluations

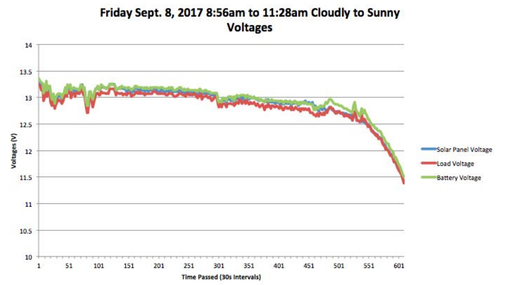

Fig. 6. Voltages throughout the day

Conclusion and Future Works

This work discusses the energy management problem of an islanded microgrid - nGrid. The nGrid utilizes solar and fuel cell generation combined with a battery energy storage system to satisfy the load demand of a small household. The solar generation is modeled as a continuous Markov process. We were able to design a prototype that emulates an nGrid. It is able to divert power from the battery to satisfy the load. By using solar, we were able to charge the battery while powering the loads showing the possibility of creating an off-the-grid house using this system.

Future work will include more accurate battery and fuel cell models in order to better predict their generation output. Furthermore, for the prototype, we will plan to take data throughout an entire day (24 hours) and improve on design.

Acknowledgments

- Santa Clara University Latimer Lab
- Michel Hernandez Cortes, Mike Lau.
- Dr. Leo Casey
- Nathan Tucker
- Santa Clara University School of Engineering

References

1.Residential Solar Statistics – California Solar Initiative (CSI), www.gosolarcalifornia.ca.gov

2.L. Belloni, L. Piroddi, and M. Prandini, “A Stochastic Optimal Control Solution to the Energy Management of a Microgrid with Storage and Renewables”, 2016 American Control Conference, Boston , MA

3.G, Bruni, S. Cordiner, M. Galeotti, V. Mulone, M. Nobile, and V. Rocco, "Control Strategy Influence on the Efficiency of a Hybrid Photovoltaic-Battery-Fuel Cell System Distributed Generation System for Domestic Applications." Energy Procedia 45 (2014)

4."Off Grid Power." Udomi | competence in fuel cell systems | off-grid power wherever you need it. http://www.udomi.de/produkte-kategorie.php?lang=en&kategorie=1.

5.Y. Levron, J. M. Guerrero, and Y. Beck, “Optimal Power Flow in Microgrids with Energy Storage,” *IEEE Trans. on Power Sys.*, vol. 28, no. 3, Aug. 2013.

6.M. Subashini, and M. Ramaswamy, "A novel design of charge controller for a standalone solar photovoltaic system." *2016 3rd International Conference on Electrical Energy Systems*, 2016.

7.Tucker, Nathan. “Jump Linear Quadratic Control for Energy Management of an Isolated Microgrid,” thesis, Santa Clara University, Santa Clara, 2017.

www.scu.edu

Santa Clara University
School of Engineering

A Low Power Energy Harvesting Circuit for IoT Applications

PhD Student: Sanad Kawar. Advisors: Shoba Krishnan and Khaldoon Abugharbieh
Department of Electrical Engineering

Santa Clara University
School of Engineering

Introduction

- The Internet of Things (IoT) has fueled more demand for low power applications.
- IoT requires a network of wireless smart nodes that contain sensors, signal processors and wireless transceivers [1].
- The drive for smaller IoT nodes means that the form factor of batteries used to power them will have limited capacity and require periodic replacement [2].
- As the number of nodes scales up to the full vision of IoT, maintenance would become impractical and costly.
- Energy harvesting (EH) is critical to allow IoT devices - such as miniature-scale sensor nodes and implantable medical devices [3] - to be self-sustaining or **energy-autonomous**, by continuously harvesting energy from ambient sources to recharge on-board batteries and/or supply a battery-less system
- Energy can be harvested from DC sources such as solar, indoor light and thermal [2][3], in addition to AC sources such as vibration. RF radiation can also be used [4].

Conceptual System Block Diagram

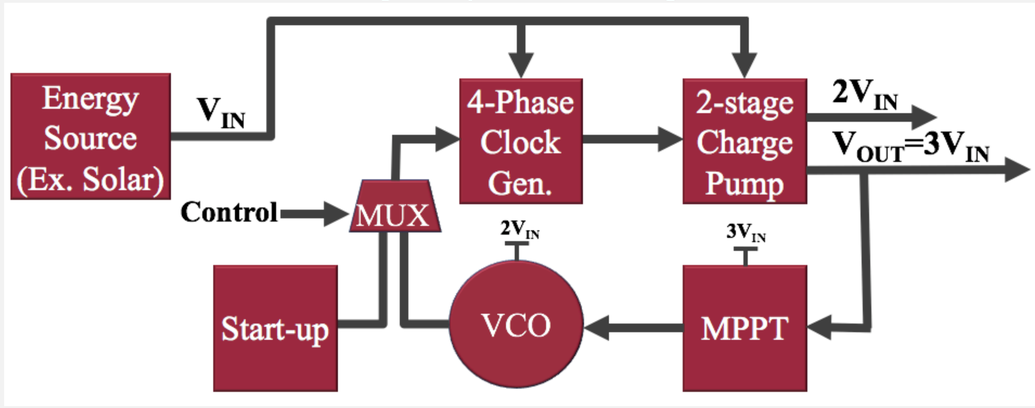

Challenges

- Available Energy varies and is environment-dependent ➡ Large range of input power makes it difficult for harvesters to operate efficiently
- Sources produce low power and low voltage ➡ Not directly usable to charge batteries (~4Volt) [5] nor drive circuits (>1Volt) [2].
  ➡ **Power Management Unit** to boost and regulate
- Harvested voltage not sufficient to turn on CMOS devices ➡ Start-up blocks needed to start operation
- Fully-Integrated Design desired ➡ Can limit efficiency [1]
- Maximum Power Point Tracking (MPPT) is necessary

Voltage Doubler Charge Pump Model

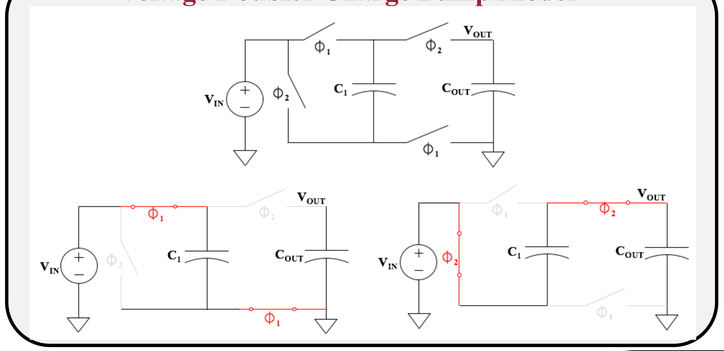

Applications

- Self-sustaining IoT devices such as wireless sensor nodes used for example for:
  - Infrastructure monitoring [3]
  - Environmental monitoring [6]

  to enable IoT applications such as smart grids, smart water networks and smart transportation
- Implantable medical systems [3]

Objectives

The purpose of this project is to design a low power, fully-integrated Energy Harvesting integrated circuit and explore innovative architectures, circuit topologies and methods for delivering power to the loads.

Design the system to:

- ➢ Operate efficiently within stringent power constraints
- ➢ Extract maximum power from environment-dependent sources
- ➢ Boost and deliver a regulated voltage to circuits and/or for battery charging

Two-Stage Charge Charge Pump [5]

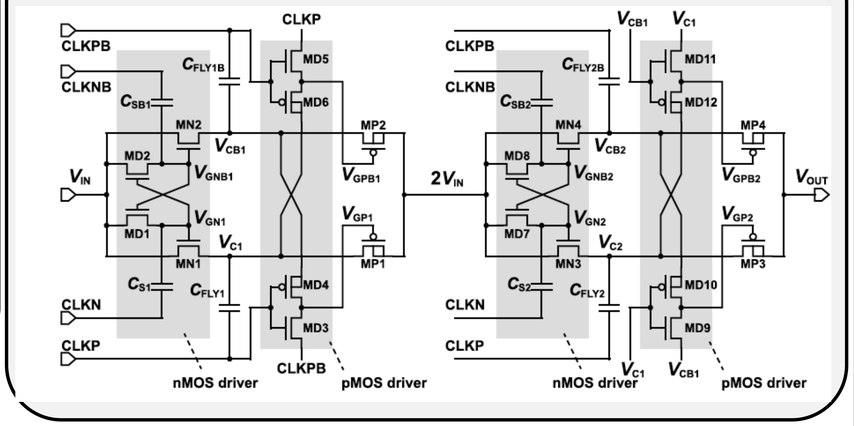

Future Plans

- Continue investigating methods to operate the charge pumps discontinuously and power-gate IoT loads to reduce power consumption
- Design the MPPT block
- Improve clock drivers

Preliminary Simulations Results

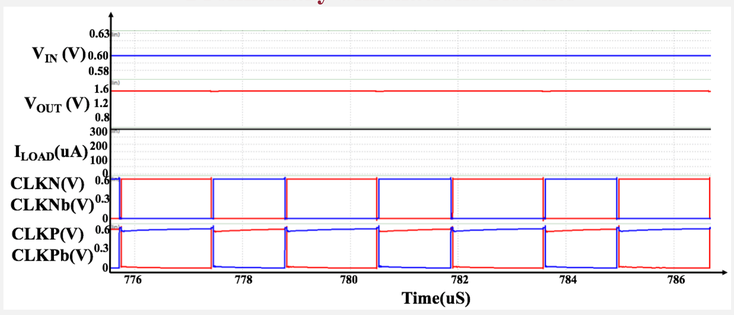

Transient Simulation Plot

Vin=0.6V. Vout=1.58V Iout=300uA Pout=0.474mW

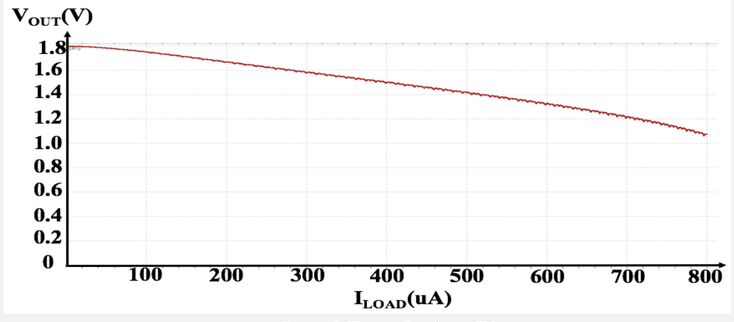

Load Regulation Plot

VCE > 70% for up to 660uA load current

References

[1] X. Liu et al., "A Highly Efficient Reconfigurable Charge Pump Energy Harvester With Wide Harvesting Range and Two-Dimensional MPPT for Internet of Things", *IEEE J. Solid-State Circuits*, vol. 51, no. 5, pp. 1302-1312, May. 2016.

[2]G. Chowdary and S. Chatterjee, "A 300-nW sensitive, 50-nA DC-DC converter for energy harvesting applications," *IEEE Trans. Circuits Syst. I*, Reg. Papers, vol. 62, no. 11, pp. 2674–2684, Nov. 2015.

[3] X. Wu et al., "A 20-pW Discontinuous Switched-Capacitor Energy Harvester for Smart Sensor Applications.", *IEEE J. Solid-State Circuits*, vol.52, no.4, pp. 972-984, Apr. 2017.

[4] S. Carreon-Bautista et al., "An Autonomous Energy Harvesting Power Management Unit With Digital Regulation for IoT Applications" in I*EEE J. Solid-State Circuits*, vol. 51, no. 6, DOI [10.1109/JSSC.2016.2545709], June. 2016.

[5] T. Ozaki et al., "Fully-Integrated High-Conversion-Ratio Dual-Output Voltage Boost Converter With MPPT for Low-Voltage Energy Harvesting", *IEEE J. Solid-State Circuits*, vol. 51, no. 10, pp. 2398 - 2407, Oct., 2016.

[6] C. M. Nguyen et al., "Wireless Sensor Nodes for Environmental Monitoring in Internet of Things", in IEEE intl. Microwave Symp., Phoenix, AZ., 2015, pp 1-4.

A C-band wide locking range injection locked oscillator based phase shifter

Sudipta Saha, PhD Student; Dr. Shoba Krishnan, Advisor, Dr. Allen A Sweet, Advisor
Department of Electrical Engineering
Santa Clara University
School of Engineering

Motivation:

Challenges of WiFi enabled devices

- Limited range, high data rate and low phase noise
- Adjacent RF interference is strong

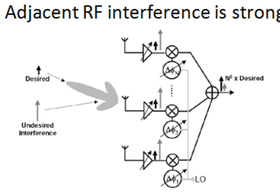

The Advantages of Phased Array based Beamforming

- Focus RF energy on the target of choice
- Suppress RF interference by adjusting deep side lobes

Objective

Phase shifters are integral components in an antenna array

- Injection locked oscillator phase shifters (ILPS) are analog
- It is important to design an ILPS with the widest possible lock range
- Lock Range can be increased by decreasing Q-factor
  > Degrades phase noise, compromises start-up and has higher power consumption
- Lock Range can be increased by increasing I_{inj} or P_{inj}
  > Greater power consumption due to increased injection amplifier gain

Operation of injection locked oscillator based phase shifter (ILPS)

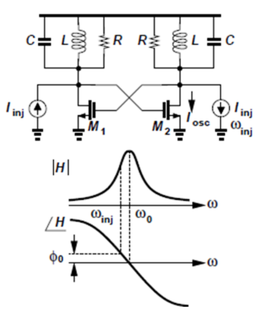

Locking Range

$$\omega_0 - \omega_{inj} = \frac{\omega_0}{2Q} \cdot \frac{I_{inj}}{I_{osc}} \cdot \frac{1}{\sqrt{1 - \frac{I_{inj}^2}{I_{osc}^2}}}.$$

Phase shift in an injection-locked oscillator

$$\sin\theta \approx \frac{2Q}{\omega_0} \cdot \frac{I_{osc}}{I_{inj}}(\omega_0 - \omega_{inj})$$

Wide lock range ILPS

- **A new approach of implementing phase shifter based on injection locking is proposed**
- Target locking range of 3GHz to 7GHz includes the Wi-Fi band
- Wide locking range is achieved by decreasing natural oscillation output power (P_{osc})
  - ➢ This method does not decrease bias current to reduce P_{osc} as this effects startup
  - ➢ Instead it uses a new design technique

New Circuit Topology

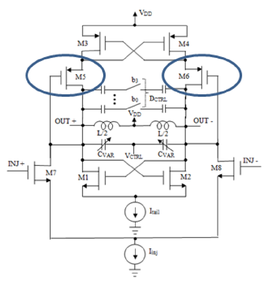

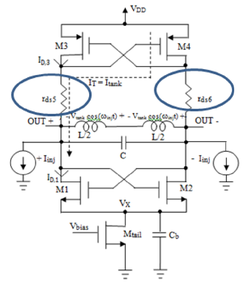

Schematic of proposed injection locked based phase shifter (ILPS)

Model of ILPS with current source AC shorted

$$\frac{I_{D,M1}}{I_{D,avg,M1}} = \left(\frac{V_{bias}}{V_Q - V_t} + \frac{V_{tank}}{V_Q - V_t}\cos(\omega_{inj}t) - \frac{V_t}{V_Q - V_t}\right)^2$$

- At RF frequencies, the drain current is no longer set by tail current source, but instead set by the voltage swing across the LC tank

Proposed injection locked oscillator based phase shifter simulation results for enhanced lock range

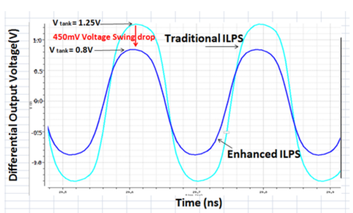

Voltage headroom reduction

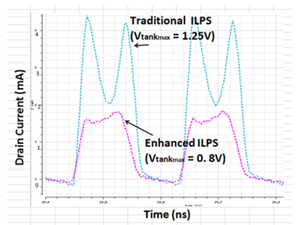

Oscillator current reduction

- Injection-locked based phase shifter achieves a reduction of +/- 450mV in differential oscillator output swing, with a resulting increase in locking range

Input injection power sensitivity

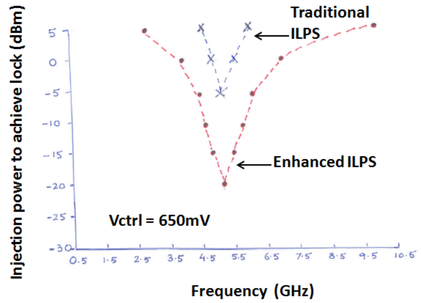

- Injection locked based phase shifter (ILPS) has a locking range of 3GHz at 5.3GHz center frequency with a 0dBm input power
- The traditional ILPS had a locking range of only 120 MHz, showing an improvement of 2.88GHz

Phase shift Vs tuning voltage for proposed injection locked oscillator based phase shifter

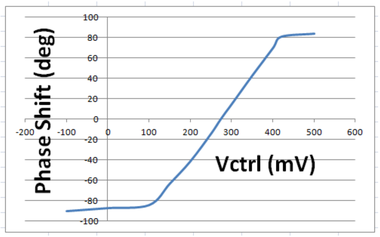

- The maximum phase shift is +/- 90 degree with 0 dBm input power.
- The phase shift is continuously tunable

Conclusion

- A new approach to implementing an analog phase shifter, based on injection locking (ILPS), is proposed
- The ILPS is implemented on an 90nm RF CMOS process
- The phase shifter can be used in the local oscillator (LO) path of a phase array system
- Improved locking range is the principal strength of this design approach
- Tradeoff is the degradation of phase noise performance

References:
(1) B. Razavi, "A study of injection locking and pulling in oscillators," IEEE JSSC, vol. 39, no. 9, pp. 1415-1424, Sept. 2004
(2) A. Natarajan, et., "A 77GHz phase array transceiver with on-chip antennas in silicon," IEEE JSSC,vol. 41, no. 12, pp. 2807-2819, Dec. 2006
(3) J. Roderick, et., "Silicon-based ultra-wideband beam-forming," IEEE JSSC, vol. 41, no. 8, pp. 1726-1739, Aug. 2006

Adaptive Search Pattern for Fast Motion Estimation in Video

Pavel Arnaudov — Santa Clara University, ELEN

Tokunbo Ogunfunmi — Santa Clara University, ELEN

ABSTRACT

Motion estimation consumes the major portion of time and power in both video compression standards – HEVC and H.264. This paper presents a Fast Motion Estimation algorithm, which learns the best search pattern per video scene. That maximizes the quality of the Motion Vectors, while preserving the speed of Fast Motion Estimation without any memory usage. The algorithm is not HEVC or H.264 specific and thus can be used by either one.

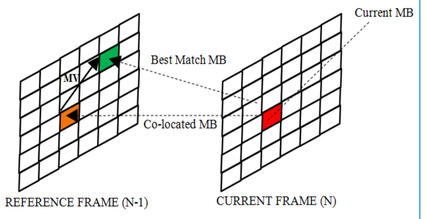

Motion Estimation

$$SAD(m,n,p,q) = \sum_{i=1}^{N}\sum_{j=1}^{M} | f_k(m+i,n+j) - f_{k-1}(p+i,q+j) |$$

OVERVIEW

This paper compares the performance of the original HMDS algorithm [3] with an algorithm similar to HMDS, but with enhanced search pattern (enhanced with manually preselected fixed set of additional search patterns), plus another HMDS-like algorithm, but with only one search point [0,0], the proposed Adaptive Search Pattern and Full Search .

More dynamic videos benefit from search patterns that have wider range, while less dynamic videos would yield better results if the reference frame points checked are closer to the co-located position in the current frame. Since the dynamics can change multiple times between scenes within the same video, we propose the search pattern to follow these changes and adapt to them.

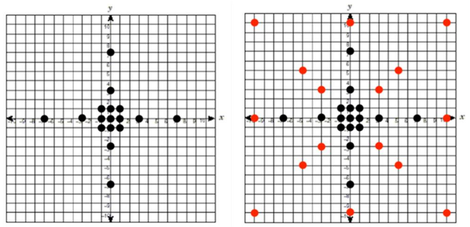

Step 1 Search Pattern: HMDS (a); EHMDS (b)

ALGORITHM

The Adaptive Search Pattern is being updated for every scene change (I-frame). The search for each new point of the Adaptive Search Pattern is being done while using all the previously found and accumulated points and then scanned through all the possible new positions for the currently searched point, without overlapping with any of the points already present in the pattern accumulated so far. The points scanned are all in the First Quadrant, with each point being symmetrically applied in the other three quadrants across the X and Y axes.

A) The active area where the Adaptive Pattern Search is being performed is flop based and its size depends on the maximum Range of the Search Pattern and the Macro Block size :

Number of flops = (2*Range+1 + MB size – 1) ^2 pixels * 8 flops/pixel = (2*Range + MB size) ^2 * 8 flops

Example: Range = 32, MB size = 16:

Number of flops = (2*32 + 16) ^2 * 8 = 51200 flops.

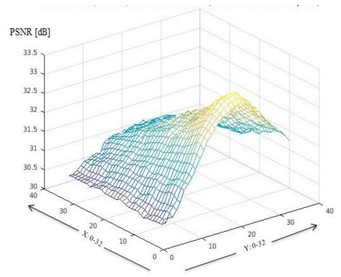

B) Time available for learning a pattern in a 80x80 pixels area:

HD Frame: 1920x1080, MB: 16x16 => ~8000 MB/frame.

Frame rate 120 fps: Budget = 1s/120 fps = 8.33ms/frame.

If scanning the active area with a Step = 8 (X & Y): (80/8)*(80/8) = 100 Fast Motion Estimations for the whole frame are needed.

(Step of 8 is justifiable by Search Passes 2 and 3, which follow)

One frame requires ~8000 MB evaluations, each of which needs as many SAD calculations as the number of points we have in the search pattern. One SAD takes 1ns (i.e. 1 cycle at 1GHz).

If the Search Pattern has 10 points in total, the Learning time is: 10 points *100 Fast ME/point *8000 MB / Fast ME * 10 ns/MB = ~80ms = ~10 inter-frame intervals. This means we can update 1 search point of the pattern for every frame for 10 frames (starting with a default fixed pattern). Ten frames after a scene change, we can choose to continue the process to improve quality (replacing the worst performing Search Pattern point) or we can stop adaptation till next new scene to save power (user dependent).

EXPERIMENTAL VIDEOS

OPTIMAL SEARCH PATTERNS FOUND

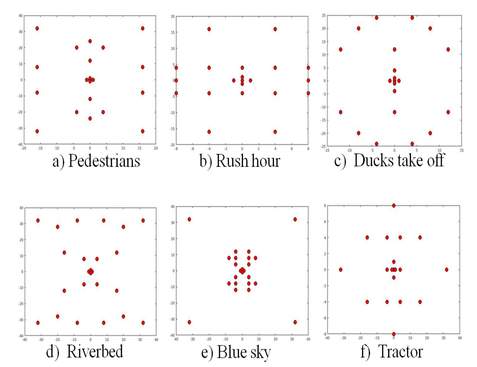

PATTERN LEARNING PROCESS

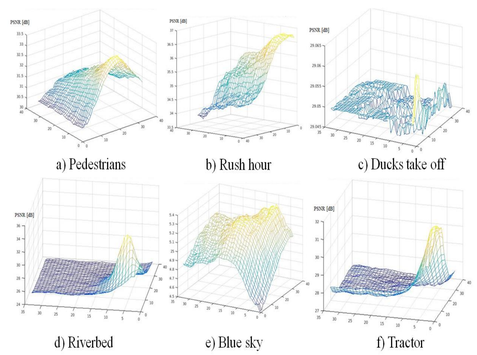

RESULTS

This is how the proposed algorithm compares to two other efficient Fast Motion Estimation approaches (HMDS, EHMDS):

PSNR Results [dB]

Sequence	$HMDS_0$	HMDS	EHMDS	Adaptive	Full
Pedestrians	22.2821	28.6883	33.6834	34.4286	37.2151
Rush Hour	26.9213	35.1311	35.8353	36.7729	37.1540
Ducks Take Off	27.7013	28.8155	28.8147	28.9558	29.0785
River Bed	19.6829	23.5266	25.8291	26.4039	30.2728
Blue Sky	19.4059	24.7533	26.1517	26.6891	27.5107
Tractor	22.2821	28.6883	33.6834	33.7160	33.9115

OPTIMAL NUMBER OF SEARCH PATTERN POINTS

The contribution of each new point added to the Adaptive Search Pattern is analyzed for the video "Pedestrians" (as a dynamic video this is the worst case for Fast ME).

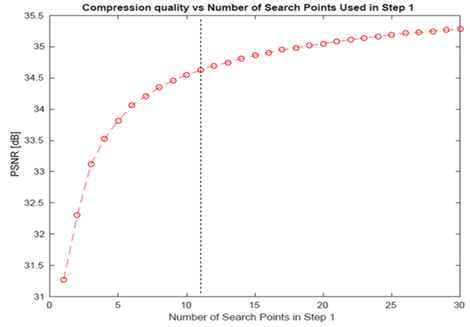

Saturation is at 10-11 points. EHMDS has 10-11 points too.

Deploying Neural Networks in Fast ME

A NN is used to provide a suggestion for the best Search Pattern.

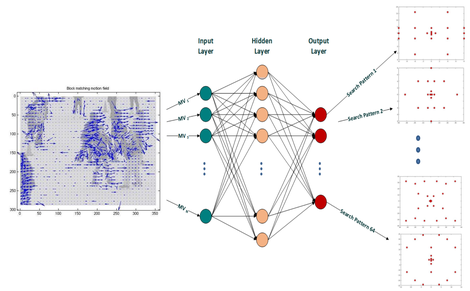

CONCLUSIONS

The results show that using an Adaptive Search Pattern helps cover about 10%-70% of the PSNR gap between existing fixed search pattern algorithms and Full Search.

This is being achieved without adding extra memory.

Future Work

Explore asymmetric Search Patterns to improve quality while reducing the computation power, time and hardware complexity.

REFERENCES

[1] T. Wiegand, G. J. Sullivan, G. Bjøntegaard, and A. Luthra, "Overview of the H.264/AVC video coding standard," IEEE Trans. Circuits Syst. Video Technol., vol. 13, no. 7, pp. 560–576, Jul. 2003..

[2] G. J. Sullivan, J.-R. Ohm, W.-J. Han, and T. Wiegand, "Overview of the High Efficiency Video Coding (HEVC) standard," IEEE Trans. Circuits Syst. Video Technol., vol. 22, no. 12, pp. 1648–1667, Dec. 2012.

[3] O. Ndili and T. Ogunfunmi, "Hardware-oriented modified diamond search for motion estimation in H.264/AVC," in Proc. IEEE ICIP, Sep. 2010, pp. 749–752.

[4] O. Ndili and T. Ogunfunmi, Algorithm and Architecture Co-Design of Hardware-Oreinted Modified Diamond Search for Fast Motion Estimation in H.264/AVC, IEEE Transactions on Circuits and Systems for Video Technology, Vol. 21, No. 9, pp. 1214-1227, Sept. 2011.

[5] R. Li, B. Zeng, and M. L. Liou, "A new three-step search algorithm for block motion estimation," IEEE Trans. Circuits Syst. Video Technol., vol. 4, no. 4, pp. 438 – 482, Aug. 1994.

[6] L.-M. Po, and W.-C Ma, "A novel four-step search algorithm for fast block motion estimation," IEEE Trans. Circuits Syst. Video Technol., vol. 6, no. 3, pp. 313 – 317, Jun. 1996.

[7] J. Y. Tham, S. Ranganath, M. Ranganath, and A. A. Kassim, "A novel unrestricted center-biased diamond search algorithm for block motion estimation," IEEE Trans. Circuits Syst. Video Technol., vol. 8, no. 4, pp. 369 – 377, Aug. 1998.

CONTACT

Pavel Arnaudov (PDArnaudov@scu.com)

Tokunbo Ogunfunmi (togunfunmi@scu.edu)

An Efficient Reconfigurable Hardware Accelerator for Convolutional Neural Networks

Anaam Ansari[1], Prof. Tokunbo Ogunfunmi[1], Kiran Gunnam[1]
1 Santa Clara University, 500 El Camino Real, Santa Clara, 95053

1. ABSTRACT

Convolutional Neural Networks (CNN) have proven to be very effective in image and speech recognition. The increasing usage of such applications in mobile devices and data centers have led the researchers to explore application specific hardware accelerators for CNN. However, most of these approaches are limited to a specific network such as AlexNet. We propose a reconfigurable technique that can be extended to be a network-agnostic architecture that supports various networks. The technique described in this paper aims at developing a reconfigurable accelerator that uses basic processing elements (PE) as building blocks of its computational engine. In our design, we control the configuration of each layer using a switching control logic and a Benes network. In addition to potentially supporting all the various CNN architectures, our computation engine design has a 94% improvement in the convolutional layer execution time for AlexNet compared to the state-of-the art architecture that only supports AlexNet.

2. CONVOLUTIONAL NEURAL NETWORK

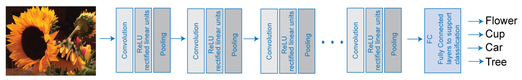

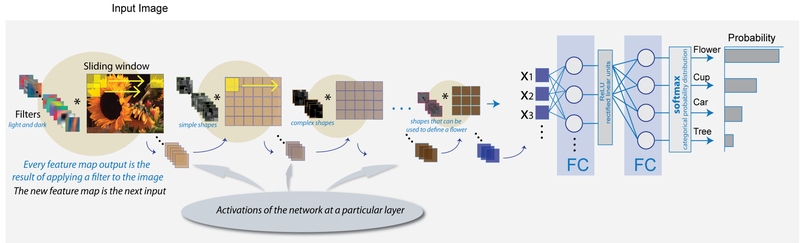

https://www.mathworks.com/help/nnet/ug/introduction-to-convolutional-neural-networks.html

CNN Hardware Accelerator

- There are some key elements to a CNN accelerator design.
- It contains a computational logic consisting of processing elements.
- There is a need for some local memory to move data around.
- A control logic is required to facilitate communication and schedule computation cycles.
- External memory to hold the results.

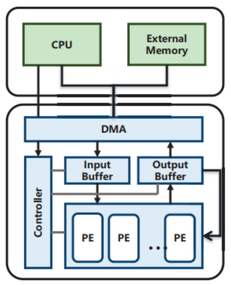

Guo, Kaiyuan et al. "Angel-Eye: A Complete Design Flow for Mapping CNN onto Customized Hardware." 2016 IEEE Computer Society Annual Symposium on VLSI (ISVLSI) (2016): 24-29.

3. NEED FOR RE-CONFIGURABILTY

- Variety of networks are available
- For a given network, the layers can be radically varying dimensions
- Optimum use of **resources**
- Extracting maximum value out of on-chip data by reusing it
- Many networks available: AlexNet, ResidualNet and Google Net
- Exploit the similarities available in different networks to minimize design cost for each network

- **Eyeriss Design**: Chen, Yu-Hsin, et al. "Eyeriss: An energy-efficient reconfigurable accelerator for deep convolutional neural networks." *IEEE Journal of Solid-State Circuits*52.1 (2017): 127-138.
- **UCLA Design**: Zhang, Chen, et al. "Optimizing fpga-based accelerator design for deep convolutional neural networks." *Proceedings of the 2015 ACM/SIGDA International Symposium on Field-Programmable Gate Arrays*. ACM, 2015.
- **Stony Brook Design** :Shen, Yongming, Michael Ferdman, and Peter Milder. "Maximizing CNN accelerator efficiency through resource partitioning." *arXiv preprint arXiv:1607.00064* (2016)

4. STATE OF THE ART

- Data Reuse techniques
  - Loop Unrolling and Tiling
  - 1-D Row Stationary techniques and 2-D Row Stationary techniques to minimize the movement of filter coefficients
- RLC to reduce parameter size
- Uniform Accelerator Design
- Multiple Convolutional Layer Processors of varying dimensions

5. PROPOSED DESIGN

- Bank of Processing Elements.
- They are held together and controlled using a switching layer. This switching layer will facilitate the interconnections in the PE grid.
- The input to the computational engine will be managed by a Benes network.
- A control logic for scheduling and controlling communication.
- To implement our design we will use the optimized unroll factors.

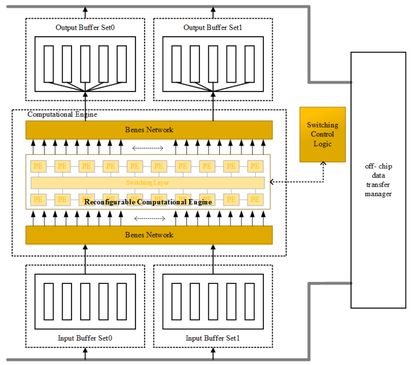

6. BENES NETWORK

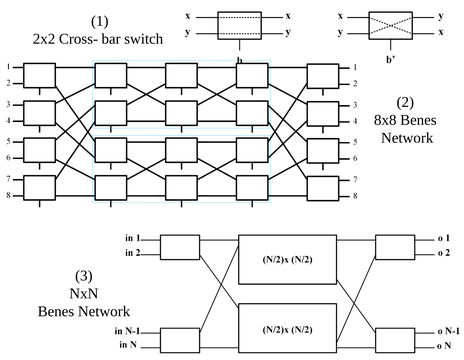

7. PROCESSING ELEMENTS

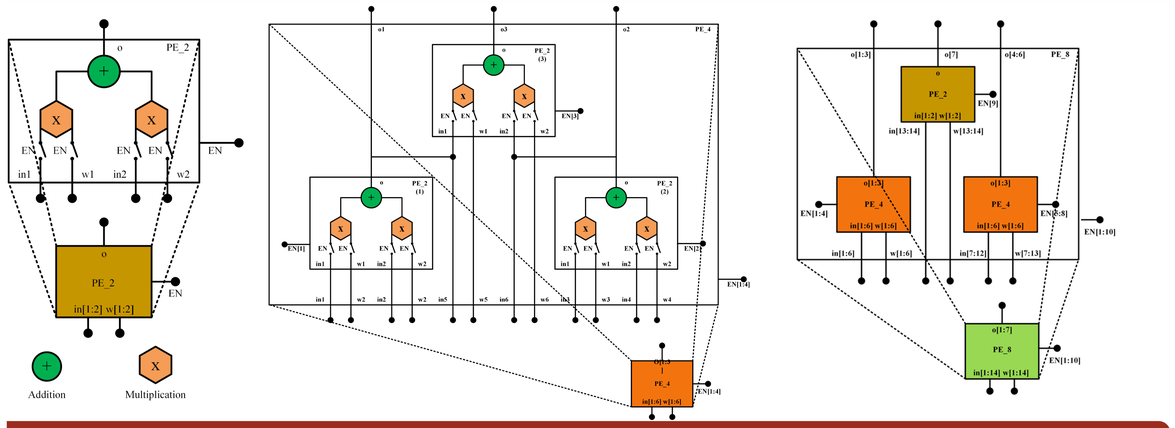

8. LAYERS

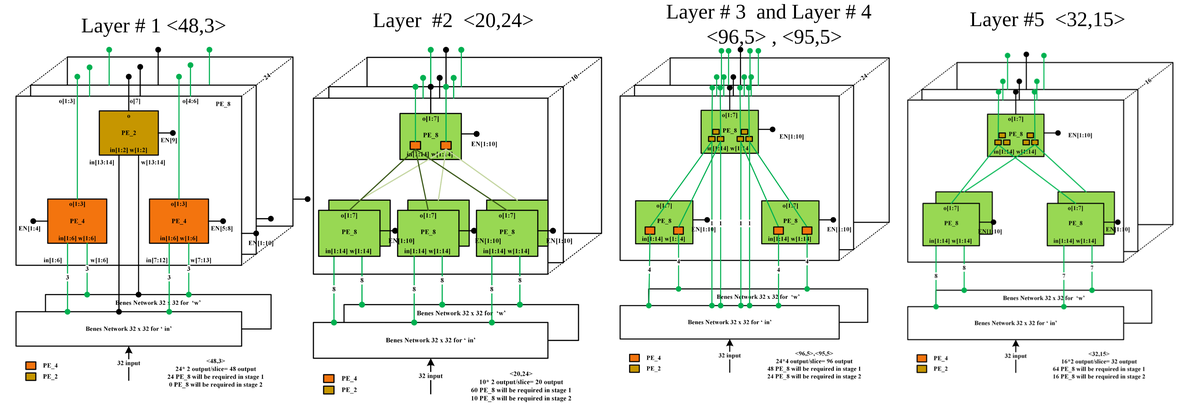

9. RESULTS

The Fmax of our design is 109.35 MHz where Fmax is the maximum frequency our design can have.

	Optimal unroll factors <Tm, Tn>	PE Engine (only) Execution Cycles	Benes network (only) Execution Cycles
Layer 1	<48,3>	21680	43350
Layer 2	<20,24>	2722	5420
Layer 3	<96,5>	13006	26010
Layer 4	<95,5>	13006	21676
Layer 5	<32,15>	4066	105126

10.CONCLUSIONS AND FUTURE WORK

- Total number of clock cycles are 159606. The design is 84% better than the one which uses uniform unroll factors <64,7> which is 1008246 clock cycles.
- Exploiting the similarity in layers was a key idea to design modular reusable hardware
- Handling of off chip memory and on-chip data is vital to the success of the an efficient architecture.
- A combination of multiple architecture techniques could be used to complement each other.
- Although, we have made accommodation in our design to make it configurable to different layer dimensions, we bear the cost of unused real estate in the computation.
- Optimization of the computations engine can help improve the overall efficiency even more.
- The input and out Benes networks provide an additional cost into completing this architecture. This design does not focus on using the state of the art network and routing protocols available.
- Extending this accommodation to other networks in order to tend towards a network agnostic architecture solution.

Using Machine Learning to Help in Medical Diagnosis

Juliana Shihadeh, Undergraduate, Computer Engineering
Professor Tokunbo Ogunfunmi, Department of Electrical Engineering
Santa Clara University, 500 El Camino Real, Santa Clara, 95053

Abstract

Machine Learning is an increasingly growing field that continues to affect our lives. In recent developments, machine learning has been becoming increasingly applied in Medical Diagnosis to speed up the process. Researchers have been drawing conclusions of solutions that speed up the process of analyzing MRI scans and provide more accurate readings of images diagnosing cancer in patient. We would like to expand on solutions for medical diagnosis that are faster, more effective, and provide higher rates of accuracy. Using the AlexNet Convolutional Neural Network Architecture, we would like to develop a tool based on it to produce results that can contribute in the field of diagnosing medical problems, such as cancer and skin health issues. Furthermore, we would like to be able to make the tool usable in remote areas where doctors are in short supply so the tool is accessible and usable around the world. Preliminary results are shown here.

Introduction

Artificial Intelligence has led to the innovation of technology smart enough to act and make decisions like a human. Under Artificial Intelligence is a subcategory identified as Machine Learning, and within Machine Learning is a subcategory identified as Deep Learning.

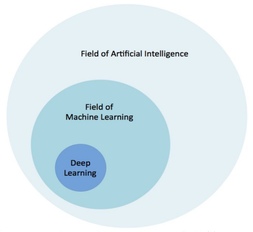

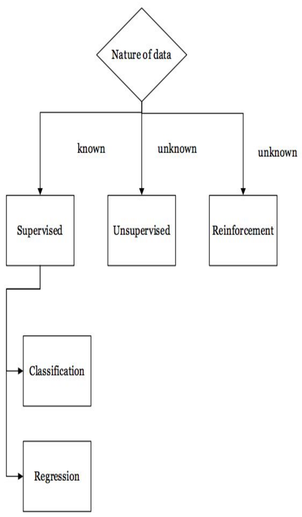

Machine Learning involves the testing of different algorithms in order to find the fastest and most accurate performing functionalities in a machine. The overarching goal is to optimize a machine's decision making skills. Machine Learning can be broken down into three categories from which further categories for examining data are derived. The three main categories are Supervised Learning, Unsupervised Learning, and Reinforcement:

Supervised: Predictions based on evidence – taking predetermined data to predict future output results of new data about to be processed. Supervised learning includes classification and regression.

Unsupervised: No previous data is present to determine future results from or the current data has not correlating conclusions to build future predictions off of. What needs to happen instead, is clustering the current data that the machine has access to in order to determine patterns within it in which conclusions can be made based off of.

Reinforcement: Learning from experience, the machine makes decisions based on previous decisions it has made. It can act based on previous states it went through. Reinforcement includes Value-based, Policy-based, and Model-based.

Overview of the algorithms in Machine Learning

Supervised:

Classification: Discrete responses, a linear function is found to divide data into two group – clusters the data into segments in order to classify future data into the appropriate segment. The data is classified based on where the data lies in comparison the linear function.

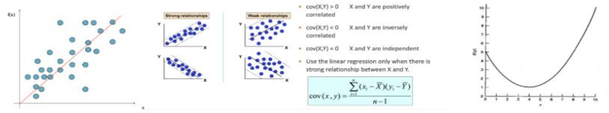

Logistic Regression (Linear)

Logistic Regression (Non-linear)

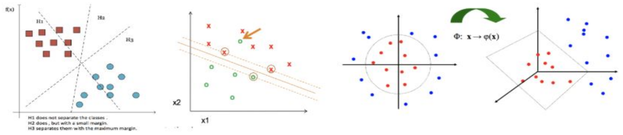

Support Vector Machine (Linear)

Support Vector Machine (Non-Linear)

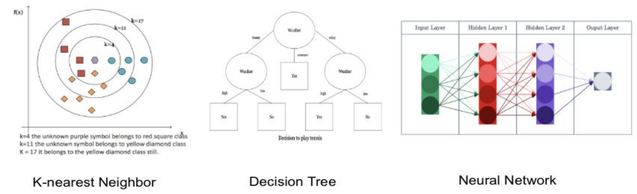

K-nearest Neighbor

Decision Tree

Neural Network

Regression: Continuous responses, in regression current data is used to predict future data, for example if you have the data of different house prices over a few years and someone asks you what the house price would be in year X then based on the regression graph you can give a fairly accurate estimate

Unsupervised:

Clustering: Collecting data together to identify patterns

- K means (choosing K is tricky, if it is too small it will be sensitive to "noise points" and if it is too large it will include unnecessary points)
- Mixture Models
- Expectation Maximization (EM)
- Belief Propagation

Reinforcement:

- Value-Based: Q-learning, real-time, dynamic programming
- Policy-based: Actor-Critic Algorithm
- Model-based: Games like Chess and GO

:

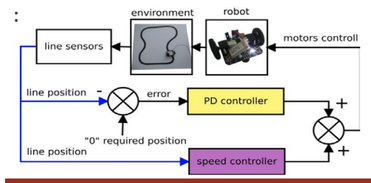

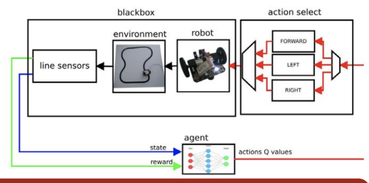

The Neuron: Core of the Neural Network

At the core of image classification is neural networks a type of supervised learning. The layers that compose a neural network rely on neurons which mimic the functionality of neurons in a human brain:

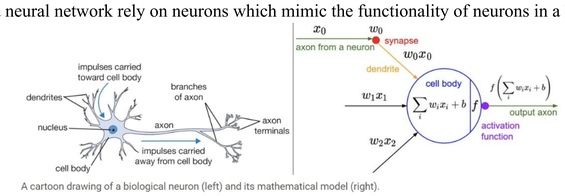

A cartoon drawing of a biological neuron (left) and its mathematical model (right).

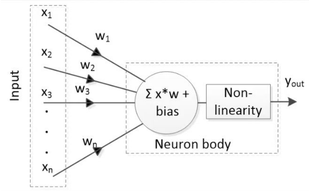

Image showing more in detail relationship between network and neuron.

AlexNet Training Results

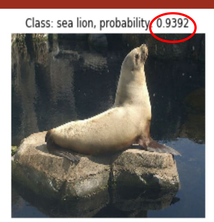


```
with tf.Session() as sess:

    # Initialize all variables
    sess.run(tf.global_variables_initializer())

    # Load the pretrained weights into the model
    model.load_initial_weights(sess)

    # Create figure handle
    fig2 = plt.figure(figsize=(15,6))

    # Loop over all images
    for i, image in enumerate(imgs):

        # Convert image to float32 and resize to (227x227)
        img = cv2.resize(image.astype(np.float32), (227,227))

        # Subtract the ImageNet mean
        img -= imagenet_mean

        # Reshape as needed to feed into model
        img = img.reshape((1,227,227,3))

        # Run the session and calculate the class probability
        probs = sess.run(softmax, feed_dict={x: img, keep_prob: 1})

        # Get the class name of the class with the highest probability
        class_name = class_names[np.argmax(probs)]

        # Plot image with class name and prob in the title
        fig2.add_subplot(1,3,i+1)
        plt.imshow(cv2.cvtColor(image, cv2.COLOR_BGR2RGB))
        plt.title("Class: " + class_name + ", probability: %.4f" %probs[0,np.argmax(probs)])
        plt.axis('off')
```

```
# Load the pretrained weights into the model
#model.load_initial_weights(sess)
```

To further help show how training based on input weights impacts AlexNet's results, the line of code that loads the weights is commented out. As you can see below, AlexNet cannot identify the images correctly anymore:

Note: This is based on a tutorial given by Kratzert. See References.

Background on ImageNet

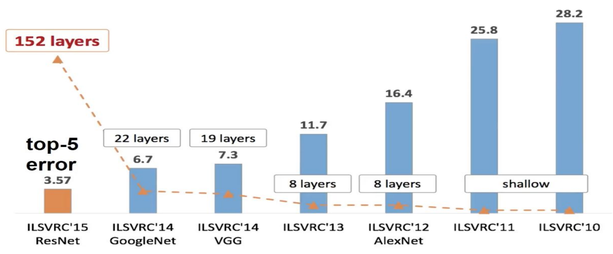

ImageNet Classification top-5 error (%)

The AlexNet Convolutional Neural Network

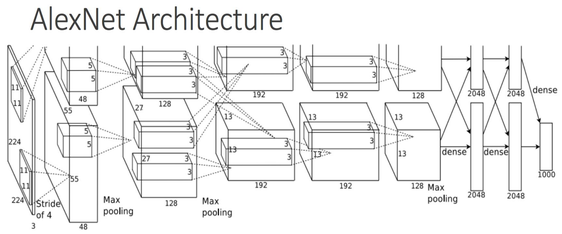

Krizhevsky, Alex, Ilya Sutskever, and Geoffrey E. Hinton. "Imagenet classification with deep convolutional neural networks." *Advances in neural information processing systems*. 2012.

Conclusion and future work

After examining all the different material, it is important to realize first and foremost the training of a neural network is necessary for a machine to be able to make decisions on its own. With a neural network like AlexNet, one can see the deeper a neural network the more accurate its results are. Considering training is a necessity for teaching a machine to identify images on its own and AlexNet is from among the best known networks, the next step comes in fine-tuning AlexNet to modify it so it can train a set of medical images. I am currently in the process of fine-tuning AlexNet to accomplish this. In doing so, I will be able to begin using what I've researched in machine learning to develop a device that can help both patients and doctors in diagnosing medical problems.

References

Kratzert, Frederik. "Finetuning AlexNet with TensorFlow." *Flair of Machine Learning - A Virtual Proof That Name Is Awesome!*, kratzert.github.io/2017/02/24/finetuning-alexnet-with-tensorflow.html.
Krizhevsky, A., Sutskever, I., Hinton, G. "*ImageNet Classification with Deep Convolutional Neural Networks", 2012.*
Gunnam, K. "Convolutional Neural Networks and Deep Machine Learning", IEEE Machine Learning Workshop (2017).
Embedded Vision Alliance. "Demystifying Deep Neural Networks," a Presentation from BDTI (w/TensorFlow Class Mention)
Wang, D., et al.: Deep learning for identifying metastatic breast cancer. arXivpreprint arXiv:1606.05718 (2016)
Liu, Y., et al. Detecting Cancer Metastases on Gigapixel Pathology Images (2017)

Process Optimization for Carbon Nanotubes-on-Graphene Fabrication

Andrew Michelmore, Julia Shaffer, Richard Senegor, Dayou Luo, and Cary Y. Yang
Center for Nanostructures, Santa Clara University

Santa Clara University
School of Engineering

Abstract

Due to superior thermal and electrical properties, carbon nanotubes (CNTs) and graphene (Gr) are promising candidates to replace copper and tungsten as interconnect materials in integrated circuits. We are exploring a three-dimensional all-carbon interconnect structure, consisting of vertically aligned CNTs grown directly on multi-layer graphene (MLG) with little or no damage to the graphene underlayer. This can serve as a building block for an on-chip interconnect network.

Background

- One major challenge in sub-20nm integrated circuit (IC) technology is the performance and reliability problem encountered in current interconnect materials, copper (Cu) and tungsten (W) [1]. Figure 1 illustrates current and projected current density requirements for Cu interconnects.
- Nanocarbons, such as CNTs and Gr, are potential replacement candidates due to their superior electrical, mechanical, and thermal properties [1,2].

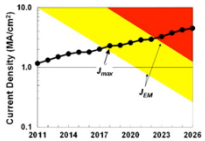

Figure 1. Projected current density requirements for Cu interconnects [1].

Objective and Methods

Figure 2 shows a schematic of a 3D CNT/Gr interconnect structure [3] which illustrates the continuous C-C bonding across the CNT-Gr interface. The objective of this project is to design a fabrication process that results in contact resistance consistent with such bonding across the interface.

Test devices fabricated in TENT Laboratory located at NASA Ames Research Center.

- Si substrate sputtered with underlayer (if needed) and catalyst film, with various sputtering times, powers, and underlayer materials (Cr and MLG).
- CNT grown on resulting sample in a plasma-enhanced chemical vapor deposition (PECVD) reactor, with various growth times and DC voltage.

Fabricated devices analyzed at Center for Nanostructures laboratory on campus.

- Imaging using scanning electron microscope (SEM) and analyses of top, tilted, and side-view images.
- Two-point electrical probing of sample using wafer probe station and parameter analyzer to obtain current-voltage (I-V) behavior and resistance, with measurement schematic shown in Figure 3.

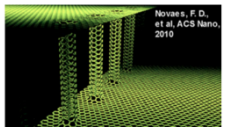

Figure 2. Computer generated schematic of CNT array connecting adjacent Gr layers [4].

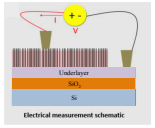

Figure 3. Electrical measurement schematic for probing CNTs [5].

Current Results

Here are four different samples that we analyzed to provide some understanding of the conduction in CNTs and MLG. The first, with CNT grown on a Cr underlayer, serves as a test of our methodology.

CNTs grown on Cr underlayer sputtered on Si substrate, using Ni catalyst and PECVD at 800 VDC

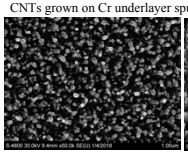

Figure 4. Top-view SEM image of PECVD grown CNT/Cr.

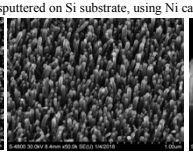

Figure 5. Tilted-view SEM image of PECVD grown CNT/Cr.

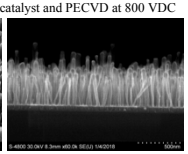

Figure 6. Cross-sectional SEM image of PECVD grown CNT/Cr.

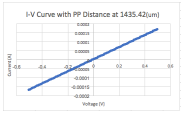

Figure 7. Typical I-V behavior for CNT/Cr sample.

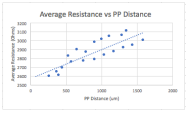

Figure 8. Average resistance vs probe-to-probe (PP) distance for CNT/Cr sample.

- CNTs grown on Cr using our standard recipe. This was done to provide a baseline growth as well as to ensure the equipment was functioning properly. The linear I-V behavior and resistance versus probe-probe distance plot show that the sample is conductive.

SEM image of bare MLG sample and electrical characteristics

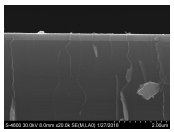

Figure 9. Cross-sectional SEM image of plain MLG.

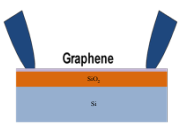

Figure 10. Probing configuration for obtaining electrical characteristics of MLG [5].

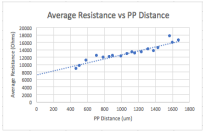

Figure 11. Average resistance vs PP distance for MLG.

- The extracted contact resistance of about 8 kΩ consists of mostly probe-MLG resistance. This result will be used for analyzing all subsequently fabricated CNT/Gr samples.

CNTs grown on MLG using Ni catalyst and PECVD at 800 VDC

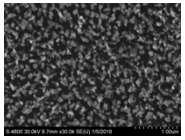

Figure 12. Top-view SEM image of 800 VDC PECVD grown CNT/MLG.

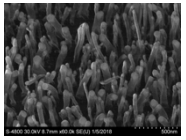

Figure 13. Tilted-view SEM image of 800 VDC PECVD grown CNT/MLG.

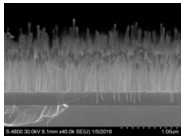

Figure 14. Cross-sectional SEM image of 800 VDC PECVD grown CNT/MLG.

- CNTs grown on MLG using the same recipe as that on Cr underlayer to verify successful CNT growth on Gr.
- The SEM images show that the CNTs are vertically aligned.
- However, the structure reveals an open circuit due to plasma damage to the graphene layer.

CNTs grown on MLG using Ni catalyst and PECVD at 500 VDC

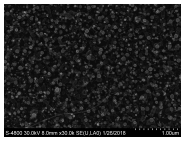

Figure 15. Top-view SEM image of 500 VDC PECVD grown CNT/MLG.

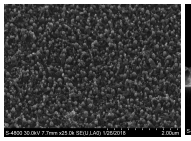

Figure 16. Tilted-view SEM image of 500 VDC PECVD grown CNT/MLG.

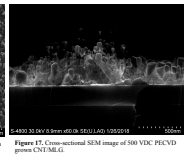

Figure 17. Cross-sectional SEM image of 500 VDC PECVD grown CNT/MLG.

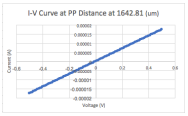

Figure 18. Typical I-V behavior for 500 VDC PECVD CNT/MLG.

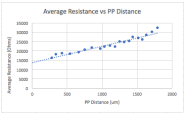

Figure 19. Average resistance vs PP distance for 500 VDC PECVD CNT/MLG sample.

- Successful growth of CNT on MLG using 500 VDC PECVD process.
- CNTs not as vertically aligned as those obtained using 800 VDC.
- The I-V and resistance results indicate that the sample is **conductive** with higher overall resistance than that of the bare MLG sample.
- This result shows that the lower DC voltage in PECVD seems to preserve the graphene underlayer.

Ongoing Experiments

There are multiple variables in the PECVD process that are being investigated, with the goal of improving the CNT alignment and reducing CNT/Gr contact resistance, while keeping the MLG intact.

- Adjust the DC voltage to improve CNT alignment.
- Use voltage pulses to generate plasma to minimize damage to MLG.
- Further analyses of electrical measurement data to extract CNT/Gr contact resistance and CNT and MLG resistivities.

Conclusion

- Our experiments confirm the results of previous work [5] from our group, which demonstrate that using PECVD at 800 VDC to grow CNTs on MLG result in vertically aligned CNTs, but the MLG underlayer is apparently damaged or destroyed resulting in an open circuit.
- Initial experiment on using 500 VDC PECVD results in a conductive CNT/Gr structure with less than optimum vertical CNT alignment.
- Our ongoing experiments are aimed at a fabrication process for a conductive CNT/Gr structure with well-aligned CNTs and no damage to the graphene underlayer. Such a structure would be consistent with continuous C-C sp^2 bonding across the CNT-Gr interface.

References

[1]International Technology Roadmap for Semiconductors, available at http://www.itrs2.net/itrs-reports.html.
[2]Balandin A 2011 Thermal properties of graphene and nanostructures carbon materials *Nature Materials* 10 569-581.
[3] Zhou C., Senegor R., Baron Z., Chen Y., Raju S., Vyas A., Chan M., Chai Y., Yang C. 2016 "Synthesis and interface characterization of CNT's on graphene" *Nanotechnology* 28 054007.
[4]Novaes F., Rurali R., Ordejon P. 2010 Electronic Transport between Graphene Layers Covalently Connected by Carbon Nanotubes *ACS Nano* 4 7596-7602.
[5]Senegor, R., Baron, Z. 2017 "Carbon Nanotubes on Graphene: Electrical and Interfacial Properties" BSEE thesis, Santa Clara University.

Bayer Feature Map Approximations through Scaling of Sensor Data

Allen Rush, Sally Wood

Determining and Predicting Convolutional Feature Map Sensitivity to Noise and Scale/Blur

Santa Clara University
School of Engineering

Objective

•Find an approximation for convolutional neural network (CNN) feature maps that use input raw Bayer pattern data directly from a sensor

Motivation

•Reduce input data to convolution neural network

•Simplify image capture process – eliminate demosaic and render pipeline

•Potential to improve accuracy- only ground truth data used (not interpolation)

Background

•In most systems images are rendered (interpolated from raw Bayer data) to form a full 3-plane RGB image. The information in the image consists of only the raw data from the sensor

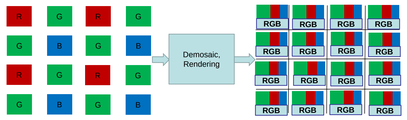

Convolutional Neural Networks

•CNNs are a class of neural networks that perform well for image classification [1]
•CNNs take images as input and output detection or classification in the form of probability vectors

•Training CNN models result in parameters that are optimized for a given training data set. Convolution layers create feature maps that are used to refine the probability of a classification of an input image

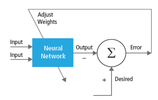

•Feature Maps are generated by convolving the input image or receptive field with a collection of convolutional kernels determine the potential fit of an image in terms of patterns, color, contrast, edge strength, and location

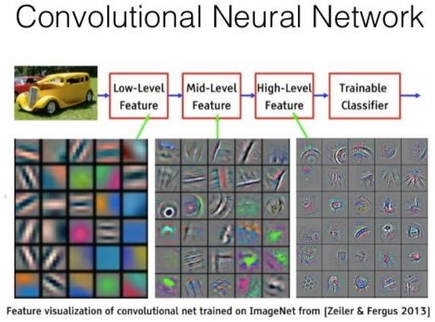

Feature Map Visualization. Simple patterns and orientation are determined in the early layers

•For deep networks, first layer feature maps are insensitive or are invariant to small changes in edge definition, shape, size, and position

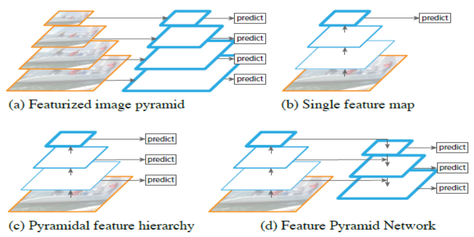

Source: Lin, Dollar, Gershick, et al [18]

Approach

We simulate the Bayer input image by applying a Gaussian blur filter to the series of test images

•In one case, we assess the detection accuracy as a function of noise.
•In the second case, we assess the detection accuracy as a function of blur

We measure the detection probability results and look for the cross-over point at which the result changes to another classification. This is the failure point after image degradation

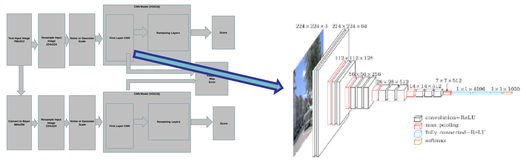

Flow to simulate raw Bayer image data as input to CNN. The output of the first layer Feature map is compared to original image feature map

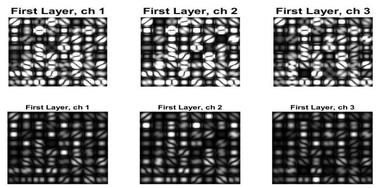

Original first layer filters and blurred version with scale =1

$$I_c(x,y) = \sum_{n=-N/2}^{N/2} \sum_{m=-M/2}^{M/2} i_{n-x,m-y} h_{n,m} \quad 1$$

$$\hat{\imath} = i * g_{Gaussian}\ (Bayer\ Estimation) \quad 2$$

$$g_{Gaussian} \propto e^{-\frac{(x+y)^2}{\sigma}} \quad 3$$

$$\hat{I_c}(x,y) \sim \sum_{n=-N/2}^{N/2} \sum_{m=-M/2}^{M/2} \hat{\imath}_{n-x,m-y} h_{n,m} \quad 4$$

$$i(x,y) = Image\ Data$$
$$h = First\ Layer\ Convolution\ Filters\ for\ each\ of\ the\ 64\ feature\ maps$$

•Convolution operations for standard image and with Bayer approximation image. MSE is given by

$$\text{MSE} = \frac{1}{XY} \sum \sum \left(I_c - \hat{I}_c \right)^2 \quad 5$$

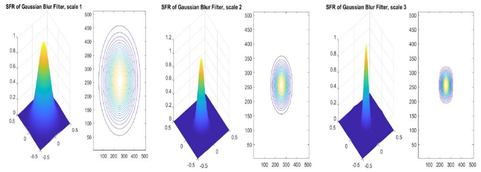

Gaussian Blur Filter used to approximate Bayer input image (scale 1,2,3)

Results

•Test Images: Kodak Test Image Set (http://r0k.us/graphics/kodak/)
•Net model: VGG16, developed by Oxford
•Only images with initial Classification Probability P(Ci)>0.5
•Noise applied to test images and cross-over detection point measured (Classification failure)
•Gaussian blur applied to test images and cross-over detection point measured (Classification failure)
•Bayer Scale with Gaussian blur applied and cross-over detection point measured (Classification failure)

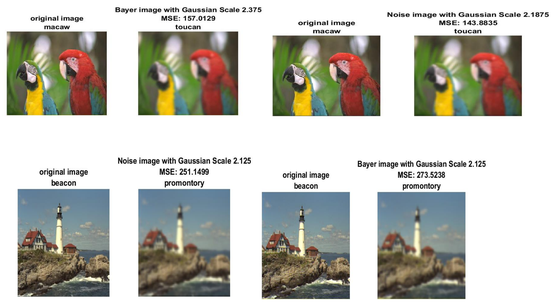

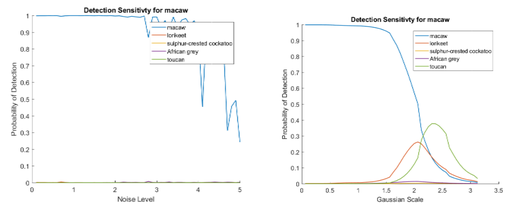

Test images with P(Ci)>.5 considered (high initial confidence). Below: example of low initial confidence (early failure, little correlation to blur)

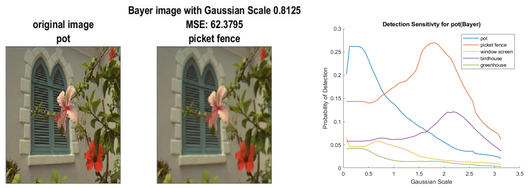

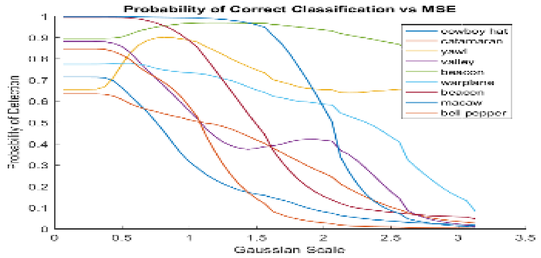

Test Image	Baseline Detection	Noise Level at Detection Change (sigma)	Gaussian Scale at Detection Change	Gaussian Scale with Bayer at Detection Change
Beacon	Beacon	2.1213	2.125	2.125
Lighthouse	Beacon	1.5811	2.0625	2.0625
Girl with hat	Cowboy Hat	1.2247	2.75	2.9375
Sailboat	Catamaran	0.54772	2.4375	2.5
Valley	Valley	1.8974	2.75	2.8125
Warplane	Warplane	1.1402	3.125	3.0625
Peppers	Peppers	0.54772	1.625	1.5625
Macaw	Macaw	*	2.1875	2.375

Conclusion

Convolutional Neural Networks that have been trained to detect objects based on a training data set can be adopted to use raw Bayer pattern sensor data as source image input. For images that exceed the mid-point classification probability (.5), the blur scale tolerance is sufficient to enable the use of raw Bayer data as the input to the first feature layer of the classification (CNN) network.

Next Steps

Derive a model for matching image capture sampling sparsity to first level feature map target response. The first level feature maps are the result of first layer convolution, and have pre-trained parameters that define the filters to apply to the input images. This represents prior information that can be used to estimate the sparse sampling or degraded image signal and still achieve the expected feature map response.

References

1. Krizhevsky, Alex, Sutskever, Ilya, and Hinton, Geoffrey E. “ImageNet classification with deep convolutional neural networks”. In NIPS, pp. 1097–1105, 2012.
2. Chen, B.,Sapiro, G., Blei, D., Dunson, D., Carin, L., “Deep Learning with Hierarchical Convolutional Factor Analysis”, IEEE Trans. on Pattern Analysis and Machine Intelligence, Vol. 35, No. 8, Aug 2013
3. Szegedy, Christian, Liu, Wei, Jia, Yangqing, Sermanet,,Pierre, Reed, Scott, Anguelov, Dragomir, Erhan, Dumitru,, Vanhoucke, Vincent, and Rabinovich, Andrew, “Going deeper with convolutions”. arXiv:1409.4842, 2014.
4. He, K., Zhang, X., Ren, S., Sun, J., “Spatial Pyramid Pooling in Deep Convolutional Networks for Visual Recognition”, IEEE Transactions on Pattern Analysis and Machine Intelligence (TPAMI) 2015.
5. Toronto, N., Morse, B., Seppi, K., Ventura, D., “Super-Resolution via Recapture and Bayesian Effect Modeling”, IEEE Conference on Computer Vision and Pattern Recognition (CVPR), 2009.
6. Li, J., Zhao, R., Wang, X., “Highly Efficient Forward and Backward Propagation of Convolutional Networks for Pixelwise Classification”, arXiv:1412.4526v2, Dec. 2014
7. Yang, B.,, Yan, J., Lei, Z., Li, A., “Convolutional Channel Features”, ICCV 2014
8. Li, J., Liang, X., Shen, S., Xu, T., Feng, J., Yan, S., “Scale-aware Fast R-CNN for Pedestrian Detection”, arXiv:1510.08160v3, June 2016
9. Kanazawa, A., Sharman, A., Jacobs, D., “Locally Scale-invariant Convolutional Neural Networks”, SICNN Workshop 2014.
10. Cai, Z., Fan, Q., Feris, R., Vasconcelos, N., “A Unified Multi-Scale Deep Convolutional Neural Network for Fast Object Detection”,
11. Yang, F., Choi, W., Lin, Y., “Exploit All the Layers: Fast and Accurate CNN Object Detector with Scale Dependent Pooling and Cascaded Rejection Classifiers”, CVPR 2016
12. Dollar, P., Appel, R., Belongie, S., Perona P., “Fast Feature Pyaramids for Object Detection”, IEEE Transactions on Pattern Analysis and Machine Intelligence, Aug. 2014
13. Nam, W., Dollar, P., Han, J., “Local Decorrelation for Improved Pedestrian Detection”, arXiv:1406.1134v2 2014
14. Lin, T., Dollar, P., Girshick, R., He, K., Hariharan, B., Belongie, S., “Feature Pyramid Networks for Object Detection”, CVPR 2016
15. Jia, Y., Huang, C., Darrell, T., “Beyond Spatial Pyramids: Receptive Field Learning for Pooled Image Features”, CVPR 2012
16. Pont-Tuset, J., Arbelaez, P., Barron, J., “Multiscale Combinatorial Grouping for Image Segmentation and Object Proposal Generation”,
17. Simonyan, K., Zisserman, A., “Very Deep Convolutional Networks for Large-Scale Image Recognition”, arXiv:1409.1556.
18. Lin,T., Dollar, P., Girshick, R., et al, “Feature Pyramid Networks for Object Detection, CVPR 2017.

DEEP LEARNING DISTANCE MEASUREMENT FOR MONOCULAR VISION

Robert H. Christiansen rhchristiansen@scu.edu
Jerry Hsu yhsu@scu.edu
Sally L. Wood swood@scu.edu

2nd Annual School of Engineering Research Showcase **February 23, 2018, Santa Clara University, Guadalupe Hall** **Santa Clara, California**

Objective

- The accurate measure of distance to objects in a road scene from a moving camera is a long-pursued goal of machine learning research.
- We have used a Deep Learning Convolution Neural Network (CNN) to detect cars in the scene using rectangular boxes described by their vertices in pixels, we assign ID's to these boxes (objects) for tracking identification , and then estimate distance from the bounding box information. Our contribution in this work is to lay a foundation of geometrical understanding for the errors (noise) inherent in the analysis of pixelated image.

Object Detection using CNN

- For object detection we choose a previously developed Convolutional Neural Network to detect, classify, and mark cars, using a bounding box described by a vector of 4 image parameters.
- The CNN detector was trained using the Nvidia Caffe deep neural networks.

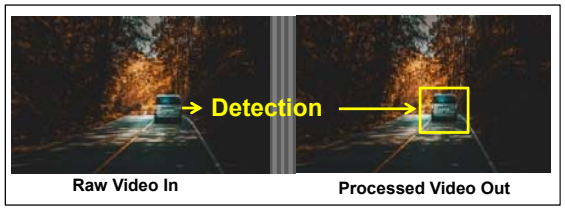

Object Detection

LIDAR Distance Ground Truth

- Much of our work requires on-road data collection.
- For this purpose, efficient design of the field test gear fulfills the resource constraints.
- For ground-truth distance required in our assessment, we use a LeddarTech optical distance sensor. In previous work this was a single-channel sensor which restricted us to a single lane, straight ahead.
- In this work we upgraded to a 16 channel ground-truth LeddarTech optical distance sensor which allowed us to expand distance measurement to adjacent lanes.

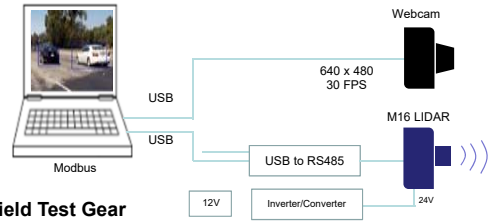

Field Test Gear

Pin-hole Camera Perspective Geometry

- The output of the detector is a bounding box superimposed on the image plane, and described by its vertices in pixels.
- Since we successfully used the bounding box information to estimate the distances to our objects, we should generalize the algebra of our estimation.
- Using pin-hole camera projective geometry analysis, and given known physical dimensions of the object, distance can be calculated analytically from the bounding box parameters.

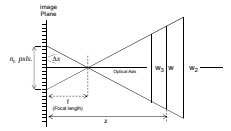

Δx : pixel width (mm)
f : focal length (mm)
W_c : car width (ft)
z : distance (ft)
OA : optical axis
x_i : car boundary(ft)

$$\frac{n_0 \Delta x}{f} = \frac{W}{z} = \frac{W_2}{z_2} = \frac{W_3}{z_3} = \cdots$$

$$z = \frac{W}{n_0 \Delta x} \cdot f = \left(\frac{1}{n_0}\right) \cdot \frac{f}{\Delta x} \cdot W$$

C

- We need to also consider the validity of the relationships when the bounding box is offset from the optical axis.

$$\frac{\frac{1}{2}W_c}{z_1} = \frac{u_2 - u_0}{f}$$

$$z_1 = \frac{W_c}{2} \frac{f}{(u_2 - u_0)}$$

$$z_1 = f \frac{(x_2 - x_0)}{(u_2 - u_0)}$$

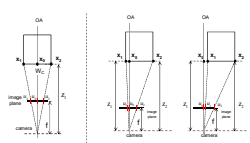

$$u_1 = \left(\frac{x_1 - x_0}{z_1}\right)\frac{f}{\Delta x} + u_0 \qquad u_2 = \left(\frac{x_2 - x_0}{z_2}\right)\frac{f}{\Delta x} + u_0$$

$$u_2 - u_1 = \left(\frac{x_2 - x_0}{z_2}\right)\frac{f}{\Delta x} + u_0 - \left(\frac{x_1 - x_0}{z_1}\right)\frac{f}{\Delta x} - u_0$$

$$= \frac{f}{\Delta x}\left[\left(\frac{x_2 - x_c}{z_2}\right) - \left(\frac{x_1 - x_c}{z_1}\right)\right] \quad \text{Assume : } z_1 = z_2 = z$$

$$u_2 - u_1 = \frac{f}{\Delta x}\left[\left(\frac{x_2 - x_c}{z}\right) - \left(\frac{x_1 - x_c}{z}\right)\right] = \frac{f}{\Delta x\, z}(x_2 - x_1)$$

Then: $z = \frac{f}{\Delta x}\frac{(x_2 - x_1)}{(u_2 - u_1)}$

From this result we can conclude the bounding box does not have to be centered on the optical axis to provide a fundamental distance estimation.

- Calibration for monocular vision is simpler than stereo vision. We only need to measure the focal length, pixel resolution and pixel size which generally can be derived from experimentation.
- The use of a checkerboard image is the best way to measure focal length.
- A simpler, albeit less accurate, measure of our webcam camera is to consider the relationship between focal length (f), the field of view (FOV), and the size of the image plane, illustrated as follows:

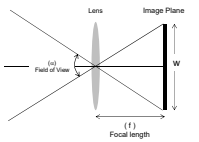

Approximate Focal Length

$$\rightarrow \tan\frac{\alpha}{2} = \frac{w}{2f} \rightarrow \cot\frac{\alpha}{2} = \frac{2f}{w}$$

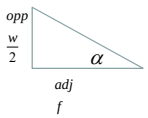

$$\frac{opp}{adj} = \tan\alpha \qquad \frac{adj}{opp} = \cot\alpha$$

Using basic trigonometry we can conclude that the field of view (a) is related to image plane dimension (w) and focal length (f) using the equation:

$$\alpha = 2\tan^{-1}\frac{w}{2f} \qquad \rightarrow \quad f = \frac{w}{2}\cot\frac{\alpha}{2}$$

Distance Estimates from the Bounding Box

- We consider errors substituent to the bounding box parameters in distance estimation

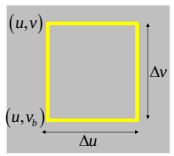

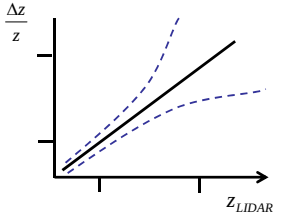

$$\hat{z}_1 = \left(\frac{f}{\Delta x}\right)\frac{W}{n} \qquad \hat{z}_2 = \left(\frac{f}{\Delta x}\right)\frac{W}{n + \Delta n} \qquad \Delta\hat{z} = \left(\hat{z}_2 - \hat{z}_1\right) \approx \frac{\Delta n}{n^2}$$

- At any given distance z, the error is normally distributed.
- Bounding Box error from different car body styles is constrained to Δu.
- Bounding Box error due to pose of the object vehicle is constrained by u,v.
- Bounding Box errors due to discrete number of pixels

– Isetta	(4.6ft)
– Coupe	(4.2ft)
– Hatchback	(5.1ft)
– Sedan	(5.3ft)
– Minivan	(5.3ft)
– Pickup	(5.7ft)
– Offroad	(4.6ft)

System Block Diagram

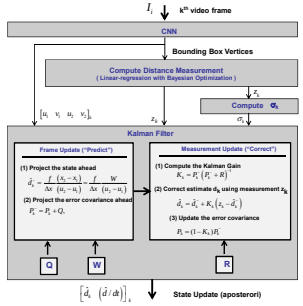

Conclusion

- A CNN is hindered by limited training data that leads to bounding box inconsistencies. This noise on the bounding box requires filtering to make distance predictions. Filtering out noise improves the utility of the neural network and extends our base of knowledge with regard to the noise sources and effective filter design.

Robust Localization of a Mars Exploration Rover Under Data Association Ambiguity in Aerial and Ground Imagery

Ph.D. Candidate: Kamak Ebadi
Thesis Advisor: Dr. Sally Wood - Co-Advisor: Dr. Curtis Padgett[1]
[1]NASA Jet Propulsion Laboratory – Maritime & Aerial Perception Systems

Jet Propulsion Laboratory
California Institute of Technology

Santa Clara University
School of Engineering

MOTIVATING APPLICATION

NASA is currently investigating the feasibility of flying a rotary-powered aircraft on the surface of Mars. A Mars Helicopter would fly ahead of a rover in order to:

- Create a high resolution map that represents the traversability of the terrain
- Identify areas of high science value to study in further detail
- Plan a route for the Mars rover to safely and efficiently navigate the terrain

PROBLEM STATEMENT

Dataset Sparsity: in remote locations on Earth or on Mars, the aerial/satellite imagery are low resolution and sparse

Perceptual Aliasing - Ambiguity in Data Association:

- Similarity between multiple scenes, each of which corresponds to a different location on the map
- Sparsity of salient features, and landmarks for detection and tracking

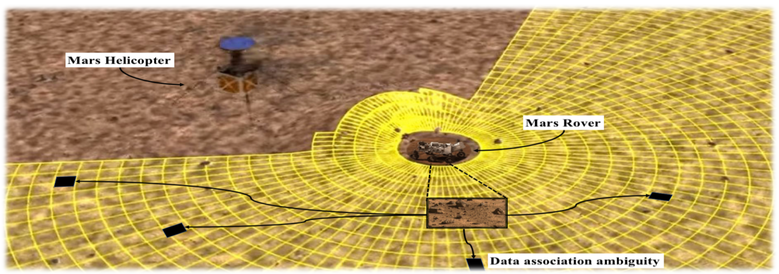

PROBLEM FORMULATION

UAV's Motion Model:

$$x_{k+1} = f(x_k, u_k, w_k) = x_k + u_k + w_k$$

Measurement/Sensing Model:

$$z_k = h(x_k, v_k)$$

$x \in \mathbb{R}^2$ → UAV's location (X-Y) on the map
$u \in \mathbb{R}^2$ → UAV's motion (odometry/command)
$w \in \mathbb{R}^2$ → Process noise
v_k → Measurement noise

PROPOSED METHOD

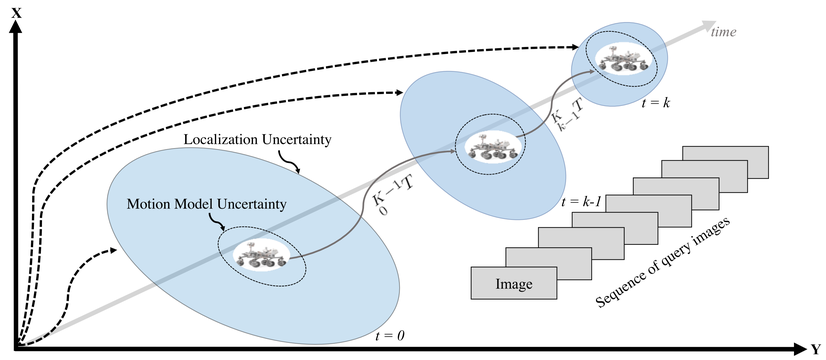

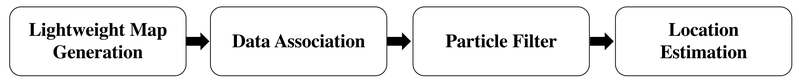

1- Lightweight Map Generation (offline):

2- Data Association (online):

3- Image Similarity Evaluation (online):

$$d_{qv} = ||Tq - v|| = \frac{1}{n}\sum_{i=1}^{n} E(q_i, v_i)$$

$$s_{qv} = \frac{\lambda}{1 + d_{qv}} \quad , \quad \lambda = \frac{n \rightarrow \text{number of inlier features in } q}{m \rightarrow \text{total \# of SURF features in the database}}$$

$$p_{qv} = \frac{sqv_i}{\sum_{i=1}^{n} sqv_i}$$

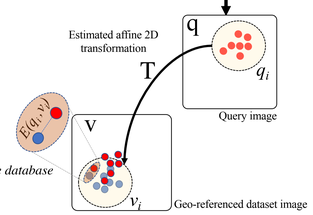

4- Particle Filter:

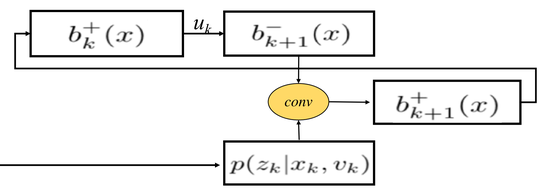

The prior belief of the copter of its location on the map:

$$b_k^-(x) = p(x|z_{0:k-1}, u_{0:k})$$

The posterior belief:

$$b_k^+(x) = p(x|z_{0:k}, u_{0:k-1})$$

Probability of z_k is evaluated at current location of every particle:

$$p(z_k|x_k, v_k), \quad v_k \sim p_v(\cdot|x_k)$$

The posterior belief at t_{K+1}

$$b_{k+1}^+(x) = b_{k+1}^-(x)p(z_{k+1}|x_{k+1}, v_{k+1})$$

REAL WORLD EXPERIMENTS

Mitrofania Island of Alaska was mapped twice in 2011 and 2016:

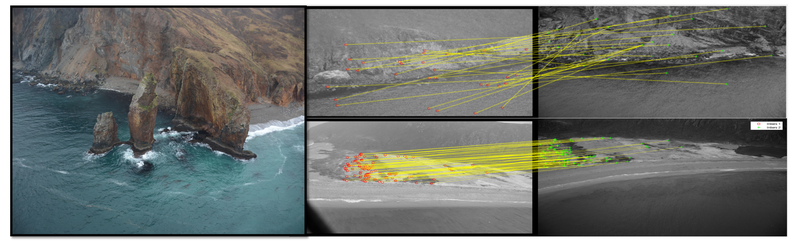

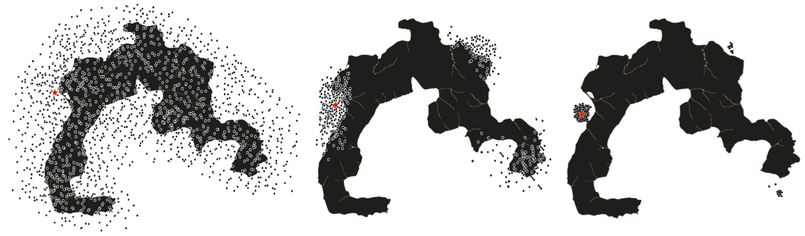

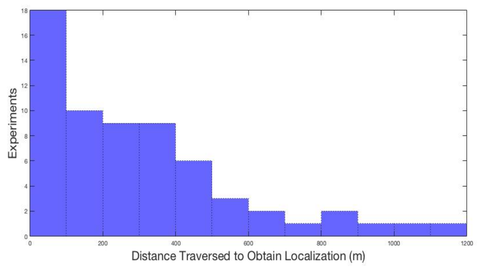

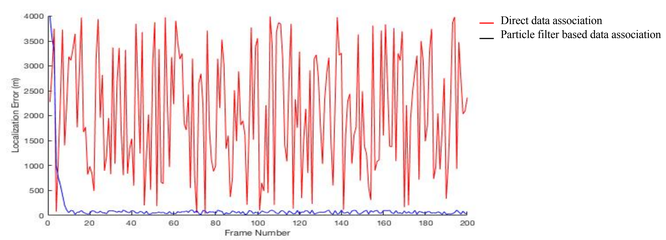

ACKNOWLEDGEMENT

This research has been conducted through a Year-Round Doctoral Research Fellowship at NASA Jet Propulsion Laboratory.
Authors would like thank NOAA for their support and providing the image dataset for Alaska ShoreZone.

Data Security using Causal Modeling

Dr. Suchitra Abel, Computer Engineering, sabel@scu.edu | Adel Abdalla, Computer Engineering, aaabdalla@scu.edu | Licheng Xiao, Computer Engineering, lxiao@scu.edu | External Collaborator: Lucy Kagiri, UC Merced | Faculty Research Adviser: Dr. Ahmed Amer, Computer Engineering, aamer@scu.edu

Santa Clara University
School of Engineering

Introduction

This poster presents the research accomplished in 2017 and January 2018, regarding data security. This shows our progress with Causal Modeling to solve important engineering and data science problems.

As “effects”, we either access continuation, or do denial of access, or thirdly, do both the denial of access to the articles and also notify the Homeland Security.

Objectives

Dataset of 20 articles and 20 users

Users : in their immediate behavior, we note 12 normal and 8 abnormal behaviors

Articles : 80% contains vital information, and 20% contains just useful information

Matrix from the original dataset

Users	Normal	Ab-s-n-v	Ab-w	Ab-s-v	Ab-w-n-v	Ab-w-v	Ab-h
1	x						
2	x						
3	x						
4	x						
5	x						
6	x						
7			x				
8			x		x		
9		x					
10			x			x	
11		x		x			
12		x		x			
13	x						
14	x						
15	x						
16			x			x	
17	x						
18	x						
19	x						
20							x

Research design / program

Abbreviations showing the abnormal behaviors of some users in the dataset, within a specified time

“Abnormal behavior – posted in social media (s), but the articles visited by this person do not have vital information (v)” --- this is abbreviated as Ab-s-n-v

“Abnormal behavior – just wavers too much (w) from article to article, which may or may not contain vital information” – this is abbreviated as Ab-w

“Abnormal behavior – wavers too much (w) – and the articles visited by this person have vital information (v)” --- this abbreviated as Ab-w-v

“Abnormal behavior – posted in social media (s), and the articles visited by this person do have vital information (v)” --- this is abbreviated as Ab-s-v

“Abnormal behavior --- wavers too much (w) from article to article, which do not contain vital information” – this is abbreviated as Ab-w-n-v

“Abnormal behavior – moved the document with vital information to a hostile nation (h)” -- this is abbreviated as Ab-h.

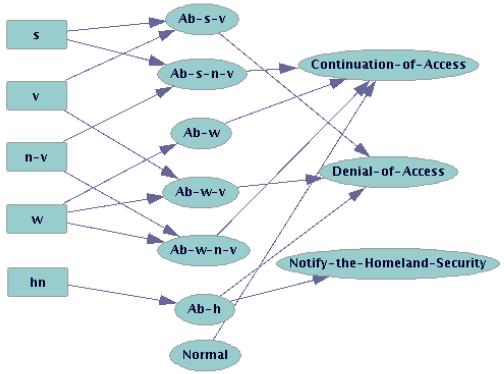

Conclusion and plans

We can conclude, based on our current research, that the equations describing the notion of causation can be formulated and utilized.

Policy $\pi(s, a)$ = highest possible probability of doing action *a* in state s

State value function: $V\pi$ (s)

= Expected return when starting in state s and following Policy π

For example, our Policy can be $\pi(s, a)$ = Policy π(Ab-s-v, deny access).

V π (s) shows the expected return of maximizing our chances of formulating the cause-effect relation properly.

We can compute the value – the reward for reaching the goal successfully; more specifically, the reward is our augmented knowledge about which subversive actions lead to which effects, in order to continue with the dataset access effectively.

Enabling Low-Power, Reliable and Timely Communication of 802.11 Devices in Cyber-Physical Systems

Jaykumar Sheth, Angelina Poole, and Behnam Dezfouli
IoT Research Lab, Department of Computer Engineering, Santa Clara University

Santa Clara University
School of Engineering

Motivation

- There will be 50 billion Internet-connected devices by 2020 [1].
- Technology has enabled the production of very a low-power WiFi stack, and the number of WiFi-based IoT devices is increasing [2].

LTE/Cellular Network	Very expensive, licensed, not energy efficient
Zigbee/Bluetooth	Low data rate, requires additional infrastructure
WiFi	Practically ubiquitous, no additional infrastructure cost, high data rate, newly manufactured 802.11 chips are low-power

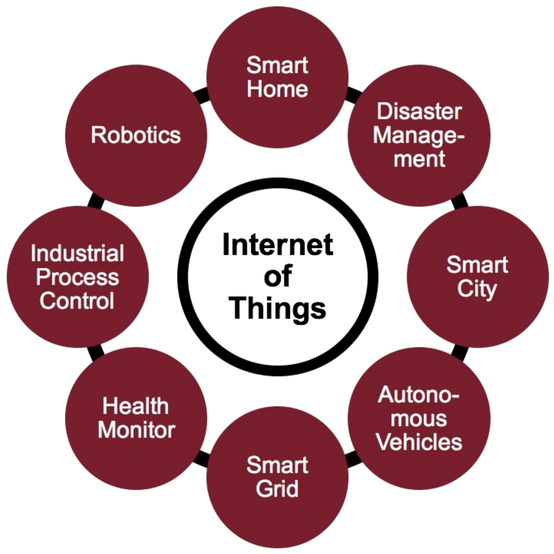

Figure 1. This Figure illustrates a few of the mission-critical IoT applications.

Problem Statement

- In this research we focus on mission-critical IoT applications, a.k.a., Cyber-Physical Systems. In particular, we are interested in using existing WiFi infrastructures for applications such as medical monitoring and industrial process control.
- The main performance metrics of the aforementioned applications are energy-efficiency, timeliness, and reliability.
- Our study shows that existing 802.11-based IoT devices suffer from high energy consumption, packet loss, and communication delay, especially in dense environments, due to interference and concurrent transmissions.
- The objective of this research is to employ scheduling and centralized network control to improve the aforementioned performance parameters.

Research Approach

Software-defined networking (SDN) as well as traffic analysis and prediction algorithms

Prediction-based sleep-awake scheduling for energy and timeliness improvement

Rate adaptation to maximize reliability

Testbed

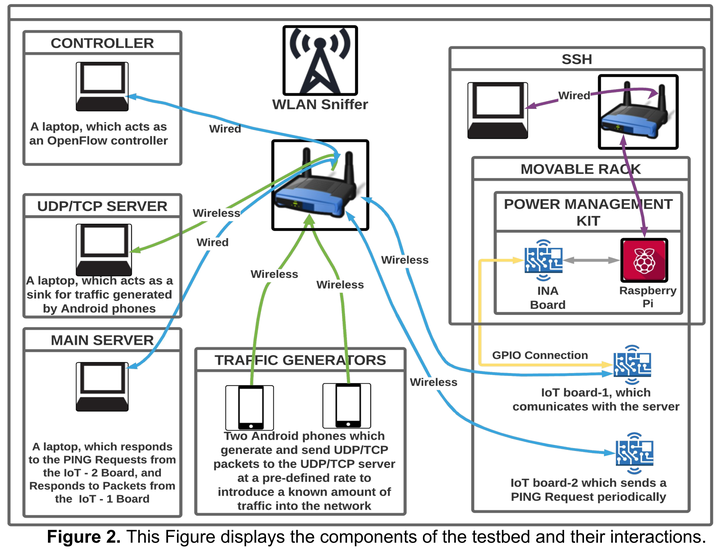

Figure 2. This Figure displays the components of the testbed and their interactions.

- A practical research platform with configurable parameters, which enables the evaluation of current technology and implementation of new ideas.
- Main components of the testbed are:
  - **A movable rack:** contains a power measurement platform and IoT boards.
  - **Android phones:** to generate actual real-life traffic
  - **Controller:** enables a centralized-global control of the network
  - **Sniffer:** to keep track of per packet activity of the entire network
- Based on a software-defined architecture:
  - The controller in the SDN has the global knowledge of variables associated with the network, such as RSSI, data rate, and traffic trends.
  - Using this knowledge, the controller and access points send hints to the stations about the probability of downlink traffic, through which the stations can decide about their sleep cycles.

Methodology

- Perform an extensive set of experiments with different variables (transmission power, distance between the IoT boards and access point, background traffic), and collect the results/statistics.
- Tools to automate the data collection and data analysis. These scripts help to examine the data and gain statistical inference from the raw data.

Results

- We have observed that there exist long gaps between packets. These are opportunities for nodes to transition into sleep mode.

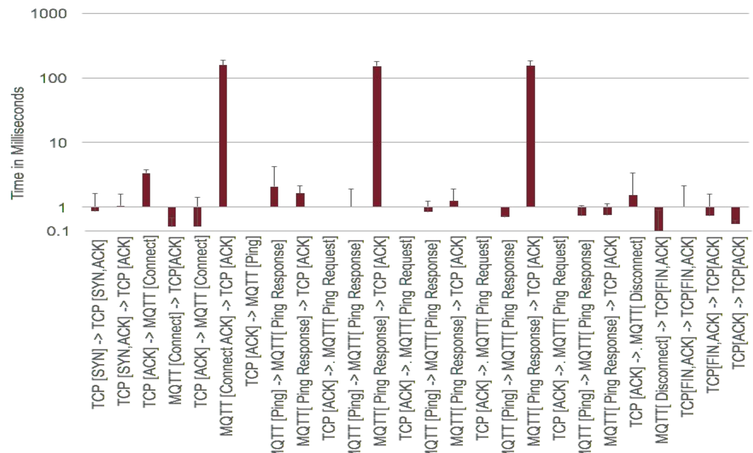

Figure 3. This Graph displays the inter-arrival times of each consecutive packet-pair exchanged during a scenario (where a station connects to the access point -> it remains idle for some time -> disconnects).

Contributions

- Software module running on the controller and access points used for traffic analysis, traffic prediction, and adjusting the operation of edge devices.
- Adjust communication parameters in order to determine an acceptable sweet spot between latency and power consumption, based on application demands.

References

[1]Evans, Dave. "The internet of things: How the next evolution of the internet is changing everything." *CISCO white paper,* 1.2011 (2011): 1-11.
[2] Tozlu, Serbulent, et al. "Wi-Fi enabled sensors for internet of things: A practical approach." *IEEE Communications Magazine* 50.6 (2012)
[3] Dezfouli, Behnam, Marjan Radi, and Octav Chipara. "REWIMO: A Real-Time and Reliable Low-Power Wireless Mobile Network." ACM Transactions on Sensor Networks (TOSN) 13.3 (2017): 17.

Santa Clara University
School of Engineering

A Remotely Programmable Software-defined Radio Platform for Low-power IoT

{ Rami Akeela and Behnam Dezfouli } Internet of Things Research Lab

Objectives

Developing an SDR platform capable of implementing various wireless communication protocols efficiently for IoT and Wireless Sensor Networks (WSNs).

1. A well-designed criteria for comparing design methodologies
2. A comprehensive survey and comparison study of SDRs and their different implementation methodologies
3. A decomposition of the protocol into a set of blocks targeting HW & SW
4. A HW/SW Co-design based SDR platform
5. Optimizations of area, timing, and power

Equipment & Tools

The following equipment was required to complete the research:

- Mathworks MATLAB & Simulink
- Avnet ZedBoard 7020 baseboard with Xilinx Zynq-7000 All Programmable SoC XC7Z020-CLG484-1
- Analog Devices AD-FMCOMMS2-EBZ
- Blade antennas
- Xilinx Vivado Design
- Xilinx SDSoC

The SDR is intended to be implemented on the Zynq SoC, which is composed of Dual-core ARM Cortex-A9 MPCore and FPGA fabric. The programmability of both enables the development of a highly programmable SDR, with hardware acceleration and power efficiency optimizations.

Introduction

Advances in wireless technologies have altered consumers' communication habits. In a technical report, the World Wireless Research Forum (WWRF) has predicted that 7 trillion wireless devices for 7 billion people will be deployed by 2020 introducing the concept of the Internet of Things (IoT). Wireless standards such as BLE, LTE, and WiFi are adapting quickly in order to accommodate different user needs and hardware specifications. This has called for a transceiver design that has the ability to handle several protocols, whether the existing ones, or the ones being developed. It needs to be flexible, re-configurable, and remotely programmable for IoT deployment.

Results 2

An All-Hardware FPGA-based proof-of-concept of PHY layer of IEEE 802.11ah WiFi protocol was demonstrated on the ZedBoard.

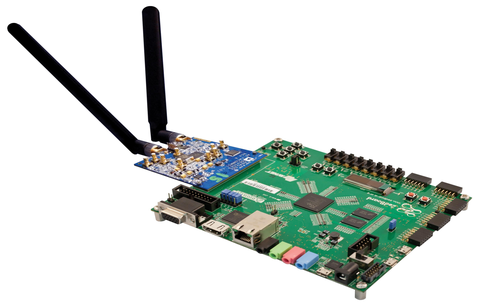

Results show timing constraints were met with a total of 18% resource utilization and 0.718 W total on-chip power. Promising results for multi-protocol, multi-band implementation.

Results 1

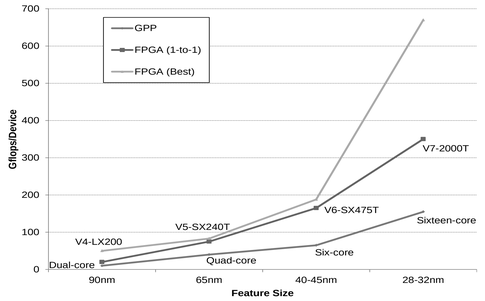

We conducted an analytical study of GPPs, GPUs, DSPs, and FPGAs and concluded through detailed comparison that FPGAs outperform the rest, and are still programmable. We also surveyed major existing SDR platforms, and deduced that co-design is the best-suited design approach for SDRs. We then surveyed development tools and determined HLS yields great results with a short turnaround time.

	Type of Hardware Platform		
	GPP	**DSP**	**FPGA**
Computation	Fixed Arithmetic Engines	Fixed Arithmetic Engines	User Configurable Logic
Execution	Sequential	Partially Parallel	Highly Parallel
Throughput	Low	Medium	High
Data Rate	Low	Medium	High
Data Width	Limited by Bus Width	Limited by Bus Width	High
Programmability	Easy	Easy	Moderate
Complex Algorithms	Easy	Easy	Moderate
I/O	Dedicated Ports	Dedicated Ports	User Configurable Ports
Cost	Low	High	Moderate
Power Efficiency	Low	Low	High
Form Factor	Large	Medium	Small
Battery Operation	No	Sometimes	Yes

Methodology & Conclusion

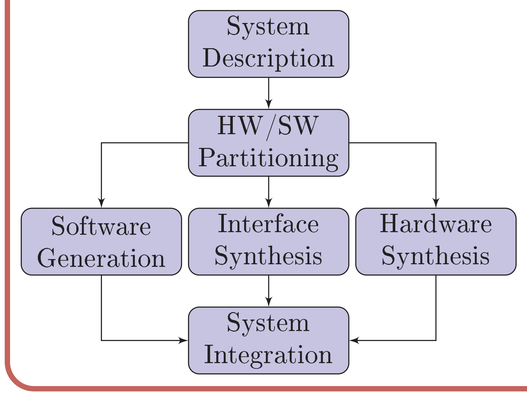

- In a 2016 report by ReportBuyer, the SDR market is projected to be more than USD 29 billion by the year 2021
- Evidenced by Ettus Research, the trend now is to develop hybrid platforms
- HW/SW Co-design approach improves design quality, design cycle time, and cost
- SoC-based SDRs have a better price to performance/Watt over GPP, GPU, and DSP-based counterparts
- SoC-based SDRs are remotely reconfigurable, which is perfect for IoT

References

[1] R. Akeela and B. Dezfouli, "Software-defined Radio: Review and Challenges," 2018.

[2] R. Akeela and Y. El Ziq, "Design and Verification of IEEE 802.11ah for IoT and M2M Applications," *2017 IEEE International Conference on Pervasive Computing and Communications Workshops (PerCom Workshops)*, pp. 491–496, Mar 2017.

Future Research

The next phase will include the development of HW/SW Co-design-based SDR for IEEE 802.11a using the partitioning methodology that will be derived. The process aims at improving the performance and energy efficiency in order to optimize battery life for IoT. This will be followed by a series of thorough field testing and optimizations. If time permits, a cross-platform comparison will be conducted to evaluate and analyze the SDR performance on multiple hardware platforms.

Contact Information

Web www.cse.scu.edu/~bdezfouli/bd-research.html

Author 1 E-mail rakeela@scu.edu

Author 2 E-mail bdezfouli@scu.edu

Neural Citation Network for Context-Aware Citation Recommendation

Travis Ebesu, Yi Fang

Department of Computer Engineering
Santa Clara University
{tebesu,yfang}@scu.edu

Santa Clara University
School of Engineering

Problem

Given a short passage of text (citation context), we recommend a list of high-quality candidate papers to cite or fill the citation placeholder. For example:

Citation Context: ...a great deal of recent research builds upon Ponte and Croft's initial proposal **[Citation Placeholder]** wherein the rank of a document d is based on the probability...

Cited Paper: Jay M. Ponte and W. Bruce Croft. 1998. A Language Modeling Approach to Information Retrieval. (SIGIR '98).

Key Contributions

- We propose a flexible encoder-decoder architecture Neural Citation Network (NCN) embodying a robust representation of the citation context with a max time delay neural network, further augmented with an attention mechanism, author networks and a gated recurrent unit decoder.
- We demonstrate the effectiveness of integrating the author networks on the large scale RefSeer dataset significantly outperforming baselines across four different metrics.

Neural Citation Network

Encoder, a Time Delay Neural Network (TDNN) $f(\cdot)$, capturing phrase level semantics over the citation context $\mathbf{X}^q$ with a sliding window of convolutions followed by max pooling

$$o_k = \text{ReLU}(\mathbf{w}^\mathsf{T}\mathbf{x}^q_{k:k+l-1} + b_k); \qquad \hat{o} = \max\{o_1, \ldots, o_{n-l+1}\}$$

Next a fully connected layer captures complex nonlinear interactions between each phrase

$$\mathbf{s}_j = \tanh(\mathbf{U}_{s_j}\hat{\mathbf{o}}_j + \mathbf{b}_{s_j})$$

Author Networks encode both the citing author(s) $\mathbf{A}^q$, and cited author(s) $\mathbf{A}^d$, with two separate TDNNs concatenated with the citation context

$$\mathbf{s}_j = [f(\mathbf{X}^q) \oplus f(\mathbf{A}^q) \oplus f(\mathbf{A}^d)]_j$$

Attention Mechanism iteratively considers the importance of the citation context, citing author(s) and cited author(s) during the decoding process

$$\mathbf{c}_i = \sum_j \alpha_{ij}\mathbf{s}_j \qquad \text{where } \alpha_{ij} = \text{softmax}(\mathbf{v}^\mathsf{T}\tanh(\mathbf{W}_a\mathbf{h}_{i-1} + \mathbf{U}_a\mathbf{s}_j))$$

Decoder leverages a Gated Recurrent Unit (GRU) to conditionally score the cited paper's title given the citation contexts and authors.

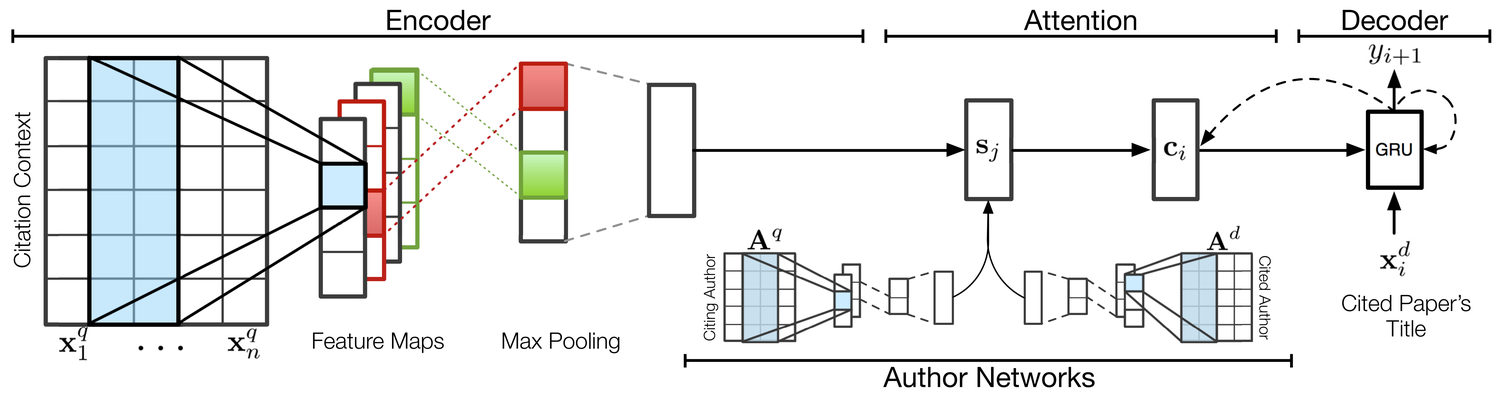

Neural Citation Network's (NCN) architecture with the attention mechanism and author networks. The dashed arrows represent recurrent dependencies.

Experiments

Results on the Refseer dataset consisting of 4,549,267 context pairs with 855,735 papers in a citation-cited relation.

	Recall	MAP	MRR	NDCG
BM-25	0.1007	0.0556	0.0606	0.0676
CTM	0.1288	0.0726	0.0777	0.0875
RNN-to-RNN	0.1590	0.0958	0.1054	0.1134
TDNN-to-RNN	0.1579	0.0935	0.1032	0.1114
Neural Citation Network	**0.2910**	**0.2418**	**0.2667**	**0.2592**

Performance comparison of the top 10 recommendations against baselines.

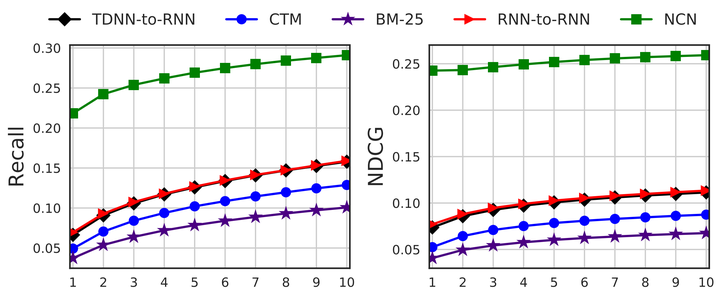

Recall and NDCG as the number of recommendations vary from 1 to 10.

Context:	"find a distribution over the latent variables that is close to the posterior of interest **[Citation Placeholder]**. Variational methods provide effective approximations in topic models and nonparametric Bayesian models"
NCN:	1. **Graphical models, exponential families, and variational inference** 2. Graphical models and variational methods 3. **An introduction to variational methods for graphical models**
CTM:	1. Indexing by latent semantic analysis 2. **An introduction to variational methods for graphical models** 3. Bayesian data analysis
RNN-to-RNN:	1. **An introduction to variational methods for graphical models** 2. The variational formulation of the Fokker–Planck equation 3. A Bayesian analysis of the multinomial probit model with fully identified parameters

Top 3 recommendations for Neural Citation Network (NCN), CTM, and RNN-to-RNN for the citation context (query), correct recommendations are in bold.

Semantic Text Hashing with Weak Supervision

Suthee Chaidaroon, Yi Fang

Department of Computer Engineering,
Santa Clara University, Santa Clara, CA 95053
{schaidaroon, yfang}@scu.edu

Santa Clara University
School of Engineering

1. Abstract

A supervised text hashing model learned from hand-labeling training data is more superior than unsupervised models in a task of similarity search. But the main bottleneck in developing and deploying the supervised hashing models is the lack of large-scale human-generated labels which is expensive and time-consuming to collect. Motivated by the success in machine learning that makes use of weak supervision, we employ low-quality but cheaply acquired supervised signals to train the semantic text hashing models. In this paper, we harness two weak signals: the sequential information extracted from text documents and the relevant documents retrieved by the BM25 retrieval model. Our proposed models utilize the weak signals and effectively learn a text hashing function that gives the competitive performance on a similar search task on four large public text corpus.

2. Semantic Hashing

SEMANTIC HASHING is an effective solution to accelerate similarity search by designing compact binary codes in a low-dimensional space so that semantically similar documents are mapped to similar codes. This approach is much more memory and computational efficient because:

- a binary code requires lesser storage space.
- computing similarity between two binary code is fast (using XOR operation).

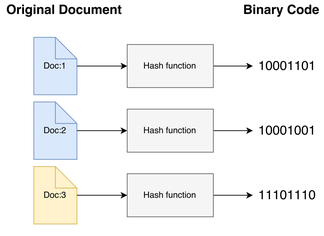

3. Objectives

We aim to learn a binary code from text data such that:

1. a binary code requires a small number of bits to encode a text document.
2. a binary code preserves the semantic of the input document.
3. a learning model does not require any hand-labeled training data such as document categories/labels.

4. Contributions

1. We propose a series of the deep generative model for text hashing. Our model architecture is applicable for pre-trained word embedding and takes word sequences as the input.
2. We propose a probabilistic model to leverage low-quality data generated by BM25 ranking model.
3. The extensive experiment on four large public text corpora demonstrates efficacy of our models over the competitive unsupervised text hashing models.

5. Generative Model

Generative models are an advancing area of research in deep learning. The main goal is to train the model to generate similar data as the training data. One such approach is to train a deep neural network to approximate the true data distribution.

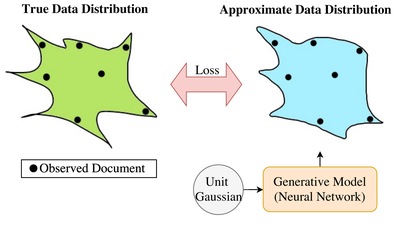

6. Convolutional Neural Networks for Text Processing

A convolutional layer is designed to detect a pattern in the sequence. In practice, a word sequence (either sentence or phrase) is represented as a matrix with V rows and L columns.

6.1 Convolutional Layer

$$C_L(\boldsymbol{X}) = \left(\sum \boldsymbol{U} \odot \boldsymbol{X}\right) + b \tag{1}$$

After applying filter C_L to all word windows, we will obtain a vector of scalars:

$$\boldsymbol{p} = [p_1, p_2, \cdots, p_{N-L+1}] = [C_L(\boldsymbol{D}_{1:L}); \cdots; C_L(\boldsymbol{D}_{N-L+1:N})]$$

6.2 Pooling Layer

We use max pooling operation to select the largest value from $\boldsymbol{p}$:

$$h = \max(\boldsymbol{p}) = \max([p_1, p_2, \cdots, p_{N-L+1}])$$

When we T filters, we will generate T feature values. Then we concatenate all scalars as a final feature vector.

$$\tilde{\boldsymbol{z}} = [h_1, h_2, \cdots, h_{\mathsf{T}}]$$

6.3 Fully-Connected Layer

The final layer is a non-linear function that transform a feature vector $\tilde{z}$ to a target vector $\boldsymbol{z}$. This layer adds flexibility to the CNN.

7. Unsupervised Model

We obtain the objective function by deriving a variational lowerbound of the log data likelihood $\log P(\boldsymbol{d})$:

$$\log P(\boldsymbol{d}) \geq \mathbb{E}_{Q(\boldsymbol{s}|\boldsymbol{d})}\left[\log P(\boldsymbol{d}|\boldsymbol{s})\right] - D_{KL}(Q(\boldsymbol{s}|\boldsymbol{d}) \parallel P(\boldsymbol{s}))$$

where $P(\boldsymbol{d}|\boldsymbol{s})$ is a product of word probability $P(w|f(\boldsymbol{s}))$:

$$P(\boldsymbol{d}|\boldsymbol{s}) = \textstyle\prod_i P(w_i|\boldsymbol{s}) \tag{2}$$

The word probability is defined as:

$$P(w_i|\boldsymbol{s}) = \frac{\exp\{\boldsymbol{s}^T \boldsymbol{A} \boldsymbol{e}_i\}}{\exp\{\sum_j \boldsymbol{s}^T \boldsymbol{A} \boldsymbol{e}_j\}} \tag{3}$$

where $\boldsymbol{e}_i$ is a onehot encoder of word i^{th}, $\boldsymbol{A}$ maps semantic vector $\boldsymbol{s}$ to a word embedding space.
we integrate CNNs a part of function f to learn function f_μ and f_σ to generate mean and standard deviation of distribution Q where $Q(\boldsymbol{s}|\boldsymbol{d};\boldsymbol{\theta}) = \mathcal{N}(\boldsymbol{s}; f(\boldsymbol{d}))$:

$$f_\mu(\boldsymbol{D}_{\text{emb}}) = \boldsymbol{W} \cdot \text{CNN}(\boldsymbol{D}_{\text{emb}}) + \boldsymbol{b} \tag{4}$$
$$f_\sigma(\boldsymbol{D}_{\text{emb}}) = \sigma\big(\boldsymbol{W} \cdot \text{CNN}(\boldsymbol{D}_{\text{emb}}) + \boldsymbol{b}\big) \tag{5}$$

A CNNs layer, CNN, calculates a feature vector $\boldsymbol{z}$ from the input document matrix $\boldsymbol{D}_{\text{emb}}$. Then, apply a transformation on $\boldsymbol{z}$ to obtain distribution parameters. Hence, we draw semantic vector $\boldsymbol{s}$ from $\mathcal{N}(\boldsymbol{s}; f_\mu(\boldsymbol{D}_{\text{emb}}), f_\sigma(\boldsymbol{D}_{\text{emb}}))$.

8. Data Augmentation with Noisy Relevant Documents

8.1 Neighborhood Construction Model

We will a set of noisy relevant document as similar documents to the input document $\boldsymbol{d}$. The objective function is:

$$\begin{aligned}\log P(\boldsymbol{d}) &= \log \int_{\boldsymbol{s}} P(\boldsymbol{d}|\boldsymbol{s}) P(\text{NN}(\boldsymbol{d})|\boldsymbol{s}) P(\boldsymbol{s}) d\boldsymbol{s} \\ &\geq \mathbb{E}_{Q(\boldsymbol{s}|\boldsymbol{d})}\left[\log P(\boldsymbol{d}|\boldsymbol{s})\right] + \mathbb{E}_{Q(\boldsymbol{s}|\boldsymbol{d})}\left[\log P(\text{NN}(\boldsymbol{d})|\boldsymbol{s})\right] \\ &\quad - D_{KL}(Q(\boldsymbol{s}|\boldsymbol{d}) \parallel P(\boldsymbol{s}))\end{aligned} \tag{6}$$

We define the neighborhood likelihood as:

$$P(\text{NN}(\boldsymbol{d})|\boldsymbol{s}) = \prod_i P_\phi(w_i|\boldsymbol{s}) \tag{7}$$

$$P_\phi(w_i|\boldsymbol{s}) = \frac{\exp\{\boldsymbol{s}^T \boldsymbol{B} \boldsymbol{e}_i\}}{\sum_j \exp\{\boldsymbol{s}^T \boldsymbol{B} \boldsymbol{e}_j\}} \tag{8}$$

8.2 Neighborhood Input Model

We define mapping function f to take noisy relevant documents as an additional input:

$$f_\mu(\boldsymbol{D}_{\text{emb}}, \text{NN}(\boldsymbol{D}_{\text{emb}})) = \boldsymbol{W_1} \cdot h_\mu + \boldsymbol{b_1} \tag{9}$$
$$h_\mu = h_\mu^{(\text{doc})} + h_\mu^{(\text{nn})} \tag{10}$$
$$h_\mu^{(\text{doc})} = \text{relu}\big(\boldsymbol{W_2} \cdot f_\mu^{(\text{doc})}(\boldsymbol{D}_{\text{emb}}) + \boldsymbol{b_2}\big) \tag{11}$$
$$h_\mu^{(\text{nn})} = \text{relu}\big(\boldsymbol{W_3} \cdot f_\mu^{(\text{nn})}(\text{NN}(\boldsymbol{D}_{\text{emb}})) + \boldsymbol{b_3}\big) \tag{12}$$

9. Results

	32 bits			
Methods	Yahoo	DBPedia	20ng	AgNews
LSH [2]	0.1465	0.5450	0.0666	0.4222
SpH [3]	0.1710	0.6068	0.2709	0.5955
STHs [4]	0.3142	0.7029	0.3860	0.6812
VDSH [1]	0.4610	0.7783	0.2678	0.7471
CNN-NN	**0.4877**	0.7932	0.4025	**0.8022**
CNN-Prior	0.4686	**0.8099**	0.3418	0.7757
CNN-Combine	0.4715	0.7933	**0.4581**	0.7982

Table 1: *Precision of the top 100 retrieved documents on four datasets with the 32-bit hash code. The bold font denotes the best result at that number of bits.*

References

[1] S. Chaidaroon and Y. Fang. Variational deep semantic hashing for text documents. In *Proceedings of the 40th International ACM SIGIR Conference on Research and Development in Information Retrieval*, SIGIR '17, pages 75–84, New York, NY, USA, 2017. ACM.

[2] M. Datar, N. Immorlica, P. Indyk, and V. S. Mirrokni. Locality-sensitive hashing scheme based on p-stable distributions. In *Proceedings of the twentieth annual symposium on Computational geometry*, pages 253–262. ACM, 2004.

[3] Y. Weiss, A. Torralba, and R. Fergus. Spectral hashing. In *Advances in neural information processing systems*, pages 1753–1760, 2009.

[4] D. Zhang, J. Wang, D. Cai, and J. Lu. Self-taught hashing for fast similarity search. In *Proceedings of the 33rd international ACM SIGIR conference on Research and development in information retrieval*, pages 18–25. ACM, 2010.

A Comparative User Study of Interactive Multilingual Search Interfaces

Chenjun Ling, Ben Steichen, Alexander Choulos, Silvia Figueira

Mobile Computing for Social Benefit Lab, Computer Science and Engineering, Department of Computer Engineering

Santa Clara University
School of Engineering

Abstract

While the number of polyglot Web users across the globe has increased dramatically, little human-centered research has been conducted to better understand and support multilingual user abilities and preferences. In particular, in the fields of cross-language and multilingual search, the majority of research has focused primarily on improving retrieval and translation accuracy, while paying comparably less attention to multilingual user interaction aspects. By contrast, this paper specifically focuses on multilingual search user interface preferences and behaviors, through a lab-based user study involving 25 participants interacting with a set of four different interactive multilingual search user interfaces. User preference results confirm that multilingual search users generally have strong preferences towards interfaces that provide clear language separation, and that the traditional approach of interleaving results, as typically used in prior research, is least preferred. In addition, an analysis of user interaction behaviors shows that multilingual users make significant use of each of their languages, and that there are several interaction behavior differences depending on interface and task type.

User Study Design

- **Multilingual Interfaces:** 4 types
  - **Interleaved**, **Universal**, **Tabbed**, **Panels**

Interleaved

Universal

Tabbed

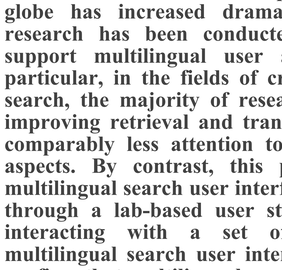

Panels

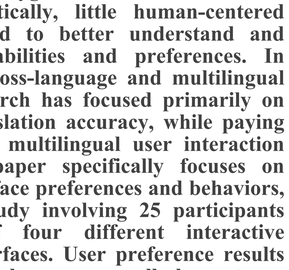

- **Task Questions and Types**
  - **3 types**: Doing, FactFinding, Learning
  - **13 task questions**: 1 practice task + 12 study tasks
- **Statistical Analysis Methods**
  - ANOVA, T-test, and Chi-squared test

Experiment

- **Procedure:** 3 steps; 90 minutes; Control order (Interface, Task)
  - **Survey**: Language proficiency, Number of languages, Language proficiency score (writing, reading, listening)
  - **Usability test:** 4 interfaces, each interface has 4 tasks (1 practice task + 3 real tasks) + 1 Questionnaire (interface)
  - **Cognitive style test**: field dependency score

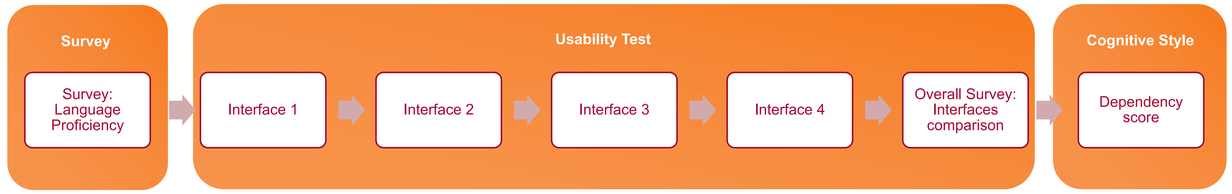

- **Participants:** 25
- **Data Source Equipment**
  - **Traditional**: Monitor, Keyboard, Mouse
  - **New (Physiological)**: Camera, Eye Tracker (Tobii)

Conclusions

Overall, it was found that clear language separation was strongly preferred, whereas an 'Interleaved' approach was least preferred. The findings from this interactive study thereby extend similar results found in studies that used static interfaces, and further present a compelling case for changing how multilingual search interfaces are built. In particular, while prior research in Multilingual Information Access has traditionally been confined to 'Interleaved' or 'Tabbed' presentation approaches, our studies have shown that these approaches are in fact often the least preferred by multilingual users. In terms of interaction behaviors, we found that users made significant use of each of their languages during search sessions. In particular, participants viewed and marked documents as relevant to a similar degree in each of their languages.

Results

- **User Preferences (RQ1)**
  - **Post and Mid Study Survey.**

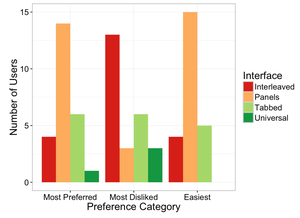

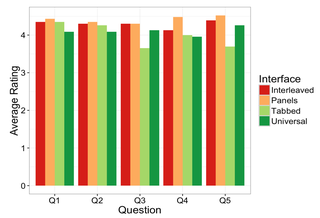

Mid-study Survey Questions
Q1: "The system provided enough information to help me solve the search tasks." (p<0.1)
Q2: "The system provided me with many different kinds of information." (p<0.4)
Q3: "The presentation of search results helped me easily combine information from multiple languages." (p<0.07)
Q4: "The presentation of search results allowed me to easily identify relevant information." (p<0.1)
Q5: "The presentation of search results helped me get an overview of the information available in multiple languages." (p<0.02)

- **General User Behavior (RQ2)**
  - **Average Query Number, Viewed Document Number, Marked relevant document number, Query language percentage.**

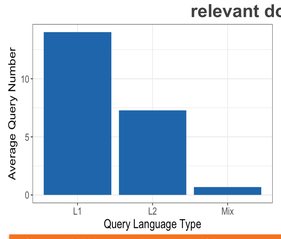

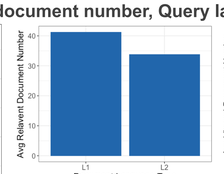

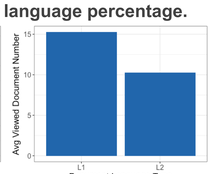

Query Pattern	Language Sequence	Percentage	Percentage
No Change	L1 only	62%	80%
	L2 only	16%	
	Mix only	2%	
Change	L1 -> L2	10.67%	20%
	L2 -> L1	3%	
	L1 -> Mix	1%	
	Mix -> L2	0.33%	
	Multiple switches	5%	

- **Influence of Interface and Task types (RQ3)**
  - **Task Time, Average query number, Query language type pattern.**

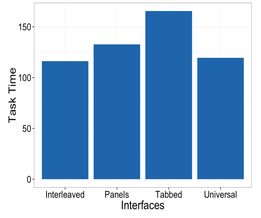

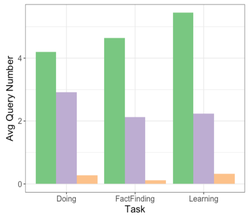

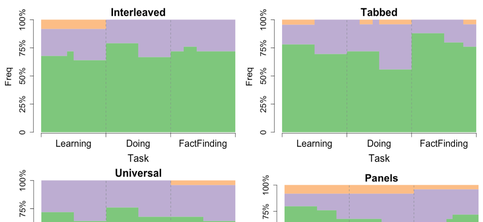

- **Eye gaze (Fixation Number, Fixation Time, Fixation Rate, Saccade length, Heatmap).**

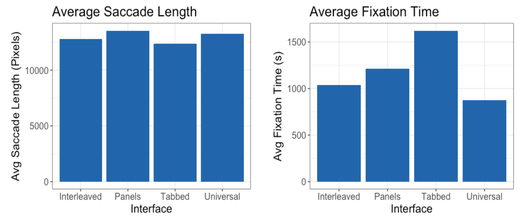

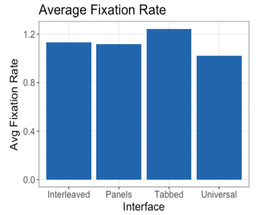

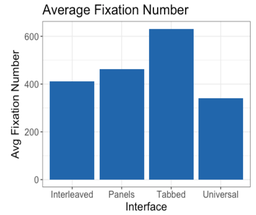

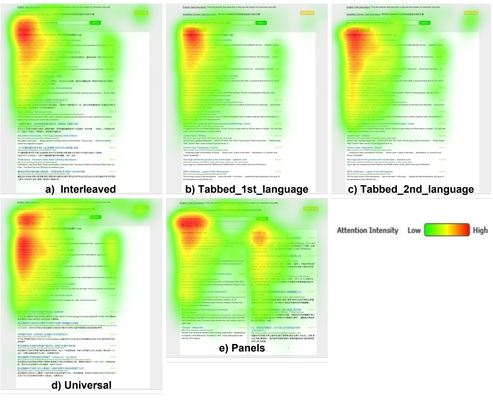

An optimized VM Allocation Strategy to Make a Secure and Energy-Efficient Cloud Against Co-residence Attack

Author: Ruiwen Li, Songjie Cai, Hanxiao He
Advisor: Yuhong Liu, Xiaojun Ruan

Santa Clara University
School of Engineering

Background

Cloud computing has become popular in both business and personal services. IaaS, or Infrastructure as a Service in cloud computing, is a service model that grants multiple users' access to a shared pool of physical resources in a dynamic way. Such dynamic resource sharing among disparate users provides the foundation of cloud computing by enabling tremendous advantages, such as the huge data storage and processing capability, scalability, and dramatic reduction in businesses costs. However, the infrastructure resource sharing among multiple tenants also raises new security challenges. Co-residence attack has been recognized as an efficient attack over the cloud infrastructure through which the attackers are able to sniff sensitive information from or negatively influence the performance of other tenants located on the same host.

Objective

We proposed a secure, workload-balanced, and energy efficient Virtual Machine (VM) allocation strategy to defend against co-residence attacks. Specifically, we modeled the VM allocation problem as an optimization problem where the goal is to minimize the security risks introduced by the co-residence of VMs from multiple users, the overall power consumption, and the unbalanced workload among different physical servers. We applied the Ant Colony Optimization (ACO) algorithm to identify the optimal allocation strategy.

Ant Colony Optimization

Ant Colony Optimization is inspired by natural ant activities. It integrates both heuristic information and randomness to find the optimized solution to a problem.

* Ants make random trails at the beginning and leave pheromone.
* More ants choose the trail with more pheromone.
* The shortest trail stands out.

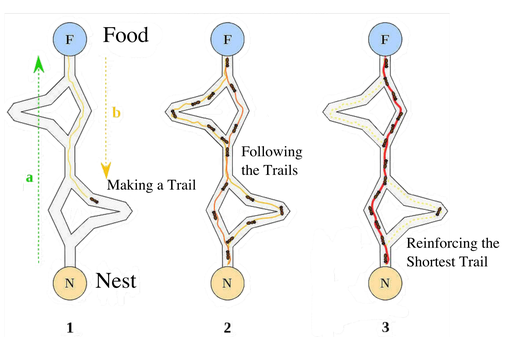

Research Design

Two connections between ACO and VM allocation:

1. The pheromone that the ants leave on the trail are the cost of an assignment of a VM to a server. The cost is calculated from an integration of its security level, power consumption, and workload balance. The pheromone is inversely proportional to the cost.

2. The paths ants take and the different assignments of VMs to servers. At first, all the assignments of a list of VMs are performed randomly. As we run the assigning process for a number of iterations, the most optimized allocation path will stand out, since at each iteration, the VMs are likely to be assigned to a server with minimum cost depending on the pheromone.

Results

We have showed that applying Ant Colony Optimization to VM allocation is effective and efficient. We explored outcomes when different parameter weights are used. If we assign a high weight of security, and low weight of workload balance and power consumption, we see the lowest cost of the VM assignment, but it requires more servers for allocation.

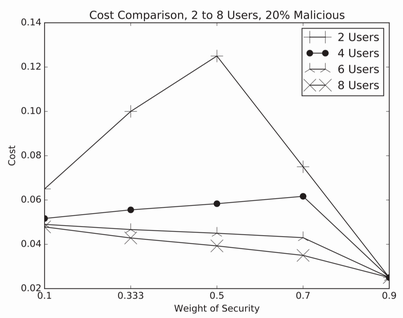

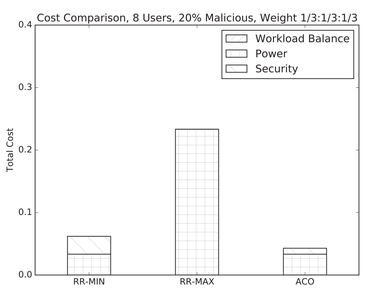

We compared our strategy with two commonly used Round-Robin VM Allocation algorithms:

RR-MIN - allocates VMs to servers in order with a minimum number of servers,

RR-MAX - sets the number of servers equal to the number of different users.

Conclusion

Co-residence attack has raised significant concerns as the increasing popularity of cloud computing. We proposed to defend against such co-residence attacks through a secure, workload-balanced, and energy-efficient VM allocation strategy, and modeled the VM allocation problem as an optimization problem. We applied the Ant Colony Optimization (ACO) algorithm, an evolutionary algorithm inspired by natural ant activities, to identify the optimal allocation strategy. Experiment results demonstrated that the proposed scheme can make the multi-tenant cloud secure and power efficient.

Future Plan

We are expanding this research for a journal paper. In future experiments, we will consider more real time factors, such as virtual machine arrival rate, the distribution of virtual machines' utilization, and integrate our program with CloudSim.

Contact Information

Advisor:
Yuhong Liu yhliu@scu.edu
Xiaojun Ruan xiaojun.ruan@gmail.com

Student:
Ruiwen Li rli@scu.edu
Songjie Cai scai@scu.edu
Hanxiao He hhe1@scu.edu